THERMODYNAMICS AND KINETICS FOR THE PEARLITE REACTION
IN
CHROMIUM STEELS

THERMODYNAMICS AND KINETICS FOR THE PEARLITE REACTION
IN
CHROMIUM STEELS

By

ROMESH CHAND SHARMA, M.Tech.

A Thesis
Submitted to the School of Graduate Studies
in Partial Fulfilment of the Requirements
for the Degree
Doctor of Philosophy

McMaster University
November 1976

DOCTOR OF PHILOSOPHY (1976)
(Metallurgy)

McMASTER UNIVERSITY
Hamilton, Ontario

TITLE: Thermodynamics and Kinetics for the Pearlite Reaction in Chromium Steels

AUTHOR: Romesh Chand Sharma, B.Tech., Indian Institute of Technology, Kanpur
M.Tech., Indian Institute of Technology, Kanpur

SUPERVISOR: Professor J.S. Kirkaldy

NUMBER OF PAGES: xii, 168

ABSTRACT

The phase equilibria in the Fe-C-Cr system, essential for the understanding of the pearlite reaction in low chromium steels, has been calculated from the thermodynamic data. The experimentally determined tie-lines are in good agreement with the calculated phase diagrams.

The pearlite growth rates and interlamellar spacings in a series of low chromium Fe-C-Cr alloys have been experimentally determined. The growth rates in these alloys are explained in terms of chromium partitioning and chromium phase boundary diffusion control at low supersaturations and in terms of the local equilibrium no-partition mechanism and carbon volume diffusion control at high supersaturations.

The relative effect of Cr, Mn and Ni on the pearlite reaction is qualitatively discussed in terms of the above mechanisms, established for the chromium steels. The results have an application to the hardenability problem in steels.

ACKNOWLEDGMENTS

The author is indebted to his supervisor, Dr. J.S. Kirkaldy, for suggesting the problems treated here and his continuous guidance throughout the course of this work. The extensive assistance offered by Dr. G.R. Purdy and the interest shown by Dr. C. Calvo, who both served on the supervisory committee, are gratefully acknowledged. The author wishes to thank the staff and graduate students of the Department of Metallurgy and Materials Science for their advice and assistance.

TABLE OF CONTENTS

LIST OF TABLES*

---

*All the tables have been placed at the end of thesis.

LIST OF FIGURES[*]

---

[*] All the figures have been placed at the end of thesis.

CHAPTER I

INTRODUCTION

A large proportion of the steels used for tools and machine parts can be classified as medium carbon, low alloy hardenability steels. The properties of these steels can be appreciably improved by quenching and tempering. A steel when cooled from the austenite (γ-face-centered cubic) phase at a sufficiently fast rate transforms to metastable martensite (a hard and brittle body-centered tetragonal) phase. On tempering martensite decomposes into ferrite (α-body-centered cubic phase) and iron carbide, so its hardness decreases and its ductility increases. Such a heat treatment produces combinations of ductility and hardness which are superior to those obtained with normalized (slow-cooled) steels.

The most significant parameter in classifying hardenability steels is the critical cooling rate. A steel must be cooled at a rate faster than the critical cooling rate to obtain 100% martensite. At slower cooling rates, austenite decomposes into stable ferrite and pearlite (or metastable bainite), pearlite being the eutectoid product of austenite decomposition.

The role of alloying elements in hardenability steels is to decrease the critical cooling rate so that thicker sections can be made responsive to quenching and tempering treatments. All the common alloying elements (with the possible exception of cobalt) decrease the critical cooling rate.(1)

The critical cooling rate for a steel is directly related to the kinetics of ferrite and pearlite reactions. The faster the kinetics of these reactions, the lower is its hardenability. Alloying elements in steels retard these reactions in varying degrees, thus increasing the hardenability.

A number of correlations,(2-5) relating hardenability to the chemical composition of steels have been developed over the years. Most of these are purely empirical, so have severe limitations with respect to accuracy and generality. Recently, Kirkaldy and co-workers have made significant progress in relating hardenability to alloy thermodynamics and to the kinetics of the pearlite reaction and other austenite decomposition products.(6) However, major gaps in our knowledge of the thermodynamics and kinetics of austenite decomposition reactions in multi-component steels remain. Hence, in the present work an intensive study of the thermodynamics and the kinetics of the pearlite reaction in the Fe-C-Cr system has been undertaken.

In the eutectoid (or pearlite) reaction the high temperature austenite phase transforms to a lamellar structure consisting of parallel lamellae of ferrite and cementite (Fe_3C-cm). It is a first order transformation and occurs by nucleation and growth.

The experimental study of nucleation is very difficult because of the very small size of the critical nucleus ($\sim$10 to 100 atoms). On the other hand, the theory of thermally activated nucleation has been fairly well established and has been recently reviewed by Russell.(7) Yet, very few attempts have been made to correlate nucleation theory with experiments in solids. Hillert(8) has suggested that pearlite develops by nucleation of ferrite. Sharma and Purdy$^{(9)}$ have recently examined the nucleation of ferrite in steels and its relationship to hardenability. The nucleation problem will not be discussed further in this thesis.

The growth of pearlite has been a subject of numerous studies, early work being carried out mainly on commercial steels. Unfortunately, the theoretical analysis of pearlite growth in these steels is complicated by the presence of a large number of elements. In the past 20 years, however, much work has been done on pearlite growth in binary Fe-C and ternary Fe-C-X (X being an alloying element) systems. An elementary theory of pearlite growth was first proposed by Zener$^{(10)}$ and this has been further developed by Hillert$^{(11)}$ and others.$^{(12-14)}$ The theory of pearlite growth in the Fe-C system is fairly well understood and has been recently reviewed by Puls and Kirkaldy.$^{(15)}$

The effect of alloying elements in reducing the pearlite growth rate is not too well understood. There is, however, some consensus that for pearlite growth in Fe-C-X systems, two regions of different retardation mechanisms exist. At low supersaturations, the alloying element must partition between the ferrite and cementite phases and the growth is controlled by the diffusion of the alloying element through the phase boundary. At high supersaturations, however, the alloying element cannot partition and the reaction is controlled through carbon diffusion and the thermodynamic effect of the alloying element. The relative importance of these mechanisms will vary with the alloying element and its concentration.

The alloying elements in steels can be divided into two groups, (i) austenite stabilizers; Mn, Ni, Cu, etc. and (ii) ferrite stabilizers; Si, Mo, V, etc. The element Cr, depending on concentration, can act as an austenite or ferrite stabilizer. This fact, among others, lead us to Fe-C-Cr as an interesting system to study.

The austenite stabilizers decrease the eutectoid temperature and thus the driving force for the pearlite reaction and their effect on decreasing the growth rate of pearlite has been satisfactorily explained purely on a thermodynamic basis by Puls and Kirkaldy.(15) Nonetheless, definite evidence for Mn partitioning during pearlite reaction at low supersaturations exists.(16,17)

The ferrite stabilizers raise the eutectoid temperature and the driving force for the pearlite reaction. Thus, their effect in retarding the pearlite growth cannot be explained solely on a thermodynamic basis. While the partitioning of Cr and Mo during pearlite growth has been experimentally established,(18,19) the theoretical basis for partitioning and the theory of pearlite growth in Fe-C-X systems has not been well established.

The present work was undertaken to obtain a greater insight into the pearlite reaction in Fe-C-X systems in general and in the Fe-C-Cr system in particular. The study has been divided into two parts. In the first part, the thermodynamics and phase diagrams of the Fe-C-Cr system are established for the low Cr (<3 weight %) range. In the second part the process for growth of pearlite in a series of Fe-C-Cr alloys is studied and related to the thermodynamic and kinetic theoretical analysis.

CHAPTER II

THERMODYNAMICS AND PHASE EQUILIBRIA IN Fe-C-Cr

II.1 INTRODUCTION

A knowledge of the phase equilibria and the thermodynamics of different phases in the system Fe-C-Cr is essential to the understanding of phase transformations in chromium steels. The general features of the phase diagram are already known. The present work is aimed at a detailed and accurate thermodynamic treatment of the ferrite, austenite and cementite phases and the equilibria between them. These are the phases involved in the pearlite reaction and the other austenite decomposition reactions in low chromium (<3% Cr) steels.

The Fe-C system has long been a subject of intensive study. The thermodynamics and phase equilibria of the Fe-C system are well established and have been recently reviewed by Harvig.(20)

A study of the thermodynamics of the Fe-Cr system was published by Müller and Kubaschewski.(21) More recently, Kirchner, Nishizawa and Uhrenius,(22) and Chipman(23) have studied the α-γ equilibrium and thermodynamics of the Fe-Cr system.

For the ternary Fe-C-Cr system, the activity of carbon in the austenite (γ) field has been studied by a number of workers. Nishizawa;(24) Bungardt, Kunze and Horn;(25) Bungardt, Preisendanz and Lehnert;(26) Jackson;(27) and Benz, Elliott and Chipman(28) have all studied the phase equilibria in Fe-C-Cr with an emphasis on high temperatures (≥850°C). The equilibrium between ferrite (α) and cementite (cm) and the stability range of cm has been discussed by Jellinghaus and Keller;(29) Kuo;(30) Bungardt et al.(25) and others.

For the study of austenite decomposition in low chromium steels, we not only need accurate equilibrium phase diagrams at temperatures below 850°C, but we also need information about the thermodynamics of the metastable phases at sub-eutectoid temperatures (<700°C).

In the present study, all the information available on the thermodynamics and phase equilibria in Fe-C, Fe-Cr and Fe-C-Cr systems has been used to establish the thermodynamics of the α, γ and cm phases and to calculate equilibria between them in the stable and metastable regions. For interpolation between various reliable data points, a quasi-regular solution model of the thermodynamics of the phases has been used. The temperature and composition range essential to the understanding of pearlite and other decomposition reactions in low chromium steels is covered. A number of critical experiments have been carried out to verify the calculations.

II.2 SOLUTION MODELS

(a) The Ferrite and Austenite Phases

For ferrite and austenite, the solutions containing substitutional as well as interstitial solutes, a simplified version of a regular solution model developed by Hillert and Staffansson(31) has been adopted. This assumes a four component solution with substitutional mixing of iron and chromium on a cubic lattice and carbon and vacancies mixing on the corresponding interstitial sub-lattice. For such a model the appropriate concentration variables are

$$Y_{Fe} = \frac{X_{Fe}}{1-X_C} \qquad (II.1)$$

$$Y_{Cr} = \frac{X_{Cr}}{1-X_C} \qquad (II.2)$$

and

$$Y_C = \frac{a}{c}\frac{X_C}{1-X_C} \qquad (II.3)$$

subject to the mass conservation conditions:

$$Y_{Fe} + Y_{Cr} = 1 \qquad (II.4)$$

and

$$X_{Fe} + X_{Cr} + X_C = 1 \qquad (II.5)$$

In equation (II.3), c/a is the number of interstitial sites per lattice site, for austenite c = a = 1 and for ferrite a = 1 and c = 3. X_{Fe}, X_{Cr} and X_C are mole fractions of iron, chromium and carbon, respectively.

The ideal entropy of mixing of one mole of solution can then be written as:

$$S^{id} = \left(\frac{1-X_C}{a}\right)\{-R[aY_{Fe}\ln Y_{Fe} + aY_{Cr}\ln Y_{Cr} + cY_C\ln Y_C + c(1-Y_C)\ln(1-Y_C)]\} \qquad (II.6)$$

and the total free energy of mixing of one mole of solution is given by:

$$G_m = X_{Fe}\,{}^{o}G_{Fe} + X_{Cr}\,{}^{o}G_{Cr} + X_C\,{}^{o}G_C - TS^{id} + {}^{E}G \qquad (II.7)$$

where ${}^{o}G_{Fe}$, ${}^{o}G_{Cr}$ and ${}^{o}G_C$ are standard free energies, T is the temperature and ${}^{E}G$ is the excess free energy of mixing. Following Hillert and Staffansson, ${}^{E}G$ can be written as:

$${}^{E}G = \left(\frac{1-X_C}{a}\right)[Y_{Fe}Y_{Cr}L_{FeCr} + Y_{Cr}Y_C L_{CCr} + Y_C(1-Y_C)L_{CV} - Y_C L_{CV}] \qquad (II.8)$$

where L_{FeCr}, L_{CrC} and L_{CV} are solution parameters which depend only on the temperature. The term $(-Y_C L_{CV})$ occurs in the expression for ${}^{E}G$ because ${}^{o}G_C$ in equation (II.7) refers to infinite dilution of C in Fe as a standard state for carbon. A higher order dependence of ${}^{E}G$ on concentrations has been suggested by Chipman and Brush(32) and by Uhrenius(33) and is included in the original solution model of Hillert and Staffansson.(31) This is equivalent to saying that the solution parameters L_{FeCr}, L_{CrC} and L_{CV} are, in general, functions of concentration. However, Chipman and Brush(32) failed to detect such higher order dependencies in Fe-C-Cr austenite, while Uhrenius(33) deduced high order parameters in Fe-C-Cr of rather high uncertainty. Our attempt to determine the concentration dependence of the solution parameters from more recently available data also did not succeed.

Consequently, the possible concentration dependencies of the solution parameters in equation (II.8) has been ignored.

The partial molar free energy, $\bar{G}_i$, of component i can be derived from G_m by the following relation:

$$\bar{G}_i = G_m + (1-X_i)\left(\frac{\partial G}{\partial X_i}\right) \tag{II.9}$$

and yields the following expressions:

$$\bar{G}_{Fe} = {}^{o}G_{Fe} + RT(\ln Y_{Fe} + \frac{c}{a}\ln(1-Y_C)) + L_{FeCr}Y_{Cr}^2 + L_{CV}Y_C^2 - L_{CCr}Y_CY_{Cr} \tag{II.10}$$

$$\bar{G}_{Cr} = {}^{o}G_{Cr} + RT(\ln Y_{Cr} + \frac{c}{a}\ln(1-Y_C)) + L_{FeCr}Y_{Fe}^2 + L_{CV}Y_C^2 + L_{CCr}Y_CY_{Cr} \tag{II.11}$$

and

$$\bar{G}_C = {}^{o}G_C + RT\ln\left[\frac{Y_C}{1-Y_C}\right] + \frac{1}{c}[-2L_{CV}Y_C + L_{CCr}Y_{Cr} \tag{II.12}$$

(b) The Carbide Phase

A number of different carbides are formed in the Fe-C-Cr system. However, here we will deal only with cementite. The general formulation can be used for other carbides. The cementite phase in Fe-C-Cr can be described as $(FeCr)C_{1/3}$. The carbon concentration and the carbon sublattice are assumed to be fixed. The ternary carbide, $(FeCr)C_{1/3}$, is formed by the substitution for Fe by Cr in the metal sublattice. Such a carbide can be considered as a solid solution of $FeC_{1/3}$ and $CrC_{1/3}$. The total free energy of mixing for this solution can be written as:(34)

$$G_m = Y_{Fe}\,{}^{o}G_{FeC_{1/3}} + Y_{Cr}\,{}^{o}G_{CrC_{1/3}} + RT[Y_{Fe}\ln Y_{Fe} + Y_{Cr}\ln Y_{Cr}] + A_{cm}Y_{Cr}Y_{Fe} \tag{II.13}$$

where ${}^{o}G_{FeC_{1/3}}$ and ${}^{o}G_{CrC_{1/3}}$ are standard free energies of formation and A_{cm} is a solution parameter.

The partial molar free energies of $FeC_{1/3}$ and $CrC_{1/3}$ will then be given by:

$$\bar{G}_{FeC_{1/3}} = {}^{o}G_{FeC_{1/3}} + RT\ln Y_{Fe} + A_{cm}Y_{Cr}^{2} \qquad (II.14)$$

and

$$\bar{G}_{CrC_{1/3}} = {}^{o}G_{CrC_{1/3}} + RT\ln Y_{Cr} + A_{cm}Y_{Fe}^{2} \qquad (II.15)$$

II.3 THE PHASE EQUILIBRIA

The phase equilibrium between austenite and ferrite is obtained by equating the partial molar free energies of each component in the two phases, i.e.,

$$\bar{G}_i^\alpha = \bar{G}_i^\gamma \qquad (i = \text{Fe, Cr, C}) \qquad \text{(II.16a,b,c)}$$

and the equilibrium between austenite (or ferrite) and cementite is given by

$$\bar{G}_M^\phi + \frac{1}{3}\bar{G}_C^\phi = \bar{G}_{MC_{1/3}} \qquad \begin{matrix}(M = \text{Fe, Cr})\\ (\phi = \gamma \text{ or } \alpha)\end{matrix} \qquad \text{(II.17a,b)}$$

To calculate the phase boundaries using equations (II.16) and (II.17), all the solution parameters defined in equations (II.8) and (II.13) for different phases and the standard free energy differences between α and γ for all three components and the free energies of formation of $FeC_{1/3}$ and $CrC_{1/3}$ are required. In the following section all these parameters are evaluated using the available thermodynamic and phase diagram data.

II.4 THE THERMODYNAMIC DATA

(a) The Fe-C System

The activity of carbon in austenite in the Fe-C system has been determined by Smith,(35) Ban-Ya, Elliott and Chipman(36,37) and others over the temperature range of stability. The most recent data of Ban-Ya et al.(37) is in good agreement with the other data reported in literature. They give the value of $\bar{G}_C^\gamma$ with standard state at infinite dilution as:

$$\bar{G}_C^\gamma = {}^oG_C^\gamma + RT\ln\left(\frac{Y_C^\gamma}{1-Y_C^\gamma}\right) + 17{,}660\,Y_C^\gamma \tag{II.18}$$

which according to equation (II.12), with $Y_{Cr} = 0$, corresponds to $L_{CV}^\gamma =$ -8830 cals/mole. This value has been adopted for our investigation, viz.,

$$L_{CV}^\gamma = -8830 \text{ cals/mole} \tag{II.19}$$

For the ferrite phase in the Fe-C system, insufficient information is available on the concentration dependence of the activity of carbon for the evaluation of L_{CV}^α. However, in the phase diagram calculations L_{CV}^α is multiplied by the terms Y_C^α and $(Y_C^\alpha)^2$ which are very small. Accordingly, without prejudice to the outcome of the calculations, L_{CV}^α has been set equal to zero.(38)

Now, the values of $({}^oG_C^\alpha - {}^oG_C^\gamma)$ and $({}^oG_{Fe}^\alpha - {}^oG_{Fe}^\gamma)$ can be obtained from the Fe-C phase diagram. For the binary Fe-C system, equation (II.16) gives

$$RT\ln\left[\frac{1-Y_C^\gamma}{(1-Y_C^\alpha)^3}\right] = ({}^oG_{Fe}^\alpha - {}^oG_{Fe}^\gamma) + L_{CV}^\alpha (Y_C^\alpha)^2 - L_{CV}^\gamma (Y_C^\gamma)^2 \tag{II.20}$$

and

$$RT\ln\left[\frac{Y_C^\gamma}{1-Y_C^\gamma}\cdot\frac{1-Y_C^\alpha}{Y_C^\alpha}\right] = ({}^0G_C^\alpha-{}^0G_C^\gamma) - 2/3L_{CV}^\alpha Y_C^\alpha + 2L_{CV}^\gamma Y_C^\gamma. \qquad (II.21)$$

By using the α-γ equilibrium concentrations from the best available phase diagram$^{(39)}$ and L_{CV}^α and L_{CV}^γ as determined above, equations (II.20) and (II.21) are solved for $({}^0G_C^\alpha-{}^0G_C^\gamma)$ and $({}^0G_{Fe}^\alpha-{}^0G_{Fe}^\gamma)$.

The $({}^0G_C^\alpha-{}^0G_C^\gamma)$ values, thus obtained, are plotted in figure (1). Within a small scatter they fall upon a straight line. The scatter is due in part to the error in picking the concentrations from the smoothed experimental phase diagram. The least squares line has been constrained so as to give the correct experimental eutectoid coordinate (.765 weight % C, 727°C).$^{(39)}$ This fit to the data gives

$$({}^0G_C^\alpha-{}^0G_C^\gamma) = 16{,}923-6{\cdot}933T(°K)\ \text{cal/mole} \qquad (II.22)$$

and this relation is used in the calculations.

The values of $({}^0G_{Fe}^\alpha-{}^0G_{Fe}^\gamma)$ calculated from equation (II.20) correspond closely to the values tabulated by Orr and Chipman$^{(40)}$ and others$^{(41-45)}$ (figure (2)). This is a good check on the overall consistancy of our data set. The tabulated values of Orr and Chipman$^{(40)}$ have been adopted for our calculations (table 1).

The γ-cm equilibrium in the Fe-C system is used to determine the free energy of formation of cementite from austenite. Equation (II.17) for the γ-cm equilibrium in the binary Fe-C gives:

$$RT\left[\ln(1-Y_C^\gamma) + \frac{1}{3}\ln\left(\frac{Y_C^\gamma}{1-Y_C^\gamma}\right)\right] = \Delta^0G^\gamma_{FeC_{1/3}} - L_{CV}^\gamma\left((Y_C^\gamma)^2 - \frac{2}{3}Y_C^\gamma\right) \qquad (II.23)$$

where

$$\Delta {}^{o}G^{\gamma}_{FeC_{1/3}} = [{}^{o}G_{FeC_{1/3}} - {}^{o}G^{\gamma}_{Fe} - \frac{1}{3}\,{}^{o}G^{\gamma}_{C}]. \qquad (II.24)$$

Since L^{γ}_{CV} is known (equation (II.19)) and since the γ-cm equilibrium in Fe-C is well-established,(27,39,46) equation (II.23) can be solved for $\Delta {}^{o}G^{\gamma}_{FeC_{1/3}}$. The values obtained as a function of temperature are fitted to an equation of the type A + BT + CTlnT as suggested by Harvig.(20) The least squares fit, subject to the condition of yielding the correct eutectoid point, gives

$$\Delta {}^{o}G^{\gamma}_{FeC_{1/3}} = -521-13.2T+1.69T\ln T \text{ cal/mole(Fe)} \qquad (II.25)$$

The data is plotted in figure (3).

The free energy of formation of cementite from ferrite, ${}^{o}G^{\alpha}_{FeC_{1/3}}$, can be written as

$$\Delta {}^{o}G^{\alpha}_{FeC_{1/3}} = [{}^{o}G_{FeC_{1/3}} - {}^{o}G^{\alpha}_{Fe} - \frac{1}{3}\,{}^{o}G^{\alpha}_{C}] \qquad (II.26)$$

and is related to $\Delta {}^{o}G^{\gamma}_{FeC_{1/3}}$ by the following relation

$$\Delta {}^{o}G^{\alpha}_{FeC_{1/3}} = \Delta {}^{o}G^{\gamma}_{FeC_{1/3}} - ({}^{o}G^{\alpha}_{Fe} - {}^{o}G^{\gamma}_{Fe}) - \frac{1}{3}({}^{o}G^{\alpha}_{C} - {}^{o}G^{\gamma}_{C}) \qquad (II.27)$$

and can be readily calculated.

(b) The Fe-Cr System

Kirchner et al.(22) have analysed the Fe-Cr system in terms of a regular solution model similar to the one used in this work. The Fe-Cr system has also been recently discussed by Chipman(23,48) and Kirchner and Uhrenius.(47) The thermodynamic parameters obtained by Kirchner et al. give the best fit to the γ-loop (figure (4)) and are consistent with the

$({}^{o}G^{\alpha}_{Cr}-{}^{o}G^{\gamma}_{Cr})$ values obtained by Kaufman.(49) Accordingly, for our calculations we have adopted the values of Kirchner et al. for the thermodynamic parameters for the Fe-Cr system. Following is a summary of these parameters.

The free energy difference between b.c.c. and hypothetical f.c.c. chromium is given by

$$({}^{o}G^{\alpha}_{Cr}-{}^{o}G^{\gamma}_{Cr}) = -2500-0.15T(°K) \text{ cal/mole} \qquad (II.28)$$

The parameter L^{α}_{FeCr}, which was obtained from the chromium activity measurements in the α phase over a range of composition and temperature and the heat of mixing data, is given by

$$L^{\alpha}_{FeCr} = 6000-2\cdot 8T \quad \text{cal/mole} \qquad (II.29)$$

The values of L^{γ}_{FeCr} were calculated to give the best fit to the experimental binary Fe-Cr phase diagram and is given by.

$$L^{\gamma}_{FeCr} = 3133-7\cdot 606T+0.6568T\ln T \quad \text{cal/mole} \qquad (II.30)$$

(c) The Fe-C-Cr System

Other parameters required for the calculation of the α-γ, γ-cm and α-cm equilibrium in the Fe-C-Cr system are L^{γ}_{CCr}, L^{α}_{CCr}, A_{cm} and the free energy of formation of $CrC_{1/3}$. These parameters are obtained from information published on the ternary Fe-Cr-C system.

(i) Ternary austenite and ferrite: The activity of carbon in Fe-Cr-C austenite has been investigated by many workers for a range of temperature and composition. This information is used to evaluate L^{γ}_{CCr}. The partial molar free energy of carbon in Fe-Cr-C austenite solutions can be written as

$$\bar{G}_C^\gamma = {}^oG_C^\gamma + RT\ln a_C^\gamma \qquad \text{(II.31)}$$

Comparing this with equation (II.12) gives:

$$RT\ln a_C^\gamma = RT\ln\left[\frac{Y_C^\gamma}{1-Y_C^\gamma}\right] + \frac{1}{c}\left[-2L_{CV}^\gamma + L_{CCr}^\gamma Y_{Cr}^\gamma\right] \qquad \text{(II.32)}$$

Since L_{CV}^γ is known (equation (II.19)) and the experimental data for a_C^γ at different temperatures and compositions of carbon and chromium is given by Nishizawa,(24) Wada et al.(50) and Greenbank,(51) we can evaluate L_{CCr}^γ from equation (II.32). No significant variation of L_{CCr}^γ with carbon and chromium content could be detected so it was assumed henceforth to be a function of temperature only. Table (2) and figure (5) summarise the experimental values of L_{CCr}^γ for each temperature. A least squares fit yields

$$L_{CCr}^\gamma = -76{,}745+40{\cdot}16T \quad \text{cal/mole} \qquad \text{(II.33)}$$

which is used in the calculations. These values of L_{CCr}^γ are in good agreement with other a_C^γ data not used in this analysis and quoted for Fe-C-Cr austenite by other workers.(26,52,53)

Values for the activity of carbon in ternary ferrite have not been experimentally determined because of the low solubility of carbon in ferrite. For this same reason the precise value of L_{CCr}^α is not critical to this calculation. It has accordingly been set equal to L_{CCr}^γ.

(ii) The ternary carbide: Since there does not exist a stable or metastable $CrC_{1/3}$ phase, the free energy of formation of this phase cannot be obtained from the Cr-C system. However, if the γ-cm equilibrium in ternary Fe-Cr-C is known with accurate tie-lines, this quantity can be deduced.

By subtracting equation (II.17b) from (II.17a) we obtain:

$$(\Delta^oG^{\gamma}_{CrC_{1/3}}-\Delta^oG^{\gamma}_{FeC_{1/3}}) + A_{cm}(1-2Y^{cm}_{Cr}) = RT\ln\left[\frac{Y^{cm}_{Fe}/Y^{cm}_{Cr}}{Y^{\gamma}_{Fe}/Y^{\gamma}_{Cr}}\right] - ({}^{E}G^{\gamma}_{Fe}-{}^{E}G^{\gamma}_{Cr}) \qquad \text{(II.33)}$$

where

$$\Delta^oG^{\gamma}_{CrC_{1/3}} = {}^oG_{CrC_{1/3}} - {}^oG^{\gamma}_{Cr} - \frac{1}{3}\,{}^oG^{\gamma}_{C}$$

$${}^{E}G^{\gamma}_{Fe} = L^{\gamma}_{FeCr}(Y^{\gamma}_{Cr})^2 + L^{\gamma}_{CV}(Y^{\gamma}_{C})^2 - L^{\gamma}_{CCr}Y^{\gamma}_{Cr}Y^{\gamma}_{C}$$

and

$${}^{E}G^{\gamma}_{Cr} = L^{\gamma}_{FeCr}(Y^{\gamma}_{Fe})^2 + L^{\gamma}_{CV}(Y^{\gamma}_{C})^2 + L^{\gamma}_{CCr}Y^{\gamma}_{Fe}Y^{\gamma}_{C}.$$

From the experimental tie-line information on the γ-cm equilibrium in ternary Fe-C-Cr tabulated by Nishizawa(24) for 1000°C, the right hand side of equation (II.33) has been calculated (table (3)) and plotted against $(1-2Y^{cm}_{Cr})$ (figure (6)). A least squares straight line is drawn through these points. From the intercept and the slope of this line the following values for $(\Delta^oG^{\gamma}_{CrC_{1/3}}-\Delta^oG^{\gamma}_{FeC_{1/3}})$ and A_{cm} are obtained:

$$(\Delta^oG^{\gamma}_{CrC_{1/3}}-\Delta^oG^{\gamma}_{FeC_{1/3}}) = -7075 \text{ cal/mole (M)} \qquad \text{(II.34)}$$

and

$$A_{cm} = 286 \text{ cal/mole (M)} \qquad \text{(II.35)}$$

Insufficient accurate data on the tie-lines in the γ+cm field in Fe-C-Cr at other temperatures are available to independently specify A_{cm} and $\Delta^oG^{\gamma}_{CrC_{1/3}}$ as functions of temperature. It is therefore assumed that A_{cm} does not vary with temperature (a true regular solution). In any case, the variation of A_{cm} with temperature is not expected to be large and A_{cm} is quite small. Accordingly, the assumptions cannot have a significant effect on the outcome of the calculations.

$\Delta^oG^\gamma_{CrC_{1/3}}$ as a function of temperature is determined using this constant A_{cm} and limited information available on the γ-cm equilibrium.(26,28,39,54) The results are summarised in table (4).

Since tie-lines in the α+cm field of Fe-C-Cr at 700°C have also been determined by Kuo,(30) Jellinghaus and Keller(29) and others, an alternative evaluation of $\Delta^oG^\gamma_{CrC_{1/3}}$ can be obtained by the following transformation:

$$(\Delta^oG^\alpha_{CrC_{1/3}}-\Delta^oG^\alpha_{FeC_{1/3}}) + A_{cm}(1-2Y^{cm}_{Cr}) = RT\ln\left[\frac{Y^{cm}_{Fe}/Y^{cm}_{Cr}}{Y^\alpha_{Fe}/Y^\alpha_{Cr}}\right] - ({}^EG^\alpha_{Fe}-{}^EG^\alpha_{Cr}) \qquad \text{(II.36)}$$

and

$$(\Delta^oG^\gamma_{CrC_{1/3}}-\Delta^oG^\gamma_{FeC_{1/3}}) = (\Delta^oG^\alpha_{CrC_{1/3}}-\Delta^oG^\alpha_{FeC_{1/3}}) - ({}^oG^\gamma_{Cr}-{}^oG^\alpha_{Cr}) + ({}^oG^\gamma_{Fe}-{}^oG^\alpha_{Fe}) \qquad \text{(II.37)}$$

The results of this calculation are summarised in table (5) and should be compared with the corresponding results in table (4).

The values of $(\Delta^oG^\gamma_{CrC_{1/3}}-\Delta^oG^\gamma_{FeC_{1/3}})$ calculated from the two data bases are in reasonable agreement. Unfortunately, the scatter in both sets is sufficient to conceal a possible temperature dependence. The averages obtained from table (4), (-6734) and from table (5), (-6575), are within 5% and 7%, respectively, of -7075, obtained from the comprehensive data set of Nishizawa(24) at 1000°C (equation II.34). Hence, we have adopted the temperature independent value of $(\Delta^{o}G^{\gamma}_{CrC_{1/3}} - \Delta^{o}G^{\gamma}_{FeC_{1/3}})$ = -7075 cal/mole (M) evaluated from what we believe is the best data set. This gives

$$\Delta^{o}G^{\gamma}_{CrC_{1/3}} = -7596-13.2T+1.69T\ln T \quad \text{cal/mole (Cr)} \tag{II.38}$$

and $\Delta^{o}G^{\alpha}_{CrC_{1/3}}$ can be obtained from the following relation

$$\Delta^{o}G^{\alpha}_{CrC_{1/3}} = \Delta^{o}G^{\gamma}_{CrC_{1/3}} - ({}^{o}G^{\alpha}_{Cr} - {}^{o}G^{\gamma}_{Cr}) - \frac{1}{3}({}^{o}G^{\alpha}_{C} - {}^{o}G^{\gamma}_{C}) \tag{II.39}$$

II.5 CALCULATION OF THE PHASE EQUILIBRIA

All the thermodynamic data required to calculate the phase equilibria according to the equations (II.16) and (II.17) are now known. These data are summarised in table (6).

(a) The α-γ Equilibrium

The α-γ equilibrium is given by equations (II.16a,b,c). Substituting equations (II.10), (II.11) and (II.12) into equation (II.16) we obtain:

$$\frac{Y^{\gamma}_{Fe}}{Y^{\alpha}_{Fe}}\frac{(1-Y^{\gamma}_{C})}{(1-Y^{\alpha}_{C})^3} = \exp[\frac{1}{RT}({}^{0}G^{\alpha}_{Fe}-{}^{0}G^{\gamma}_{Fe}) + \frac{1}{RT}(-L_{CrC}(Y^{\alpha}_{Cr}Y^{\alpha}_{C}-Y^{\gamma}_{Cr}Y^{\gamma}_{C})$$

$$+ L^{\alpha}_{FeCr}(Y^{\alpha}_{Cr})^2 - L^{\gamma}_{FeCr}(Y^{\gamma}_{Cr})^2 - L^{\gamma}_{CV}(Y^{\gamma}_{C})^2)] \qquad \text{(II.40a)}$$

$$\frac{Y^{\gamma}_{Cr}}{Y^{\alpha}_{Cr}}\frac{(1-Y^{\gamma}_{C})}{(1-Y^{\alpha}_{C})^3} = \exp[\frac{1}{RT}({}^{0}G^{\alpha}_{Cr}-{}^{0}G^{\gamma}_{Cr}) + \frac{1}{RT}(L_{CrC}(Y^{\alpha}_{Fe}Y^{\alpha}_{C}-Y^{\gamma}_{Fe}Y^{\gamma}_{C})$$

$$+ L^{\alpha}_{FeCr}(Y^{\alpha}_{Fe})^2 - L^{\gamma}_{FeCr}(Y^{\gamma}_{Fe})^2 - L^{\gamma}_{CV}(Y^{\gamma}_{C})^2)] \qquad \text{(II.40b)}$$

and

$$\frac{Y^{\gamma}_{C}}{Y^{\alpha}_{C}}\frac{(1-Y^{\alpha}_{C})}{(1-Y^{\gamma}_{C})} = \exp[\frac{1}{RT}({}^{0}G^{\alpha}_{C}-{}^{0}G^{\gamma}_{C}) + \frac{1}{RT}(L_{CrC}(\frac{1}{3}Y^{\alpha}_{Cr}-Y^{\gamma}_{Cr}) + 2L^{\gamma}_{CV}Y^{\gamma}_{C})] \qquad \text{(II.40c)}$$

These are three equations involving four independent concentration terms. By fixing the temperature and the value of one concentration term, equations (II.40) can be solved for the other three concentrations, thus defining a single tie-line in the $\alpha+\gamma$ field. In our case, the equations were solved for a set of given values of Y_{Cr}^{α} by computer iteration, thus defining the stable (or metastable) $\alpha+\gamma$ phase field in the Fe-C-Cr system for the low chromium range. The predictions (lines) are shown in figures (7), (8) and (9). Figures (7) and (8) show the stable $\alpha+\gamma$ region at 770°C and 750°C, respectively, while figure (9) shows the predicted metastable $\alpha+\gamma$ field at 700°C.

(b) The γ(or α)-cm Equilibrium

The γ(or α)-cm equilibrium is given by equations (II.17a,b). Substituting the appropriate equations from equations (II.10), (II.11), (II.12), (II.14) and (II.15) into the equations (II.17a,b) and rearranging we get the following for the γ-cm equilibrium

$$\frac{(Y_{Cr}^{cm}/Y_{Fe}^{cm})}{(Y_{Cr}^{\gamma}/Y_{Fe}^{\gamma})} = \exp[\frac{1}{RT}(\Delta^{o}G_{FeC_{1/3}}^{\gamma}-\Delta^{o}G_{CrC_{1/3}}^{\gamma}) + \frac{1}{RT}(L_{CrC}Y_{C}^{\gamma}$$

$$+ L_{FeCr}^{\gamma}(1-2Y_{Cr}^{\gamma}) - A_{cm}(1-2Y_{Cr}^{cm}))] \qquad \text{(II.41a)}$$

and

$$\frac{Y_{Fe}^{\gamma}}{Y_{Fe}^{cm}}(Y_{C}^{\gamma})^{1/3}(1-Y_{C}^{\gamma})^{2/3} = \exp[\frac{1}{RT}(\Delta^{o}G_{FeC_{1/3}}^{\gamma}) + \frac{1}{RT}(A_{cm}(Y_{Cr}^{cm})^{2}$$

$$+ L_{CV}^{\gamma}(2/3-Y_{C}^{\gamma})Y_{C}^{\gamma} - L_{CrC}^{\gamma}Y_{Cr}^{\gamma}(1/3-Y_{C}^{\gamma})$$

$$- L_{FeCr}^{\gamma}(Y_{Cr}^{\gamma})^{2})] \qquad \text{(II.41b)}$$

and for the α-cm equilibrium:

$$\frac{(Y^{cm}_{Cr}/Y^{cm}_{Fe})}{(Y^{\alpha}_{Cr}/Y^{\alpha}_{Fe})} = \exp\Big[\frac{1}{RT}(\Delta{}^{o}G^{\alpha}_{FeC_{1/3}} - \Delta{}^{o}G^{\alpha}_{CrC_{1/3}}) + \frac{1}{RT}(L_{CrC}Y^{\alpha}_{C}$$

$$+ L^{\alpha}_{FeCr}(1-2Y^{\alpha}_{Cr}) - A_{cm}(1-2Y^{cm}_{Cr}))\Big] \qquad \text{(II.42a)}$$

and

$$\frac{Y^{\alpha}_{Fe}}{Y^{cm}_{Fe}}\,(Y^{\alpha}_{C})^{1/3}(1-Y^{\alpha}_{C})^{8/3} = \exp\Big[\frac{1}{RT}(\Delta{}^{o}G^{\alpha}_{FeC_{1/3}}) + \frac{1}{RT}(A_{cm}(Y^{cm}_{Cr})^{2}$$

$$- L_{CrC}Y^{\alpha}_{Cr}(1 - Y^{\alpha}_{C}) - L^{\alpha}_{FeCr}(Y^{\alpha}_{Cr})^{2})\Big] \qquad \text{(II.42b)}$$

In the case of the γ(or α)-cm equilibrium, there are only two equations involving three independent concentrations; two for the γ(or α) phase and only one for the cementite since the carbon concentration in cementite is fixed. The equations are solved for the γ(or α)-cm equilibrium by fixing Y^{γ}_{Cr} (or Y^{α}_{Cr}) and solving for the other two concentrations by computer iteration, giving the stable (or metastable) two phase fields. The results of the calculations for γ-cm equilibrium are also shown in figures (7), (8) and (9) and for the α-cm equilibrium in figures (8) and (10).

(c) The Eutectoid Point and the Three Phase Equilibrium

The intersection of the (α+γ)/γ and the γ/(γ+cm) phase boundaries defines the eutectoid point as indicated in figure (8). Figure (11) shows the predicted variation of the eutectoid temperature and the eutectoid carbon composition as a function of the chromium concentration.

The equilibrium three phase field, (α+γ+cm), is defined by the three phase triangle as shown in figure (8). The intersection of the α/(α+γ) and α/(α+cm) phase boundaries defines the point of the three phase triangle at the α-phase end and the eutectoid point at the γ-phase end. The point at the cementite line is defined by the α-cm tie-line from the α-phase end and the γ-cm tie-line from the γ-phase end. The fact that the γ-cm and α-cm tie-lines which form the boundaries of the three phase field intersect at exactly 25 atomic % carbon ($(\mathrm{(FeCr)C}_{1/3})$), demonstrates the internal consistency of the calculations relating different phase fields.

II.6 EXPERIMENTAL DETERMINATION OF THE TIE-LINES

The calculated phase diagrams (figures (7) through (11)) are in general accord with the very limited ternary measurements available. (24,26,28-30,39,54) To further verify the calculated phase diagrams, we carried out a few critical experiments at lower temperatures. In particular, tie-lines in stable ($\alpha+\gamma$) and (γ+cm) regions were determined at 770°C and 750°C and (α+cm) tie-lines were determined at 700°C. One experiment was carried out in the three phase region at 750°C.

(a) Preparation of the Material

The Fe-Cr binary alloys were prepared from electrolytic iron and high purity chromium stock and melted in a non-consumable tungsten electrode arc furnace under an argon atmosphere. The alloy buttons (around 100 gms each) were turned and melted at least four times to attain a uniform solution of iron and chromium. The buttons thus obtained were cold rolled to about 1/2 cm thickness and homogenized at 1050°C for about 10 days and then further cold rolled to a final thickness of $\sim$0.5 mm. The samples of about 1 cm x 2 cm were cut from these sheets and carburized in a flowing $CO-CO_2$ gas mixture at 1000°C to the required carbon content. The times (t) for which the samples were carburized were sufficient to ensure a homogeneous carbon content ($\frac{D_C t}{\ell^2} > 5$, where D_C is the carbon diffusion coefficient and ℓ is the half thickness of the sample). The samples, after the carburizing treatment, were directly quenched in water.

The samples were then analysed for chromium and carbon using standard procedures. The compositions of the alloys used for the tie-line experiments are given in tables (7) through (10) under the columns for 'alloy composition'.

(b) Tie-Line Experiments in the $(\alpha+\gamma)$ Region

The experimental determination of the tie-lines in the Fe-C-Cr system at low temperatures is difficult because of the slow diffusion of Cr, particularly in the austenite phase. The times required to obtain thermodynamic equilibrium are generally impractically large. The tie-lines could in principle be determined from diffusion couple experiments. However, this method proved impractical because the error involved in extrapolating the steep concentration gradients to the interface is large and the Cameca microprobe at McMaster could not analyse accurately enough for the low carbon contents.

Some time ago, Gilmour(54) and Gilmour et al.(55) developed a technique to overcome the difficulty of slow diffusion and we have proceeded along the same lines. Kurdjumov(56) had shown that the diffusion of the substitutional elements in up-quenched ternary austenites is greatly enhanced because of the presence of an extensive defect structure. Furthermore, the diffusion of Cr in ferrite is known to be approximately two orders of magnitude higher than in austenite.(57) To take advantage of these increased mobilities in equilibrating the alloys at low temperatures, our alloys were quenched from the high temperature (1000°C) austenite region to produce martensite, encapsulated in quartz tubes with an argon atmosphere and inserted into a preheated Kanthal furnace at the equilibration temperature to produce an austenite dispersion in a ferrite matrix.

After about a week the capsules were removed from the furnace and dropped into water without breaking the capsule. The microstructure indicated that this rate of cooling was sufficient to produce all martensite in former austenite regions. The samples were then reduced in thickness by 5 to 10% by hammering to produce more dislocations and thus enhance the diffusion of chromium in both the α and the γ phases. The samples were then re-encapsulated and inserted in the furnace. This procedure was repeated three times. After the final heat treatment, samples were quenched in water by breaking the capsules under water. The total time for the isothermal treatment was 5.5×10^6 secs at 770°C and 1.05×10^7 secs at 750°C. The temperature was controlled to ±2°C and periodically checked during the heat treatment.

The samples were analysed for chromium distribution between α and γ using the Cameca microprobe, detecting chromium K_α radiation. A typical microstructure and a preliminary scan is shown in figure (12). Careful point counts accross the sample did not indicate any chromium gradients within a phase. This is good assurance that the phases are in thermodynamic equilibrium.

Both phases, the ferrite and the martensite (formerly austenite), were quantitatively analysed for chromium using an accelerating voltage of 20 kV and a beam current of 120 nano-amps. The background radiation was measured on pure electrolytic iron and the original untreated martensitic alloy was used as a standard for chromium, assuming background subtracted counts as proportional to the weight percent of chromium. This linearity was verified by analysing three alloys of different chromium contents mounted together and analysed under similar conditions. Figure (13) shows a typical calibration curve, which is a straight line within the experimental error. This justified the procedure adopted in calculating the chromium content of the different phases from the microprobe data. The samples were lightly etched with 2% nital but this has been shown to have no effect on the microprobe analysis.(5[illegible])

The volume fraction of the two phases (α and martensite) was determined using an automatic image analyser at the Steel Company of Canada Research Laboratories. Knowing the bulk carbon content and the volume fractions of the phases (a correction of 4% was made to allow for the volume expansion of the austenite in the martensitic transformation(59)) the carbon content of the austenite could be calculated from the carbon mass balance. The carbon content of the ferrite was assumed to be the same as in the calculated phase diagram. This, along with the chromium analysis by microprobe, resulted in a complete determination of the tie-lines in the α+γ region.

(c) The Tie-line Experiments in the (γ+cm) and the (α+cm) Regions

The alloys of appropriate compositions were prepared as described previously. The samples of the alloys in martensitic form were encapsulated in quartz tubes in argon atmosphere and heat treated at the equilibration temperatures for times ranging from 15 days for the α+cm equilibrium at 700°C to over a month ~~for the~~ γ+cm equilibrium at 750°C and 770°C. The carbides precipitated as a fine dispersion at these temperatures. An estimate of the chromium diffusion distance indicates that the above times were more than sufficient to obtain thermodynamic equilibrium. Figures (14) and (15) show typical micrographs of the samples equilibrated in the γ+cm and the α+cm regions, respectively.

(i) Carbide analysis: The cementite particles in these alloys were too small for analysis by the electron microprobe. Furthermore, extraction and chemical analysis is not [illegible]ble for martensite (formerly austenite) - carbide samples. Hence analy[illegible]s achieved by preparing carbide extraction replicas for the Phili[illegible] electron microscope fitted with the EDAX energy dispersion sili[illegible] detector system. The technique is described below.

In a 'thin' specimen the primary X-rays produced by the incident electron beam have a very low probability of either being absorbed or exciting fluorescent radiation in the sample. In such a case one can write:(60-62)

$$\frac{I_1}{I_2} = k \frac{C_1}{C_2} \tag{II.43}$$

where I_1 and I_2 are measured characteristic X-ray intensities and C_1 and C_2 are the weight fractions of any pair of elements (e.g., Fe and Cr in our case). The factor k depends only on the relative efficiency of X-ray production for these two elements and the detector (Si[Li]) efficiency. For a given instrument and operating voltage, k is a constant for a given pair of elements. Note that the ratio (I_1/I_2) depends only on the weight fractions of the two elements in question and not on the weight fractions of other elements present as well, as is the case in bulk sample microprobe analysis. The constant k can be experimentally determined for a given instrument operating under specific conditions once and for all.

Provided the specimen is thin enough to satisfy the above conditions, equation (II.43) can be used to calculate the weight fraction ratios of pairs of elements in a sample. This limiting thickness of a sample is a function of accelerating voltage and sample density. As the accelerating voltage is increased the limiting thickness increases. Hall(63) has found that at 30 kV the limiting thickness has a mass per unit area of about 500 µg/cm^2 and he has estimated that at 100 kV it will be around 1 mg/cm^2. These estimates are in general agreement with the estimated values of Lorimer et al.(60)

The cementite particles in our samples were small enough to satisfy the condition of a 'thin' specimen for the accelerating voltage (80 kV) used. Using a density of 7.6 gm/cm^3 for cementite and the above estimates, the limiting thickness of the cementite particles is 1.3µ at 100 kV and 0.65µ at 30 kV. Since cementite particles in our samples were generally less than 1µ thickness we concluded that all would be 'thin' at an accelerating voltage of 80 kV.

The broad characteristic X-ray peaks which are obtained in the energy dispersive analysis as compared to the wavelength dispersive method can lead to an extra difficulty in the quantitative analysis if the elements being analysed are adjacent to each other in atomic number, because of the overlap of K_α and K_β peaks of these elements. However, for the thin specimens, the ratio of K_β to K_α peaks is constant for a given element. Once these ratios are determined, the problem of overlapping peaks can easily be solved if either the K_α or K_β peak is isolated.(61) In our case, (analysis of Fe and Cr) this problem did not exist.

The carbon extraction replicas were prepared using the method described by Smith and Nutting.(64) The samples were polished and etched with 2% nital so that the structure was readily visible under the optical microscope. A thin carbon film was then evaporated onto the surface. To make the stripping easier the film was scored into small squares with a knife edge while still on the specimen. The specimen was then dipped into 5% nitric acid in ethanol and etched for 5 to 10 minutes, after which the carbon film was stripped by transferring the sample to distilled water. The carbon films were then lifted from the distilled water onto 200 mesh copper grids and were ready to be used. Most of the carbide particles were extracted in each case. For comparison purposes, one pure Fe-C alloy was treated in the α+cm region at 700°C and analysed in a similar manner. The typical extraction replica micrographs are shown in figures (14) to (16).

The Philips EM300 electron microscope at the McMaster University Medical Centre fitted with the EDAX Si[Li] X-ray energy dispersion analysis system was used for the carbide analysis. The geometry of the specimen chamber and the line diagram of the X-ray production and detection is shown in figure (17). A tilt angle of 36° was used for all the measurements. These were carried out at an 80 kV accelerating voltage. After identifying the particle to be analysed the electron beam was focussed on the particle by manipulating the condensers I and II. The minimum beam size of about 0.5μ was easily obtained. Figure (18) shows the typical X-ray spectra obtained. In some cases the cementite particles from the pure Fe-C alloy showed CrK_α counts. However, this number was well within the statistical error of the analysis.

The integrated peak intensities of FeK_α and CrK_α peaks were obtained by using the computer programme EDIT/7EM prepared by EDAX Laboratories. The peaks were statistically smoothed and the background subtracted. Since the elements Fe and Cr are very close to each other in atomic numbers the value of the k factor in equation (II.43) is very close to unity.(61) In our calculations we used the theoretically calculated value of EDAX.(62) The weight fractions of Cr and Fe in cementite were then obtained using equation (II.43). From the scatter of the (I_{Cr}/I_{Fe}) values from the different particles in the same sample, the R.M.S. error in the analysis was estimated to be around ±7% of the amount present. For each particle the analysis was carried out for a sufficiently long time to obtain a statistical counting error of much less than this. This time generally varied from one to two minutes.

To cross-check this method of obtaining the composition of the cementite, an alternative method was followed for the 1.87 atomic % Cr, 3.08 atomic % C alloy treated in the $(\alpha$+cm) region at 700°C for 15 days. The cementite was isolated from the sample by electrolytic extraction using a $CdBr_2$ electrolyte.(66) The residue was then analysed for chromium and iron. It contained 15 weight % chromium. However, the total of chromium, iron and a stoichiometric amount of carbon added to only 95%. The difference from 100% was due to the decomposition of some of the cementite during the electrolytic extraction. Applying a correction for this, the isolated cementite was analysed as 15.5 weight % chromium. This is to be compared with 14.9 weight % chromium obtained with the method described above. Since the agreement is excellent, the simpler and more general extraction replica method was followed for all other measurements.

(ii) Metallography: The volume fraction of the cementite in the alloys containing martensite (formerly austenite) and cementite was determined with the automatic image analyser. The samples were tempered at 200°C for 1 hr to darken the martensite phase. This has no effect on the volume fraction of cementite measured. The composition and the volume fraction of cementite is now known. The composition of the austenite is obtained from the mass balance of chromium and carbon. This leads to complete determination of the tie-lines in the (γ+cm) region.

The tie-lines for the alloys in the (α+cm) region are obtained from the mass balance for carbon and chromium and the composition of cementite. The ferrite phase is assumed to have a carbon concentration the same as obtained from the calculated phase diagram.

(d) The Experiment in the Three Phase Region

A single experiment in the three phase region (α+γ+cm) was carried out at 75 °C. A 1.88 atomic % Cr, 2.73 atomic % C alloy was quenched from the austenite region to produce martensite and then heat treated at 750°C for 36 days. The three phase structure obtained is shown in figure (19). The cementite was analysed as described previously. Because of the fine structure, the ferrite and the martensite (formerly austenite) phases could not be analysed for chromium by the microprobe. The volume fraction of martensite was determined with the automatic image analyser and the volume of cementite was determined by a systematic point count method.

For the complete determination of the compositions of all the three phases by the mass balance we require the chromium content of at least one of the two remaining phases, ferrite and austenite. Since these could not be determined with the techniques available, the comparison with the calculated phase diagram is necessarily a limited one. The experimental values determined above are compared with the ones expected from the calculated phase diagram.

II.7 RESULTS AND DISCUSSION

The experimentally determined tie-lines in the $\alpha+\gamma$ region at 770°C and 750°C are shown in figures (7) and (8), respectively (dotted lines). The results are summarised in table (7). The agreement between the calculated and the experimental phase boundaries is excellent. Nonetheless, the slopes of the tie-lines differ slightly from the calculated values. The maximum difference in $k_{Cr}^{\alpha/\gamma}$ (= $\frac{X_{Cr}^{\gamma}}{X_{Cr}^{\alpha}}$) values is about 10% at 750°C. For the low concentration measurements by the electron microprobe, the minimum statistical R.M.S. error is given by$^{(105)}$

$$\sigma = \frac{100\sqrt{N_p+N_B}}{N_p-N_B} \qquad \text{(II.44)}$$

where N_p is the number of counts of the characteristic radiation (CrK_α in this case), N_B is the number of background counts and σ is the standard deviation. For our measurements on the low chromium alloy this was about 5% which would lead to a standard deviation of about 7% in the $K_{Cr}^{\alpha/\gamma}$, i.e., at a 95% confidence level, the error in the $K_{Cr}^{\alpha/\gamma}$ measurements is ±14%. This does not include other possible experimental errors. Hence, the difference between the slopes of the experimental and calculated tie-lines is insufficient to suggest an error in the independently calculated tie-lines.

The experimentally determined tie-lines in the γ+cm region at 770°C and 750°C are also shown in figures (7) and (8), respectively (dotted lines) and are summarised in table (8). The agreement between the calculated and the experimentally determined phase boundaries as well as the slopes of the tie-lines is very good. The last two columns of table (8) compare the experimental and calculated distribution coefficients for chromium between cementite and austenite. Again, within the experimental error the agreement is excellent.

Table (9) gives the results of the experiments in the α+cm region at 700°C and the summary is given in figure (10). In this case, the phase boundaries are not independently determined but are assumed to be the same as the calculated ones. The cementite phase boundary is fixed and lies at 25 atomic % carbon. The solubility of carbon in α is very small, and could not be determined, hence, the above-mentioned assumption. The best test of the calculated phase diagram in this case therefore lies in correctly predicting the composition of the cementite. In table (9), columns (7) and (8) give the experimental and the predicted chromium content of the cementite for the experimental alloys. The agreement in the two cases is excellent. In the third case the experimental and predicted values are within 10% of each other. The error in the analysis is around ±7%. Hence, the agreement can be said to be fair in this case. Columns (9) and (10) give the experimental and the calculated distribution coefficients of chromium between the cementite and the ferrite. The average of the experimental values is at 53 which is in fair agreement with the average of the calculated values which is ~~at~~ 44.5. Hence, the overall agreement between the experiments in the α+cm region and the independently calculated phase diagram is good.

Table (10) gives the experimental values of the volume fractions of the different phases (γ and cm) and the composition of the cementite phase for the alloy treated in the three phase (α+γ+cm) region at 750°C. The alloy composition is marked in figure (8). These experimental values are compared in table (10) with the values of these parameters that would be expected from the calculated phase diagram (figure (8)) for the given alloy composition. The agreement, as seen from table (10), is good.

The eutectoid temperature as a function of chromium content in the Fe-C-Cr system can be obtained from isothermal spacing experiments for the pearlite reaction. The extrapolation of the 1/S vs T (S is the interlamellar spacing and T is temperature) as a straight line to infinite spacing (i.e., 1/S = 0) should intercept the temperature axis at the eutectoid temperature. Figure (11) shows the experimental points for the eutectoid temperature thus determined from our own (Chapter V) and other experiments.(19). The agreement with the calculated curve is excellent.

In general, the agreement between the calculated phase diagrams and the experiments is very good. The thermodynamics of the Fe-C-Cr system described in the first part of this Chapter is thus used with confidence in subsequent chapters to calculate stable and metastable phase diagrams and to obtain all the other thermodynamic information as a function of temperature which is required to describe the pearlite reaction in the Fe-C-Cr system.

CHAPTER III

THEORY OF PEARLITE GROWTH

III.1 THE Fe-C SYSTEM

Figure (20) shows the binary Fe-C phase diagram calculated from the thermodynamic data of Chapter II. The dashed lines define the region where the pearlite reaction takes place. During the pearlite reaction the γ phase decomposes cooperatively into a lamellar structure of α and cm. This lamellar structure grows into the untransformed γ phase at constant velocity during an isothermal experiment. Following the early attempt of Zener$^{(10)}$ to describe the pearlite growth on the basis of carbon volume diffusion, the problem of pearlite growth by volume diffusion has been rigorously treated by subsequent workers. Because of an apparent disagreement between the volume diffusion theory of pearlite growth and the experimental observations, a number of workers have investigated the problem on the basis of the boundary diffusion of carbon and other mechanisms. Recently, Puls and Kirkaldy$^{(15)}$ have taken account of the variation of the carbon diffusion coefficient in austenite with concentration of carbon and shown that the volume diffusion model satisfactorily describes the pearlite growth data in Fe-C at higher temperatures. The partial involvement of boundary diffusion at lower temperatures is not ruled out. In the following we will briefly describe the volume and boundary diffusion models.

(a) Volume Diffusion Model

Figure (21a) shows schematically the pearlite-austenite interface. Local equilibrium is assumed to exist across this interface. In the case of cooperative precipitation, such as edgewise lamellar growth, there exists a situation at the junction of the two lamellae where three phases must exist in local equilibrium below the eutectoid temperature. This is achieved through the modification of the phase diagram due to capillarity. In this way, the concentration of the parent phase can vary smoothly across the junction. At the three phase junction the mechanical equilibrium of the surface tension forces must be simultaneously accommodated. It is therefore essential to admit a curvature of the interface between the parent and the product phases. The local radius of curvature generates a pressure which is assumed to act mainly on the product phases. This leads to a variation of composition along the interface, which is everywhere in local equilibrium.

A simplified theory accounting for these considerations was first put forward by Zener.(10) If the ferrite-austenite and the cementite-austenite interfaces were flat, the concentration difference which provides the driving force for diffusion would be $(C_0^{\gamma\alpha}-C_0^{\gamma cm})$, where $C_0^{\gamma\alpha}$ and $C_0^{\gamma cm}$ are the equilibrium concentrations according the the phase diagram for austenite in contact with ferrite and cementite, respectively. It was conjectured by Zener that the capillarity modified difference can be approximately represented by $(1-\frac{S_0}{S})(C_0^{\gamma\alpha}-C_0^{\gamma cm})$ where S is the interlamellar spacing and S_0 is the critical interlamellar spacing. S_0 is a function of temperature only. At the critical interlamellar spacing no concentration difference exists, the thermodynamic driving force for the pearlite reaction is exactly balanced by the interfacial energy stored in the α-cm interfaces and the velocity necessarily goes to zero.

Further, Zener supposed that the effective distance for diffusion up to the edge of a cementite lamella is proportional to its thickness, so the flux

$$J = -D\frac{dC}{dX} \cong -D\,\frac{C_0^{\gamma\alpha}-C_0^{\gamma cm}}{aS^{cm}}\left(1-\frac{S_0}{S}\right) \qquad (III.1)$$

or from the mass balance

$$J = -v(C^{cm}-C^{\alpha}) \qquad (III.2)$$

where v is the pearlite growth rate and C^{cm} and C^{α} are the concentrations of the cementite and the ferrite, respectively. From the lever rule

$$S^{\alpha}(C_{\infty}-C^{\alpha}) = S^{cm}(C^{cm}-C_{\infty}) = \frac{S^{cm}S^{\alpha}}{S}(C^{cm}-C^{\alpha}) \qquad (III.3)$$

so a combination of equations (III.1), (III.2) and (III.3) yields

$$v = \frac{D}{a}\,\frac{S^2}{S^{\alpha}S^{cm}}\,\frac{(C_0^{\gamma\alpha}-C_0^{\gamma cm})}{(C^{cm}-C^{\alpha})}\,\frac{1}{S}\left(1-\frac{S_0}{S}\right) \qquad (III.4)$$

Brandt(67) and Scheil(68) were the first to construct a comprehensive volume diffusion model for the pearlite transformation. A more rigorous calculation based on Brandt's series solution, but including capillarity, has been performed by Hillert.(11,69) He also achieved a detailed prediction of the interface shape. Bolze et al.(14) generalised Hillert's volume diffusion model to take into account the non-uniformity of concentration in the product phases which results from a variation of curvature along the pearlite austenite interface. The Hillert and Bolze et al. treatments are briefly summarised below.

First we consider the effect of the curved interface on the equilibrium compositions. A curved interface gives rise to a pressure difference, ΔP, between the two sides of the interface, which is related to the interfacial energy, σ, by

$$\Delta P = \sigma\left(\frac{1}{r_1} + \frac{1}{r_2}\right) \tag{III.5}$$

where r_1 and r_2 are the two principle radii of curvature of the interface.

Two phases α and γ in equilibrium in a binary system having the compositions $(X_1^{\gamma\alpha}, X_2^{\gamma\alpha})$, $(X_1^{\alpha\gamma}, X_2^{\alpha\gamma})$ and the activities of the two components a_1 and a_2 satisfy the Gibbs-Duhem relations

$$X_1^{\gamma\alpha} d\ln a_1 + X_2^{\gamma\alpha} d\ln a_2 = \frac{V_m^{\gamma}}{RT}\, dP^{\gamma} \tag{III.6}$$

and

$$X_1^{\alpha\gamma} d\ln a_1 + X_2^{\alpha\gamma} d\ln a_2 = \frac{V_m^{\alpha}}{RT}\, dP^{\alpha} \tag{III.7}$$

Assuming $dP^{\gamma} = 0$, the molar volumes of the γ and the α phases V_m^{γ} and V_m^{α} to be equal to each other, $d\ln a_1 \stackrel{*}{\simeq} d\ln X_1^{\alpha\gamma}$ and low undercoolings the above equations can be solved to yield(14)

$$P^{\alpha} = RTk_{\alpha}(C_{10}^{\alpha\gamma} - C_1^{\alpha\gamma}) \tag{III.8}$$

or in terms of the concentrations in the γ phase

$$P^{\gamma} = RTh_{\alpha}(C_{10}^{\gamma\alpha} - C_1^{\gamma\alpha}) \tag{III.9}$$

where $C_{10}^{\alpha\gamma}$ and $C_{10}^{\gamma\alpha}$ refer to the concentrations for the flat interface and k_{α} and h_{α} are constants related to the phase diagram. Similar expressions for the m phase are obtained.

For the steady state pearlite reaction occurring at velocity, v, the diffusion problem is two dimensional. To obtain a steady state solution of the diffusion equations, a translation of the frame of reference is made via (figure (21a))

$$u = x - vt \tag{III.10}$$

In this frame the diffusion equation for solute concentration is

$$-v \frac{\partial C}{\partial u} = D\left(\frac{\partial^2 C}{\partial x^2} + \frac{\partial^2 C}{\partial y^2}\right) \tag{III.11}$$

For boundary conditions we have $C = C_\infty$ at $u = \infty$ for all y and $C(y) = C(y+S)$ for all u. We thus obtain the solution:

$$C = C_\infty + \Sigma_0^\infty A_n e^{\lambda_n u} \cos b_n y \tag{III.12}$$

where

$$b_n = \frac{2\pi n}{S} \tag{III.13}$$

and

$$\lambda_n = \frac{v}{2D}\left(1 + \sqrt{\frac{1 + 4b_n^2 D^2}{v^2}}\right) \tag{III.14}$$

Hillert has suggested that for all interesting experimental situations $\frac{2\pi nD}{Sv} >> 1$, so that to a very good approximation

$$\lambda_n \cong -b_n\left(1 + \frac{v}{2Db_n}\right) \tag{III.15}$$

Now considering a mass balance in a small strip of volume of width, dy, we obtain two expressions of the form

$$v(C_\infty - C_p) = -D \int_{u_o}^{\infty} \frac{\partial^2 C}{\partial y^2}\, du \qquad \text{(III.16)}$$

In this, C_p is the concentration in the product phase (α or cm). Possible diffusion in the product phases is ignored. Using the expression for C from equation (III.12) and making the assumption that the interface is approximately flat so that $e^{\lambda_n u_o(y)} \simeq 1$, equation (III.16) becomes

$$v(C_\infty - C_p) = -D\, \Sigma_1^\infty \frac{A_n b_n^2}{\lambda_n} \cos b_n y \qquad \text{(III.17)}$$

To complete the solution of the problem, the balance of surface tension forces at the three phase junction is utilised, viz.,

$$\frac{\sigma^{\alpha\gamma}}{\sin\phi^{cm}} = \frac{\sigma^{\gamma cm}}{\sin\phi^{\alpha}} = \frac{\sigma^{\alpha cm}}{\sin\phi^{\gamma}} \qquad \text{(III.18)}$$

The terms in equation (III.18) are defined in figure (21a). If the interface between α and cm is assumed to be parallel to the u axis, the above boundary conditions can be expressed as:

$$-\cos\phi^\alpha = \int_0^{S^\alpha/2} \frac{P^\alpha}{\sigma^{\alpha\gamma}}\, dy \qquad \text{(III.19a)}$$

and

$$-\cos\phi^{cm} = \int_{S^\alpha/2}^{S/2} \frac{P^{cm}}{\sigma^{\gamma cm}}\, dy \qquad \text{(III.19b)}$$

Substituting the expressions for P^α and P^{cm} expressed in terms of the concentrations in the phase (equation (III.9)) into equations (III.19a) and (III.19b), and integrating gives:

$$-\frac{2}{RT}\frac{\sigma^{\alpha\gamma}\cos\phi}{S\,h_{\alpha}} = C_0^{\gamma\alpha}-C_\infty^{\gamma}-A_0-\frac{2}{S^{\alpha}}\Sigma_1^{\infty}\frac{A_n}{b_n}\sin(n\frac{S^{\alpha}}{S}) \qquad \text{(III.20)}$$

and

$$-\frac{2}{kT}\frac{\sigma^{cm\gamma}\cos\ \frac{cm}{}}{S^{cm}h_{cm}} = C_0^{\gamma cm}-C_\infty^{\gamma}-A_0+\frac{2}{S}\Sigma_1^{\infty}\frac{A_n}{b_n}\sin(n\pi\frac{S^{\alpha}}{S}) \qquad \text{(III.21)}$$

Now equations (III.17), (III.20) and (III.21) can be combined to give a v vs S relationship. Hillert, assuming a uniform concentration in the product phases, arrived at the solution

$$v = \frac{D\pi^3}{B}\frac{S^{\alpha}S^{cm}}{S^2}\frac{(C_0^{\gamma\alpha}-C_0^{\gamma cm})}{C^{cm}-C^{\alpha}}\frac{1}{S}(1-\frac{S_0}{S}) \qquad \text{(III.22)}$$

where

$$B = \Sigma_1^{\infty}\frac{\lambda_n S}{2\pi n^4}(\sin\pi n\frac{S}{S})^2$$

Bolze et al.,$^{(14)}$ taking into account the concentration variation in the product phases, arrived at the relation

$$v = \Omega\frac{1}{S}\frac{(1-\frac{S_0}{S})}{(1+\frac{\phi}{S})} \qquad \text{(III.23)}$$

where the coefficient Ω is essentially the same as Hillert's and where the term $(1+\frac{\phi}{S})$ in the denominator represents the effect of non-uniform concentrations in the product phases. ϕ is interpreted as representing the free energy stored via solute segregation in the product phases. It was also shown that the effect of this segregation for systems with low solute solubility in the terminal phases is very small. Hence the Hillert approximation is adequate for the Fe-C system.

For given values of S and v equation (III.12) can be solved for C^γ. Once C^γ is known the pressure difference between the γ and α (or cm) can be calculated assuming local equilibrium across the interface. If the interfacial free energies are known equation (III.19) can then be solved for the detailed shape of the interface. Figure (21b) shows the results of such a calculation for the Fe-C system performed by Hillert.

(b) Boundary Diffusion Model

The boundary diffusion model for lamellar growth was first applied to the problem of discontinuous precipitation by Turnbull(12) and by Cahn.(13) Various attempts to invoke boundary diffusion control in eutectoid reactions have since been made. In the case of the eutectoid reaction in the Fe-C system the carbon is assumed to diffuse through a pearlite-austenite boundary of thickness δ and diffusion coefficient D_B. To a first approximation the growth equation for pearlite can be obtained from the volume diffusion model by substituting a boundary diffusion coefficient, D_B, for the volume diffusion coefficient, D, and decreasing the "window" for lateral diffusion" 1/S by the ratio δ/S. This leads to

$$v \propto \frac{D_B \delta}{S^2}\left(1 - \frac{S_0}{S}\right) \qquad \text{(III.24)}$$

A more comprehensive solution for the boundary diffusion model has been obtained by Hillert(11,69) and by Shapiro and Kirkaldy.(70) Considering the mass balance in a thin strip of material parallel to the α-cm interface, we obtain

$$-\int_{-\infty}^{\infty} D \frac{\partial^2 C}{\partial y^2} dy = D_B \frac{d^2 C^B}{dy^2} \delta = v(C^\gamma - C^{\alpha;cm}) \qquad (III.25)$$

where C^B is the concentration in the boundary. Assuming the concentrations in the α and cm to be constant and $C^B = KC^\gamma$, where K is an adsorption coefficient, the above equation can be easily integrated. Using these solutions along with equations (III.19) Hillert obtained the following velocity equation:

$$v = 12\, KD_B\delta \frac{S^2}{S^\alpha S^{cm}} \frac{(C_o^{\gamma\alpha} - C_o^{\gamma cm})}{C^{cm} - C^\alpha} \frac{1}{S^2} (1 - \frac{S_o}{S}) \qquad (III.26)$$

Shapiro and Kirkaldy, following a more rigorous but less general argument obtain for a symmetric eutectoid

$$v = 24\, \delta D_B \frac{(C_o^{\gamma\alpha} - C_o^{\gamma cm})}{1/2 - a} \frac{1}{S^2} (1 - \frac{S_o}{S}) \qquad (III.27)$$

where

$$D_B = 2qVL \qquad (III.28)$$

q and a are equilibrium thermodynamic parameters obtained from the free energy composition diagram, V is the molar volume and L is the Onsager phenomenological coefficient (mobility) for boundary diffusion.

The boundary diffusion models are difficult to test quantitatively against experiments because of the lack of knowledge of the boundary diffusivity and the nature of the boundary phase. However, semi-quantitative comparisons based on the functional relation between v and S and the Arrhenius behaviour can be made.

(c) Problem of the Optimum Spacing

The theories of pearlite growth based on either volume diffusion or boundary diffusion lead to a single relation between the spacing, S, velocity, v, and the undercooling, ΔT. Since in an experiment either v or ΔT, but not both can be fixed, the spacing is not uniquely determined by the diffusion solution. To get a unique solution of the problem we require a further condition. This usually takes the form of an optimization principle.

Zener$^{(10)}$ originally proposed the maximum velocity principle, i.e., in an isothermal experiment, pearlite chooses a spacing corresponding to the maximum in the v vs S curve. This is based on the intuitive, but incorrect reasoning that the areas of the pearlite front which have a spacing less or more than the one corresponding to the maximum in v will lag behind and eventually vanish. Zener's criterion leads to the optimum spacing of 2 S_o for the volume diffusion model and 1.5 S_o for the boundary diffusion model. Initially this had been accepted as the practical solution to the problem. However, in the past 15 years a number of workers have turned to perturbation tests and irreversible thermodynamic arguments to gain more insight into the spacing optimization problem in eutectic and eutectoid reactions.$^{(13,71-75)}$ These studies have been reviewed by Puls and Kirkaldy.$^{(15)}$ We will briefly summarise the results below.

Cahn,$^{(13)}$ following an approach originally expounded by Frank and Puttick,$^{(74)}$ argued that if we analytically impose a perturbation on the local spacing of forced eutectics it can be inferred that spacings less than for minimum undercooling are inherently unstable, while spacings greater than for ΔT_{in} are inherently stable. A similar argument can be constructed for isothermal pearlite which suggests that the stability point is for $S > S(v_{max})$. Sundquist,(75) in investigating shape changes of the lamellar front within the range of the steady state v vs S relation, has discovered that for $S(v_c) >> S(v_{max})$ the diffusion solutions become non analytic implying a catastrophic instability. Kirkaldy(7[illegible]) used a "half-spacing" perturbation procedure, combining elements of Cahr's and of Jackson and Chalmer's(71) arguments, to arrive at an optimum spacing for the isothermal pearlite. For each quasi-steady configuration he envisages a region of a colony front which, via nucleation or overgrowth, has achieved a spacing exactly one-half of that for the colony generally. An examination of the analytic relaxation of such a perturbation for all spacings uniquely identifies a stability point at that spacing for which a short region of the front which has one-half the average spacing has the same velocity as the average. For pearlite growth by volume diffusion this gives a stability point at a spacing of 3 S_o and for the boundary diffusion model a stability point at 7/3 S_o.

Kirkaldy(76,77) has also concluded that a maximum in the rate of entropy production consistent with Onsager's Dissipation Theorem(78) is the best thermodynamic criterion for defining the optimum spacing. For the steady state growth of pearlite the rate of entropy production is

$$\frac{d_iS}{dt} = -v \cdot \frac{\Delta F}{T} \qquad \text{(III.29)}$$

where

$$\Delta F \propto (1- \frac{S_o}{S}). \qquad \text{(III.30)}$$

For isothermal pearlite growing according to the volume diffusion model this gives:

$$\frac{d_i S}{dt} \alpha \frac{1}{S} (1 - \frac{S_o}{S})^2 \qquad \text{(III.31)}$$

which is maximum at $S = 3\ S_o$ and for the boundary diffusion model

$$\frac{d_i S}{dt} \alpha \frac{1}{S^2} (1 - \frac{S_o}{S})^2 \qquad \text{(III.32)}$$

which is maximum at $S = 2\ S_o$.

The optimum spacing obtained from a maximum in the rate of entropy production is therefore the same, or very nearly the same, as that obtained from the perturbation analysis.

(d) Comparison between Theory and Experiments

Early comparisons between the experimental growth rates of pearlite in Fe-C and theoretical values based on the volume diffusion model were unsuccessful. The experimental values seemed to be generally an order of magnitude higher than the calculated ones. This led Cahn and others to suggest that the major part of the carbon diffusion takes place through the boundary layer separating the pearlite and the austenite. However, Brown and Ridley,(79) assuming volume diffusion control, back-calculated the effective carbon diffusivity in austenite from the pearlite growth data and found D_C values only 2 to 4 times higher than the experimental diffusion coefficients. They also found that for small undercoolings the effective D_C almost remains constant with decreasing temperature. Kirkaldy and Puls attributed this to the fact that the diffusion coefficient of carbon in austenite is strongly concentration dependent.(15,103) They therefore re-calculated the pearlite growth rates in Fe-C using Hillert's volume diffusion model and taking into account the variation of carbon diffusion coefficient in austenite with carbon concentration and found that the volume diffusion calculations agree with the experimental values within a factor of 2 between 727° and 650°C. They also concluded that below this temperature involvement of boundary diffusion begins and eventually takes over as the temperature is further lowered.

Puls and Kirkaldy(15) also calculated the interfacial free energy, $\sigma^{\alpha cm}$, between α and Cm from the interlamellar spacing measurements of Brown and Ridley,(79) the volume diffusion theory of Hillert and the principle of maximum entropy production and arrived at a value of $\sigma^{\alpha cm}$ = 00 ergs/cm^2. This was regarded as a salutary result since this value corresponds to an incoherent interface and is consistent with the observation of Bolling and Richman(80) that pearlite can change direction smoothly without a change in the spacing.

In final conclusion, the agreement between theory and experiment for the pearlite growth process in Fe-C appears to be good.

III.2 Fe-C-X SYSTEMS

The rigorous treatment of the diffusion equations and the thermodynamics for pearlite growth in Fe-C-X systems is intractable. Bolze(81) investigated the problem for the volume diffusion model so as to accommodate a wide range of constitutions and ternary interactions. Unfortunately, he was only able to obtain a tractable and transparent result for rather unrealistic physical conditions. Hillert(82) has recently treated the problem of ternary eutectoid growth for a group of ternary models (both solutes moving via volume diffusion, both via boundary diffusion and one via boundary and the other via volume diffusion). The author, however, made no attempt to relate his solutions explicitly to real or schematic phase diagrams, making even a qualitative relative appraisal difficult.

In the case of pearlite growth with no partitioning of the alloying element, X, the solutions for the binary Fe-C system with an appropriate modification of the driving force can be used (see a detailed discussion in Chapter IV). Puls and Kirkaldy(15) have qualitatively explained the growth rates of pearlite in the Fe-C-Mn and the Fe-C-Ni systems in this manner. In the case where the alloying element partitions, the diffusion of carbon as well as the alloying element must be taken into account. Since the partitioning reaction takes place at higher temperatures, carbon most probably diffuses through the volume. However, to obtain the growth rates encountered in the experiments we must at the same time assume that the alloying element diffuses through the boundary. Kirkaldy(6) has semi-empirically taken this into account by combining the volume diffusion for carbon and the boundary diffusion for the alloying elements via a heat transfer analogy. More discussion of the growth of pearlite in Fe-C-X systems is given in the next chapter.

CHAPTER IV

THERMODYNAMIC AND KINETIC CONSIDERATIONS PERTAINING TO THE PARTITIONING OF ALLOYING ELEMENTS DURING THE DECOMPOSITION OF AUSTENITE

IV.1 INTRODUCTION

The behaviour of the alloying elements during the austenite decomposition reactions has been the subject of extensive theoretical and experimental investigation. In Fe-C-X systems, where X is a substitutional alloying element, carbon volume diffusion is much faster than the diffusion of alloying elements. Under such conditions the diffusion-controlled austenite decomposition reactions can take place in one of two ways. In the first case the alloying element is partitioned between the parent (austenite) phase and the product phase (or phases). We will call such a reaction a partitioning reaction. In this case the reaction is slowed down considerably because of the relitively slow diffusion of the alloying element involved. In the second case, the alloying undergoes no long range diffusion and the ratio of the alloying element to iron remains the same in the product phase (or phases) as in the parent phase. The reaction in this case is controlled by the diffusion of carbon. An alloying element affects the reaction kinetics only through its thermodynamic influence on the driving force for the reaction. We will call such a reaction a no-partition reaction. In general, the partitioning reaction must take place at low supersaturations while the no-partitioning reaction can take place at high supersaturations. The actual temperature of the partition - no-partition transition, if it exists, depends on the alloy system and composition.

IV.2 EXPERIMENTAL [illegible] FOR THE PARTITION - NO-PARTITION TRANSITION

In the literature there is considerable evidence for a partition - no-partition transition. Bowman(83) in 1946 reported that zero partition of molybdenum was detected during the formation of pro-eutectoid ferrite in a number of Fe-C-Mo alloys transformed between 650° and 750°C. Aaronson and Domian(58) have recently studied the partition of the alloying elements between austenite and pro-eutectoid ferrite (or bainite) in a number of Fe-C-X systems. They detected zero partition of X between the austenite and the pro-eutectoid ferrite during the initial stages of transformation at every temperature studied in the case of Si, Mo, Al, Cr and Cu steels. However, they observed partitioning of X between austenite and pro-eutectoid ferrite at temperatures above an individually characteristic critical temperature in Mn, Ni and Pt steels. Purdy et al.(84) have studied the pro-eutectoid ferrite reaction in a number of Fe-C-Mn alloys and found zero partitioning of Mn at high supersaturations, while there was definite evidence of partitioning at low supersaturations. If the reaction in the high supersaturation, no-partition region is allowed to proceed for long times, the alloying element will eventually partition towards the thermodynamic equilibrium values. This has been studied by Gilmour et al.(85) in the Fe-C-Mn system and by Sharma and Kirkaldy(86) in the Fe-C-Ni system for the pro-eutectoid ferrite reaction.

The partitioning of the alloying elements during the pearlite reaction is a much more difficult problem to study experimentally. Firstly, because of the very small pearlite spacing, the electron microprobe cannot be used and the method of extraction and chemical analysis of carbides is affected by the partitioning between ferrite and cementite behind the transforming interface, which necessarily leads to a deviation from the amount of partitioning that occurred at the reaction front. Nonetheless, quite a few attempts have been made to study partitioning during the pearlite reaction. Bowman(18) observed partitioning of Mo between ferrite and cementite in pearlite formed in Fe-C-Mo alloys down to 600°C. Picklesimer et al.(16) observed that Mn partitions between the ferrite and cementite during the pearlite reaction in an Fe-C-Mn alloy at low supersaturations but not at high supersaturations. However, they were unable to accurately determine the partion - no-partition tran ition temperature. Recently, Razik et al.(17,19) have studied the partitioning of Mn and Cr during the pearlite reaction using the analytic electron-microscope EMMA-4. In both cases they observed partitioning at low supersaturations and zero partitioning at high supersaturations. These appear to be the most reliable results on the partitioning of alloying elements during the pearlite reaction reported in literature thus far.

IV.3 THEORETICAL INTERPRETATION

The problem of partitioning of alloying elements during the austenite to ferrite (or cementite) transformation has been extensively studied theoretically. Hultgren in 1951(87) first suggested that two types of ferrite could form during the isothermal decomposition of austenite in alloy steels. He noted that at relatively low supersaturations the kinetics of transformation were slow while at higher supersaturations they were much faster and that the high and low supersaturation data could in many cases be represented by separate C-curves on the TTT diagrams. He proposed, therefore, that at low supersaturations the interface is in local equilibrium and the transformation required the equilibrium redistribution of the alloying elements. The ferrite produced under such conditions was called orthoferrite by Hultgren. At low temperatures, i.e., high supersaturations, the slow diffusing alloying elements could not redistribute and thus the transformation would proceed under carbon diffusion control, precipitating the ferrite of the same alloying content as the austenite. He called this non-equilibrium product, paraferrite. Since this early work of Hultgren, it has been found that the double C-curve does not necessarily imply that the alloying element partitions in the region of the upper C-curve.(88) Other reasons for the double C-curve (or the 'bay' in the C-curve) found in certain alloy systems have been suggested(9,69,88) but we will not go into the details here. However, the general conclusion of Hultgren, that during the pro-eutectoid ferrite reaction the alloying elements partition at relatively low supersaturations and not at higher supersaturations, remains valid.

Hillert(89) and Rudberg(90) have discussed the position of the para-equilibrium phase boundaries in ternary, Fe-C-X alloy systems in more detail. Hillert(69) has shown that the para-equilibrium phase boundaries can be calculated from a knowledge of the free energy surfaces. A true para-equilibrium tie-line must satisfy the criterion that the chemical potential of the high mobility element (carbon) must be the same in both of phases (austenite and ferrite). While the ratio of the alloying element to iron remains constant in both phases $\left(\frac{X_X^\alpha}{X_{Fe}^\alpha} = \frac{X_X^\gamma}{X_{Fe}^\gamma}\right)$. The para-equilibrium boundaries must lie within the thermodynamically stable two phase field. Gilmour et al.(55) and Sharma and Kirkaldy(86) have calculated such para-equilibrium boundaries for the Fe-C-Mn and the Fe-C-Ni system from basic thermodynamic data. Such calculations for the Fe-C-Cr system will be considered later in this chapter. A schematic representation of para-equilibrium boundaries is shown in figure (22).

Another way in which a no-partition reaction can take place is called the local equilibrium no-partition condition. This has been described by Kirkaldy,(91) Hillert(69) and others. Under this condition the precipitating phase, during a diffusion controlled transformation in a Fe-C-X alloy, may have substantially the same alloying element composition as the original austenite phase and still maintain a complete chemical equilibrium at the interface. Kirkaldy(91) published solutions to the diffusion equations for transformations in ternary alloys assuming local equilibrium at the interface. Purdy et al.(84) extended these solutions of the diffusion equations for the Fe-C-Mn system to show that at low supersaturations these solutions predict manganese partition and low growth rates due to manganese diffusion control, while at higher supersaturations the manganese need not partition and the transformation would be controlled by carbon diffusion. The position of this local equilibrium partition - no-partition boundary in the ternary Fe-C-X phase diagrams has been further considered by Hillert,(69) Gilmour,(38) Coates(92,93) and others. The construction of such a boundary is schematically shown in figure (23). The intersection of the carbon component ray ($\frac{X_X}{X_{Fe}}$ = constant line) from the ferrite end of a tie-line in the stable $\alpha+\gamma$ two phase field and the extrapolation of the carbon iso-activity line in austenite from the austenite end of the tie-line define a point on the partition - no-partition boundary. The locus of such points divides the two phase ($\alpha+\gamma$) region into partition and no-partition regions. Figure (24), taken from Gilmour's(38) thesis, shows the concentration profiles during the diffusion transformation, $\gamma \rightarrow \alpha$, in the Fe-C-Mn system in the low and high supersaturation regions.

In the high supersaturation no-partition range, the two no-partition conditions described above could exist. Which of these two possible conditions actually operate and under what circumstances has not been completely determined. However, the problem has been discussed by Hillert,(69) Gilmour(38) and Coates.(92,93) The local equilibrium model, in general, looks more attractive because it postulates a thermodynamic equilibrium across the interface where the mobility of atoms, in general, is much higher than in the bulk. However, at high reaction rates or very early times the alloying element diffusion profile (spike) width in front of the growing interface calculated according to the local equilibrium model approaches atomic dimensions or less.(38,92,93) In such a case the local equilibrium model becomes ambiguous, so the reaction may proceed under these conditions according to the para-equilibrium model. Figure (25), taken from Gilmour's thesis, schematically shows the possible operative regions for the various conditions. In general, the transition between a para-equilibrium and a local equilibrium no-partition condition should depend on the precipitation size (i.e., the time of reaction) and the supersaturation.(92,93)

The above discussion summarises the present state of theoretical development of the partitioning problem. The same discussion also applies to the austenite → cementite transformation.

In the rest of this chapter, the thermodynamic predictions of the para-equilibrium and local equilibrium no-partition boundaries for the Fe-C-Cr system for austenite → ferrite and austenite → cementite transformations are given, followed by a general discussion of the partitioning problem in the pearlite reaction in the Fe-C-Cr system.

IV.4 CALCULATION OF THE PARA-EQUILIBRIUM BOUNDARIES IN Fe-C-Cr

The thermodynamic conditions defining para-equilibrium for austenite → ferrite, as discussed in the previous section, are given by:

$$\overline{G}_C^\alpha = \overline{G}_C^\gamma \tag{IV.1}$$

$$X_{Fe}^\alpha \overline{G}_{Fe}^\alpha + X_{Cr}^\alpha \overline{G}_{Cr}^\alpha = X_{Fe}^\gamma \overline{G}_{Fe}^\gamma + X_{Cr}^\gamma \overline{G}_{Cr}^\gamma \tag{IV.2}$$

and

$$\frac{X_{Fe}^\alpha}{X_{Cr}^\alpha} = \frac{X_{Fe}^\gamma}{X_{Cr}^\gamma} = \text{constant} \tag{IV.3}$$

All symbols and numerical values are as defined in Chapter II. By substituting for the partial molar quantities in the above equations, we get:

$$\frac{Y_C^\gamma}{Y_C^\alpha}\frac{1-Y_C^\alpha}{1-Y_C^\gamma} = \exp[\frac{1}{RT}({}^oG_C^\alpha - {}^oG_C^\gamma) + \frac{1}{RT}(L_{CCr}(\frac{1}{3}Y_C^\alpha - Y_{Cr}^\gamma) + 2Y_C^\gamma L_{CV}^\gamma)] \tag{IV.4}$$

$$\frac{1-Y_C^\gamma}{(1-Y_C^\alpha)^3} = \exp[\frac{1}{RT}(Y_{Fe}({}^oG_{Fe}^\alpha - {}^oG_{Fe}^\gamma) + Y_{Cr}({}^oG_{Cr}^\alpha - {}^oG_{Cr}^\gamma))$$

$$+ \frac{1}{RT}(Y_{Fe}Y_{Cr}(L_{FeCr}^\alpha - L_{FeCr}^\gamma) - L_{CV}^\gamma(Y_C^\gamma)^2)] \tag{IV.5}$$

and

$$\frac{Y_{Fe}^\alpha}{Y_{Cr}^\alpha} = \frac{Y_{Fe}^\gamma}{Y_{Cr}^\gamma} = \frac{Y_{Fe}}{Y_{Cr}} = \text{constant} \tag{IV.6}$$

Equations (IV.4) to (IV.6) are solved for a number of given Y_{Cr}/Y_{Fe} ratios to give the para-equilibrium two phase field, α+γ, for a given temperature by computer iteration. The results of such calculations for 750° and 770°C are shown in figures (26) and (27), respectively.

For austenite → cementite the thermodynamic conditions defining para-equilibrium are:

$$Y_{Fe}\overline{G}^{\gamma}_{Fe} + Y_{Cr}\overline{G}^{\gamma}_{Cr} + \frac{1}{3}\,\overline{G}^{\gamma}_{C} = \Delta G^{\gamma}_{(FeCr)C_{1/3}} \qquad \text{(IV.7)}$$

and

$$\frac{X^{\gamma}_{Fe}}{X^{\gamma}_{Cr}} = \frac{X^{cm}_{Fe}}{X^{cm}_{Cr}} = \text{constant} \qquad \text{(IV.8)}$$

All symbols and numerical values are again as defined in Chapter II. Substituting for the partial molar quantities and for the free energy of formation of $(FeCr)C_{1/3}$ in the above equations we get:

$$\begin{aligned}(Y^{\gamma}_{C})^{1/3}(1-Y^{\gamma}_{C})^{2/3} = \exp\Big[&\frac{1}{RT}(Y_{Fe}\Delta^{o}G^{\gamma}_{FeC_{1/3}} + Y_{Cr}\Delta^{o}G^{\gamma}_{CrC_{1/3}})\\ &+ \frac{1}{RT}(Y_{Fe}Y_{Cr}(A_{cm}-L^{\gamma}_{FeCr}) + L^{\gamma}_{CV}(\frac{2}{3}\,Y^{\gamma}_{C}-(Y_{C})^{2})\\ &- \frac{1}{3}\,L^{\gamma}_{CCr}Y_{Cr})\Big]\end{aligned} \qquad \text{(IV.9)}$$

and

$$\frac{Y^{\gamma}_{Fe}}{Y^{\gamma}_{Cr}} = \frac{Y^{cm}_{Fe}}{Y^{cm}_{Cr}} = \frac{Y_{Fe}}{Y_{Cr}} = \text{constant} \qquad \text{(IV.10)}$$

Equation (IV.9) is solved for Y_C^γ for a series of given values of Y_{Fe}/Y_{Cr}, generating a para-equilibrium $\gamma/(\gamma+cm)$ phase boundary. Results for 750° and 770°C are shown in figures (26) and (27), respectively.

IV.5 CALCULATION OF THE LOCAL EQUILIBRIUM NO-PARTITION BOUNDARIES IN Fe-C-Cr

The local equilibrium no-partition boundary is calculated from the intersection of the isoactivity line of carbon in austenite from the austenite end of the tie-line and the carbon component ray ($\frac{X_{Fe}}{X_{Cr}}$ = constant) from the ferrite (or cementite) end of the tie-line as shown in figure (23). Mathematically, the local equilibrium no-partition boundary conditions can be written as follows

$$RT\ln\frac{Y_C^{\gamma N}}{1-Y_C^{\gamma N}} + Y_{Cr}^{\gamma N}L_{CCr}^{\gamma} - 2L_{CV}^{\gamma}Y_C^{\gamma N} = RT\ln\frac{Y_C^{\gamma}}{1-Y_C^{\gamma}} + Y_{Cr}^{\gamma}L_{CCr}^{\gamma} - 2L_{CV}^{\gamma}Y_C^{\gamma} \quad (IV.11)$$

and

$$\frac{Y_{Cr}^{\gamma N}}{Y_{Fe}^{\gamma N}} = \frac{Y_{Cr}^{\alpha}}{Y_{Fe}^{\alpha}} \quad \text{for } \alpha\text{-}\gamma \text{ equilibrium} \quad (IV.12)$$

or

$$\frac{Y_{Cr}^{\gamma N}}{Y_{Fe}^{\gamma N}} = \frac{Y_{Cr}^{cm}}{Y_{Fe}^{cm}} \quad \text{for } \gamma\text{-cm equilibrium} \quad (IV.13)$$

where $Y_{Cr}^{\gamma N}$, $Y_C^{\gamma N}$ and $Y_{Fe}^{\gamma N}$ are the local equilibrium no-partition boundary concentrations and Y_{Cr}^{α}, Y_{Fe}^{α}, Y_{Cr}^{γ}, Y_{Fe}^{γ}, Y_C^{γ} are the equilibrium tie-line concentrations in the ($\alpha+\gamma$) field and Y_{Cr}^{cm}, Y_{Fe}^{cm}, Y_{Cr}^{γ}, Y_C^{γ} are the equilibrium tie-line concentrations in the (γ+cm) field. Once the equilibrium tie-lines are known, equation (IV.11) can be readily solved for the local equilibrium no-partition boundary. This calculation has been carried out for the α-γ and the γ-cm equilibrium and the results for 750° and 770°C are shown in figures (26) and (27), respectively.

IV.6 PARTITIONING DURING THE PEARLITE REACTION

In the preceding sections of this chapter we have calculated the para-equilibrium and local equilibrium no-partition boundaries for the planar precipitation of ferrite and cementite. Figure (28) schematically shows the general regions of partition, no-partition reactions in the Fe-C-Cr system in the range where the pearlite reaction, $\gamma \rightarrow \alpha + C_m$, is feasible. A para-equilibrium or local equilibrium no-partition eutectoid point on such a diagram can easily be defined as shown in figure (27). The variation of these eutectoid points with chromium content are shown in figure (29). It is seen from figure (29) that the para-equilibrium and local equilibrium no-partition eutectoid temperatures are not only lower than the equilibrium eutectoid temperature, as would be expected, but are also lower than the binary Fe-C eutectoid temperature and decrease as the chromium content increases. For a given chromium content the local equilibrium no-partition eutectoid temperature is lower than the para-equilibrium eutectoid temperature. Hence a completely carbon controlled pearlite reaction in an Fe-C-Cr alloy would be slower than in the binary Fe-C alloy. It would be even slower for the local equilibrium no-partition condition than for the para-equilibrium condition and is further retarded with increasing chromium content. The eutectoid carbon content for no-partition reactions lies close to the binary Fe-C eutectoid composition and increases slowly with increasing chromium content (figure (29)), whereas the equilibrium eutectoid carbon composition decreases as the chromium content increases.

For the pearlite reaction under para-equilibrium or local equilibrium no-partition conditions, the kinetics will be controlled by the diffusion of carbon and can be obtained from equation (III.22) for the volume diffusion model and equation (III.26) for the boundary diffusion model. However, the values for $C_o^{\gamma\alpha}$ and $C_o^{\gamma cm}$ in these equations will be modified by the chromium content of the alloy as discussed in the previous sections of this chapter.

In region C of figure (28) partitioning of chromium is thermodynamically required for the precipitation of α as well as cm, so the same can be said for the pearlite reaction, $\gamma\rightarrow\alpha$+cm. In region A, α and cm can both precipitate without partitioning and hence the pearlite reaction, $\gamma\rightarrow\alpha$+cm, can thermodynamically proceed without the partitioning of chromium. In the region [illegible] only one of the two phases (α or cm) requires the partitioning of the alloying element. In this case two possibilities exist. Since the kinetics of the no-partition reaction are much faster than the partitioning reaction, the phase which requires no-partitioning can precipitate first and grow until the matrix composition shifts into region A or C and then the pearlite reaction can start accordingly. The other possibility is that the capillarity effects during the pearlite reaction modify the phase diagram in such a way that the alloy falls in region A or C and the pearlite reaction again takes place accordingly. In either case a carbon component ray ($\frac{X_{Cr}}{X_{Fe}}$ = constant) passing through the no-partition eutectoid point would divide the pearlite reaction region into regions where partitioning is required and where no-partition is thermodynamically feasible. Since generally in practice no primary ferrite or cementite is observed in alloys in the B regions, the second possibility seems to be operative.

The pearlite reaction under alloying element diffusion control

In the temperature range where the partitioning of the alloying element takes place the pearlite reaction may be assumed to be controlled by diffusion of the alloying element. Since carbon diffuses much faster than the alloying element it can be inferred that the carbon activity in front of the pearlite growth front is uniform. At the same time the diffusion path of the alloying element must be through the pearlite-austenite interface (boundary diffusion control) since the volume diffusion coefficient for substitutional elements at these temperatures is vanishingly small.

Now, assuming local equilibrium at the interface and a steady state pearlite growth (i.e., the average composition in the pearlite is the same as in the original alloy), the interface compositions for a flat interface condition and consistent with the above description can be obtained by the construction shown in figure (30). In figure (30) point 0 is the alloy composition, points a and d the compositions in the ferrite and cementite phases, respectively, ab and cd are the tie-lines describing the ferrite-austenite and cementite-austenite interface compositions, respectively, and the line going through b and c is the carbon isoactivity line ahead of the pearlite-austenite interface. The carbon isoactivity line in general, may not go through point 0 (i.e., the original composition of the alloy). The difference is accommodated by the capillarity effect. The driving force for the boundary diffusion of the alloying element will then be proportional to ($C_X^{\gamma\alpha}$-$C_X^{\gamma cm}$) where $C_X^{\gamma\alpha}$ is the concentration of X in austenite at the α-γ interface (point b in figure (30)) and C_X^{cm} is the concentration of X in the austenite at the γ-cm interface (point c in figure (30)). The growth rate of pearlite under the boundary diffusion control of the alloying element can then be written, following Hillert$^{(11,69)}$ (Section III.1, Chapter III), as:

$$v = 12K\, D_{Cr}^{B}\, \delta\, \frac{S^2}{S^{\alpha}S^{\beta}}\, \frac{(C_X^{\gamma\alpha}-C_X^{\gamma cm})}{\bar{C}_X}\, \frac{1}{S^2}\, (1-\frac{S_o}{S}) \qquad (IV.14)$$

where K is the boundary segregation coefficient for X, δ is the boundary thickness, $\bar{C}_X$ is the average composition of X in pearlite and other terms are as defined previously in Chapter III. The term $\bar{C}_X$ exists in the denominator in equation (IV.14), and not a term of the form $(C_X^{cm}-C_X^{\alpha})$ as in the case of carbon boundary diffusion control of the pearlite reaction, because in the eutectoid reaction in Fe-C-X system the major component which determines the nature of the reaction (i.e., the eutectoid) is carbon whereas X only modifies the thermodynamics of this reaction. Equation (IV.14) is similar to the one used by Kirkaldy(6) and gives the correct binary limit as X goes to zero.

The concentration of the alloying element in ferrite and cementite (i.e., the partitioning of X) is obtained from points a and d in figure (30), respectively. However, these concentrations are modified by the capillarity effect.

CHAPTER V

THE PEARLITE REACTION IN THE Fe-C-Cr SYSTEM

V.1 INTRODUCTION

A knowledge of the kinetics of the pearlite reaction is of great importance for the understanding of the hardenability of steels. The role of alloying elements during the pearlite reaction has been the subject of numerous experimental as well as theoretical studies.

All the common alloying elements in steels, with the possible exception of cobalt, are known to retard the pearlite reaction. The theory of pearlite reaction for binary Fe-C alloys has been well established (Chapter III). However, the effect of the alloying elements on the pearlite reaction is theoretically less understood. The attempts by Hillert(82) and by Bolze(81) to develop a theory for the eutectoid reaction in ternary systems have not been very successful.

This part of the present work was undertaken to experimentally examine the growth process of pearlite in the Fe-C-Cr system, to investigate the partitioning of chromium between ferrite and cementite during the pearlite reaction and to relate it to the thermodynamics of the Fe-C-Cr system.

Unfortunately, our attempts to experimentally determine the partitioning of chromium did not succeed. In this chapter the growth rate and pearlite spacing measurements on a number of Fe-C-Cr alloys are discussed and the data on the partitioning of chromium during the pearlite reaction published recently by Razik et al.(19) is analysed in terms of the thermodynamics of the Fe-C-Cr system and the general discussion on the theory of pearlite reaction presented in previous chapters.

V.2 EXPERIMENTAL PROCEDURE

(a) Preparation of Material

Three Fe-C-Cr alloys with nominal chromium contents of 0.5, 1 and 2 percent were chosen to investigate the influence of chromium on the growth process of pearlite. The method for the preparation of the alloys was similar to the one described in Chapter II. The analysed alloy compositions are given in table (11).

(b) Isothermal Experiments

For the pearlite transformation experiments samples approximately 0.5 mm thick and 1 cm x 2 cm in area were austenitised at 950°C for half an hour in a salt bath and then transferred to a lead bath at the required transformation temperature. At each temperature six samples were treated for different times and then quenched into water. Despite normal precautions, surface decarburisation of some samples was detected. To solve this problem the samples were plated with copper by dipping the cleaned samples in a slightly acidic copper sulphate solution. This gave an adherent copper film on the surface and no further decarburisation occurred. For the times and the temperatures of heat treatment the diffusion of copper into the sample was calculated to be insignificant and hence would have no effect on the transformation kinetics. These partially transformed samples were metallographically analysed for growth rates and interlamellar pearlite spacings.

(c) Measurement of the Growth Rates

The simplest and the most common method for determining the growth rates of pearlite is from measurements of the largest unimpinged nodule diameter observed in a sample after a given reaction time. The growth rate is obtained by plotting the radius of such a nodule as a function of time, the slope giving the growth rate.

Another method of obtaining the average growth rate of pearlite is outlined by Cahn and Hagel.(94) The average growth rate, $\bar{v}$, is defined by:

$$\bar{v} = \frac{1}{A_f}\frac{dX}{dt} \qquad (V.1)$$

where A_f is the free pearlite surface area, X is the volume fraction transformed and t is time. $\frac{dX}{dt}$ is obtained from the relation:

$$\frac{dX}{dt} = \frac{(1-X)\ln(1/(1-X))}{t} \cdot m \qquad (V.2)$$

where m is the slope of a $\log[\ln(\frac{1}{1-X})]$ vs log(t) curve. The free pearlite surface area, A_f, is defined as the matrix/pearlite interface not yet impinged with other pearlite nodules and therefore assumed to be free to grow.

The third method for measuring the growth rate of pearlite has been developed by Woodhead after the ideas of Scheil and Lange-Weise.(95) It involves the determination of the size distribution of the pearlite nodules in each specimen using a Zeiss particle analyser. Recentely, Bramfitt and Marder(96) have measured the pearlite growth rates accurately using a hot-stage microscopic technique.

Brown and Ridley(97) used the first three methods to determine the pearlite growth rates in the same samples and found that all three methods yielded results in good agreement with each other.

In our investigation, we followed the first method for the most part. The samples were polished and etched and the measurement of the largest unimpinged nodule diameter (or radius) was carried out on an optical microscope mounted with a measuring eyepiece. Figure (31) shows typical micrographs for one isothermal experiment. The second method of Cahn and Hagel(94) was also used for the 2% Cr alloy. The volume fraction and the free pearlite surface area were measured using the automatic image analyser at the Steel Company of Canada Research Laboratories, Hamilton. The results of the growth rates by this method were in good agreement with those obtained by the first method. Only the first method was used for the other alloys. In some cases the pearlite nucleated at the free surface and grew inwards, particularly at lower temperatures. The growth rates in these samples were measured by determining the width of this surface pearlite as a function of time. Figure (32) shows typical micrographs of such samples. The results of these measurements were repeated and confirmed by the first method in some cases.

(d) Measurement of the Interlamellar Spacing

The most common and the most reliable and consistent approach employed in determining the interlamellar pearlite spacing is to measure the average smallest spacing in a specimen.(15,97) Other methods(98) to arrive at the "true" minimum spacing have been tried without much success. It is, therefore, generally agreed that the average minimum spacing is the most reliable and consistent. In this investigation the following procedure was adopted to obtain the average minimum interlamellar spacings.

Gold-shadowed carbon replicas of the polished and etched samples were prepared by the conventional method. Before mounting the replicas in the electron microscope, latex spheres of 0.481 μ diameter size were sprayed onto the replicas for reference. A number of electron-micrographs (20 to

25 for each sample) were taken of the areas where the spacing seemed to be minimum by visual examined. Then the average minimum spacing was obtained by careful measurements on the enlarged micrographs. The image of the latex spheres was used as a standard. Figure (33) shows typical electron micrographs.

(e) Partitioning Measurements

The measurement of the partitioning of the alloying element between cementite and ferrite during the pearlite reaction is rendered difficult for two main reasons: (1) The spacing between the cementite and the ferrite is submicron in dimension so the conventional microprobe technique cannot be used to resolve the concentration difference between these phases because the X-ray excitation volume in the conventional microprobe technique is of the order of a few microns. (2) Also, for the same reason of submicron interlamellar spacing, a substantial partitioning of the alloying element towards equilibrium takes place behind the growing pearlite-austenite interface during the isothermal treatment and hence carbide extraction and analysis would give results which cannot be easily related to the growth process.

Recently Razik et al.(17,19) studied the partitioning of manganese and chromium during the pearlite reaction in the analytic electron microscope, EMMA-4, using thin film specimens. This electron microscope is adapted with a probe forming mini-lens and X-ray detection equipment. A probe size of 0.05-.1 μ diameter was obtained which is also the effective diameter of the beam because of the thin specimen condition. The measurements for partitioning were carried out near the pearlite-austenite interface, thus avoiding errors due to post-diffusion.

We did not have this facility available at McMaster University. The Philips EM300 electron microscope attached with the EDAX system described in Chapter II was capable of a minimum probe size of 0.3-0.5 μ which is insufficient to resolve the concentration differences between cementite and ferrite. We decided, therefore, to try carbide extraction replicas instead of thin films. The carbon extraction replicas of partially transformed samples were prepared by the method described by Booker and Norbury.(99) The samples were polished and lightly etched with 2% nital and then dipped in a 10% nitric acid solution in ethanol for times varying from one half to two minutes. The optimum time was arrived at by trial and error. Immediately after this etch the specimen was thoroughly rinsed with alcohol and dried in hot air. The etched surface was then coated with a thick collodion film. After the film was dry it was stripped from the specimen and a thin layer of carbon was deposited on it under vacuum. The collodion film was then dissolved and a carbon extraction replica was obtained. By this method good carbon extraction replicas were obtained as shown in figure (34). In this way we sought to analyse the chromium content of cementite near the edge of a pearlite nodule using the Philips EM300 electron microscope attached with the EDAX system. Unfortunately, repeated efforts to obtain reliable and consistent data by this method did not succeed. The failure is due to either or both of the following reasons:

(i) There is always some X-ray signal produced from the internal structure of the microscope; particularly the sample holder. For example, Berenbaum and Cammarano(100) observed Ni and Cu and sometimes Cr and Zn characteristic X-rays in a similar set-up.

In the analogous experiments described in Chapter II to analyse equilibrium carbides the error due to Cr radiation originating from the internal structure of the electron microscope was found to be within the statistical scatter. This was confirmed by analysing cm particles in pure Fe-C alloy under similar conditions. This result was to be expected because of the relatively high counting rate obtained from the high chromium contents and the relatively large size of the carbide particles.

In the analyses of the pearlite extraction replicas the cementite particles were much thinner and lower in Cr content than for the equilibrium experiments and required a counting time of ten minutes or more to obtain a statistically significant number of counts. In this case the Cr radiation coming from the internal structure of the microscope posed a major problem. A pearlite extraction replica prepared from a partially transformed pure Fe-C alloy gave counts corresponding to chromium contents of anywhere from 0.5 to 5 chromium. No systematic correction for this error could be applied since the chromium counts for pure Fe-C pearlite varied from position to position. We might have taken the minimum value from a large number of measurements as being close to the actual value. However, even this index had a large variation from sample to sample and could not be relied upon.

(ii) The erroneous analysis could lie in the method of preparing the extraction replicas themselves. Kirchner and Stephenson,(101) and Habrovec (102) have reported that during the preparation of extraction replicas very small cm particles can spontaneously decompose or chemically react with the etchant. In checking this possibility we found that our results did not improve using cold bromine and other etchants.

Thus, as already noted, the partition of chromium during the pearlite reaction could not be determined with the techniques available to us. As an alternative, therefore, the measurements of the chromium partition obtained by Razik et al.(19) will be discussed in the light of the new thermodynamic and kinetic considerations described in Chapters III and IV.

V.3 RESULTS

(a) The Growth Rates

Table (12) compares the growth rates obtained by the maximum nodule diameter measurements and by the method of Cahn and Hagel$^{(94)}$ for the 2% Cr alloy. At higher temperatures the Cahn and Hagel method gave low results. This is because the automatic image analyser at the Steel Company of Canada used for the measurements, measured the whole of the pearlite-martensite (formerly austenite) interface area even though some of the interface was not an active growth front (i.e., grain boundary hemispherical nodules). This situation does not exist at lower temperatures. The results obtained by the two methods are generally in good agreement. Only maximum nodule diameter measurements were used to determine the growth rates for the other alloys.

Tables (12) to (14) summarise the growth rate data obtained for all three experimental alloys. The growth rates as a function of temperature are plotted in figure (35) for all of the alloys. Also included in figure (35) are the growth rate data for Fe-C and Fe-1.3 wt% Cr-0.8 wt % C alloys taken from other comparable studies. As is seen from figure (35) the maximum in the growth rate of pearlite shifts to a lower rate and a higher temperature as the chromium content of the steel is increased, thus demonstrating the retarding effect of chromium on the pearlite reaction.

(b) The Interlamellar Spacing

The interlamellar spacing as a function of temperature is given in tables (12) to (14) for all three experimental alloys. The reciprocal of the interlamellar spacing as a function of the transformation temperature is plotted in figure (36). The mean experimental curves for 0% Cr and 1.3% Cr alloys from other sources are also included in figure (36).

V.4 DISCUSSION

(a) The Growth Rates

(i) High Supersaturation: Puls and Kirkaldy(15) have calculated growth rates for the pearlite reaction in the Fe-C system assuming carbon volume diffusion control. Their calculated values are in reasonable agreement with the experimental values above 600°C. They obtained the following expression for the pearlite velocity, v, based on Hillert's(11,69) theory:

$$v = 1.27 \frac{D_C}{S} (C_o^{\gamma\alpha} - C_o^{\gamma cm}) \text{ cm/sec} \tag{V.3}$$

where D_C (cm^2/sec) is the carbon diffusion coefficient in austenite, S (cm) is the interlamellar spacing and where $C_o^{\gamma\alpha}$ and $C_o^{\gamma cm}$ (wt % C) are the carbon concentrations in austenite in equilibrium with ferrite and cementite, respectively. In the case of the Fe-C-Cr system without partitioning of chromium, i.e., either the para-equilibrium or the local equilibrium no-partition conditions, we are justified in assuming that equation (V.3) can still be used to calculate the pearlite growth rates. Figures (37) to (40) show the para-equilibrium and the local equilibrium no-partition phase diagrams for our three experimental alloys and the 1.3% Cr alloy used by Razik et al.,(19) calculated according to the procedure described in Chapter IV. $C_o^{\gamma\alpha}$ and $C_o^{\gamma cm}$ values thus calculated are used in equation (V.3) to calculate the pearlite growth rates. The diffusion coefficient of carbon in austenite, D_C, was obtained by extrapolating the data of Wells et al.(102) to the average carbon concentration at the interface which was calculated as

$$\left(\frac{S^\alpha}{S} C_o^{\gamma\alpha} + \frac{S^{cm}}{S} C_o^{\gamma cm}\right)$$

and the S values obtained from the experiments (figure (36)) were used.

The results of such calculations are shown in figures (41) to (45) along with the comparable calculations for the Fe-C (figure (41)) and the Fe-1.3% Cr alloy (figure (44)). Also shown in these diagrams are the experimental growth rates.

In the case of the Fe-C alloys the calculated growth rates are lower than the experimental values by a factor of about 2 (figure (41)). This is the minimum discrepancy between the experimental values and the volume diffusion model calculations that has been achieved to date. The partial involvement of boundary diffusion is thus not ruled out. Puls and Kirkaldy$^{(15)}$ have discussed this problem in more detail. Here we note only that there is a residual discrepancy between the experiments and the volume diffusion calculations to be kept in mind when making similar comparisons for the other alloys.

For the Fe-C-Cr alloys, figures (42) to (45), the experimental values for the grwoth rates at the lower temperatures are in general closer to the local equilibrium no-partition model than to the para-equilibrium model. The experimental values, as in the Fe-C case, are generally higher by a factor ranging from 1 to 2.5. The growth rates calculated from the para-equilibrium model are fortuitously closer to the experimental values in the case of the Fe-0.4% Cr alloy (figure (42)) because of the residual discrepancy, but are higher for all the other alloys by a factor ranging from 2.5 for the Fe-1% Cr alloy to about 15 for the Fe-2% Cr alloy. Thus it can be concluded that for all the alloys discussed, above the pearlite growth at low temperatures is most probably governed by the local equilibrium no-partition condition.

(ii) Low Supersaturations: At high temperatures, or low supersaturations, the pearlite reaction must be accompanied by the partitioning of chromium between cementite and ferrite. The chromium must therefore diffuse through the pearlite-austenite interface as the volume diffusion coefficient of chromium at these temperatures is vanishingly small. Assuming a uniform carbon activity in austenite in front on the pearlite-austenite interface, the driving force for chromium boundary diffusion-controlled growth can be calculated as discussed in Chapter IV, section IV.6 (see also figure (30)). Figure (46) shows the calculated values for the driving concentration difference $(C_{Cr}^{\gamma\alpha}-C_{Cr}^{\gamma cm})$ for the four alloys under discussion. The growth rate according to Hillert is given by equation (IV.14), i.e.,

$$v = 12K\, D_{Cr}^{B}\,\delta\, \frac{S^2}{S^\alpha S^\beta}\, \frac{(C_{Cr}^{\gamma\alpha}-C_{Cr}^{\gamma cm})}{\bar{C}_{Cr}}\, \frac{1}{S^2}\, (1-\frac{S_0}{S}) \qquad (V.4)$$

Taking $\frac{S^\beta}{S} = \frac{1}{8}$ and $\frac{S^\alpha}{S} = \frac{7}{8}$, and $S = 2S_0$, equation (V.4) becomes:

$$v \cong 54K\, D_{Cr}^{B}\,\delta\, [\frac{(C_{Cr}^{\gamma\alpha}-C_{Cr}^{\gamma cm})}{\bar{C}_{Cr}}]\, \frac{1}{S^2} \qquad (V.5)$$

Since in this equation K and D_{Cr}^{B} are experimentally unknown the functional validity of the equation must be checked as follows:

Rearranging equation (V.4) we get

$$K\,\delta\, D_{Cr}^{B} = \frac{v}{54[\frac{C_{Cr}^{\gamma\alpha}-C_{Cr}^{\gamma cm}}{\bar{C}_{Cr}}]\,\frac{1}{S^2}} \qquad (V.6)$$

The left hand side of equation (V.6) is independent of the alloy composition, depending only on the temperature. Furthermore, the temperature dependence of the left hand side should be the same as that of D_{Cr}^{B} since K and δ can be assumed as a first approximation to be independent of temperature. The values of the right hand side of equation (V.6) are calculated for all the alloys at temperatures above the local equilibrium no-partition transition temperatures. The experimental v and [illegible] values and the $(C_{Cr}^{\gamma\alpha}-C_{Cr}^{\gamma cm})$ values from figure (46) are used. The calculations are summarised in table (15) and plotted as $\ln(K\delta D_{Cr}^{\delta})$ vs 1/T in figure (47).

The values of $K\delta D_{Cr}^{B}$ obtained from such calculations, as seen from table (15) and figure (47), are approximately constant for a given temperature (within a factor of 2) as would be expected if equation (V.4) were valid. From the slope and intercept of the straight line in figure (47), the following equation is obtained for $(K\delta D_{Cr}^{B})$:

$$K\delta D_{Cr}^{B} = 7.6\times10^{-8}\ \exp\left(-\frac{40,350}{RT}\right)\ \mathrm{cm}^3/\mathrm{sec.} \qquad (V.7)$$

This gives an activation energy for D_{Cr}^{B} of 40.350 cal/mole. No measurements of chromium diffusion exist in appropriate phase boundaries, and furthermore, there are very few studies on the grain boundary diffusion of alloying elements in iron. However, there are several studies on the grain boundary diffusion of iron in austenite and ferrite. All these studies, including one on chromium grain boundary diffusion in ferrite, have been summarised by Fridberg et al.$^{(104)}$ They found that the grain boundary diffusion coefficient of iron in austenite and in ferrite, as well as the boundary diffusion coefficient of some alloying elements in austenite and/or ferrite, can be described by a single equation:

$$K\delta D_B = 5.4\times10^{-8} \exp(-\frac{37,000}{RT}) \text{ cm}^3/\text{sec.} \qquad (V.8)$$

In view of the limited temperature range covered by our analysis (60°C), the value of 40,350 cal/mole for the activation energy for the phase boundary diffusion of chromium derived from the pearlite growth data on the basis of equation (V.4) is in reasonable agreement with the above experimental value of 37,000 cal/mole(104) (equation (V.8)).

Comparing equations (V.7) and (V.8), the values of the $K\delta D_B^{Cr}$ obtained from these equations in the temperature range of our analyses are within a factor of 4 which is about the same as the scatter in the experimental data from which equation (V.8) is obtained. This, together with the reasonable value for the activation energy for chromium boundary diffusion, testifies to the broad validity of equation (V.4) for pearlite growth in Fe-C-X systems at low supersaturations where the alloying element must partition.

(b) Interlamellar Spacing

In figure (36), the reciprocal interlamellar spacing is plotted as a function of temperature for 0, 0.4, 0.9, 1.3 and 1.8 percent chromium steels. The points lie close to straight lines and are very nearly parallel. Cahn and Hagel(94) have suggested that the plot of reciprocal spacing vs temperature should show a distinct change in slope in the vicinity of the temperature where the partitioning of the alloying element ceases. Interestingly, no such change was observed in the present study, nor has it been observed in previous studies on alloy pearlites.(17,19)

The intercept of the reciprocal spacing vs temperature line with the temperature axis should be the eutectoid temperature. At this temperature the spacing approaches infinity as there is no free energy available for forming an interface between α and cm. Eutectoid temperatures obtained from figure (36) have been used as an experimental verification for the phase diagram calculations in Chapter II and the agreement is very good (figure (11)).

Now we will consider the 1/S vs T relationship in more detail. There are two interesting features of this relationship which need to be explained. Firstly, the 1/S vs T relationship for the chromium alloys are approximately straight lines and show no change of slope near the partition - no-partition transition. Secondly, the lines for the chromium alloys are nearly parallel to the 1/S vs T straight line for the binary Fe-C alloy and do not cross to lower 1/S values at high supersaturation (i.e., low temperatures) as might be expected from the fact that the no-partition eutectoid temperature is lower than the eutectoid temperature of the binary Fe-C system.

The critical interlamellar spacing, S_0, is related to the free energy of transformation for the pearlite reaction, ΔF_0, by the relation

$$S_0 = -\frac{2\sigma^{\alpha cm}V}{\Delta F_0} \qquad (V.9)$$

where $\sigma^{\alpha cm}$ is the interfacial free energy between α and cm and V is the molar volume. Figure (48) shows ΔF_0 as a function of temperature for the binary Fe-C and the 1.3% Cr alloys for different mechanisms of transformation, calculated from the thermodynamic data of Chapter II. Figure (49) shows the relative 1/S vs T plots expected by assuming $S = 2S_0$ in the low supersaturation range (chromium boundary diffusion control) and $S = 3S_0$

for high supersaturations and for binary Fe-C (i.e., carbon volume diffusion control) and for the same $\sigma^{\alpha cm}$ value for the two alloys (---, lines in figure (49)).

To explain the straight line relationship we must assume that transition from the low supersaturation chromium partitioning range to the high supersaturation no-partition range is not sharp as predicted from the thermodynamics but rather is gradual. Furthermore, at low supersaturations there must be a mixing of the local equilibrium and paraequilibrium models to yield lower values of 1/S (i.e., a smooth transition corresponding to a variable deviation from complete local equilibrium at the interface) and at high supersaturations there must be appreciable diffusion of chromium along the pearlite-austenite interface to give higher values of 1/S. By such a transition between processes a linear 1/S vs T relationship as shown in figure (49) (-·-·-, line) might be obtained.

The 1/S vs T line obtained from the above considerations would cross the 1/S vs T line for the binary Fe-C at some temperature in the vicinity of the local equilibrium partition - no-partition transition (see figure (49)). By contrast, the experimental 1/S vs T relationships for chromium steels are approximately parallel to that for Fe-C (see figure (36)). The relative slopes of these lines can be explained if we conjecture that the interfacial free energy, $\sigma^{\alpha cm}$, changes with the addition of chromium. The back calculation required to predict the correct relative slopes of the 1/S vs T relationships from the calculated ΔF_0 and the experimental interlamellar spacings give $\sigma^{\alpha cm}$ values ∿40% lower for the 1.8% Cr alloy, ∿30% lower for the 1.3% Cr alloy, ∿20% lower for the 0.9% Cr alloy and ∿8% lower for the 0.4% Cr alloy than the $\sigma^{\alpha cm}$ value for the binary Fe-C ($\sim$650 ergs/cm^2). This implies an approximately linear decrease in $\sigma^{\alpha cm}$ with the chromium content of steel. It is certainly conceivable that chromium segregation to the α-cm interface could decrease its energy by the above factors.

(c) Partitioning of Chromium

The partitioning of chromium during the pearlite reaction could not be experimentally determined as explained earlier in section V.2(e). The results of chromium partitioning obtained by Razik et al.(19) for 1.3% Cr alloy will accordingly be discussed here.

Razik et al. have defined the chromium partitioning during the pearlite growth as:

$$K_{\alpha}^{cm}\ (Cr) = \frac{[C_{Cr}/C_{Fe}]^{cm}}{[C_{Cr}/C_{Fe}]^{\alpha}} \qquad (V.10)$$

The chromium partitioning is calculated as described in Chapter IV (see also figure (30)) and converted into K_{α}^{cm} (Cr) as defined in equation (V.10). The calculated values and the experimental results of Razik et al.(19) for 1.3% chromium alloy are plotted together in figure (50). The calculated values are seen to be high by a factor of 5 or more. Razik et al. obtained zero partitioning of chromium below about 690°C while the calculated no-partition temperature according to the local equilibrium model is 685°C. In this latter respect, the agreement between the theory and experiment is excellent.

The discrepancy between the calculated and experimental K_{α}^{cm} (Cr) values may be due to one or both of the following factors: (i) an error in experimentation and (ii) incomplete local equilibrium at the interface, i.e., partial involvement of para-equilibrium.

With the EMMA-4 analytical electron microscope used by Razik et al. for partitioning measurements the minimum probe size that can be obtained is 500 Å to 1000 Å. The pearlite spacing for the 1.3% Cr alloy was approximately 1000 Å at 700°C and 760 Å at 680°C, which leads to a cementite plate thickness of about 150 Å and 100 Å, respectively. To have a probe focussed entirely on the cm plate it must be at a very low angle to the surface of the thin foil (~10° or less). This may not have always been the case, and even if it were, a small volume of α is likely to come into the path of the electron beam as indicated in figure (51). This would lead to generally lower concentrations of chromium in cementite being measured than the actual values and hence to low experimental K_{α}^{cm} (Cr) values. This could also partially explain the fact that as the temperature goes down the discrepancy between the experimental and calculated values is increased. However, this factor alone is insufficient to explain the large difference between the experimental and calculated values.

More significantly, a correction for the lack of complete local equilibrium at the pearlite-austenite interface would lower our predicted K_{α}^{cm} (Cr) values. This would imply a state at the interface which is intermediate between local equilibrium and para-equilibrium. In the previous section, while discussing the straight line relationship between the 1/S. vs T plot, we were forced to conjecture that at low supersaturations the pearlite reaction takes place by a mixing or overlap of the local equilibrium and para-equilibrium conditions to justify an average straight line relationship. The lower experimental K_{α}^{cm} (Cr) values can be taken as an indirect justification for that conjecture.

Here a further general comment upon the controlling principle for pearlite reaction in ternary steels is required. While we can thermodynamically define the operative regions for different mechanisms, the smooth variation of growth rate as a function of temperature, and particularly the unexpected straight line relationship between 1/S and T over a range which involves several different thermodynamically-defined mechanism regions, implies the existence of a yet unspecified thermokinetic principle which determines the operating state. This could be a mini-max in the rate of entropy production as suggested by Kirkaldy. However, it will not be possible to check such a proposition until the rigorous approach to the ternary problem introduced by Bolze(81) and by Hillert(82) is rendered tractable.

In conclusion, our prediction of the amount of partitioning during the pearlite reaction in Cr steels is not very good. At the same time the observed partition - no-partition transition temperature is close to the predicted local equilibrium no-partition temperature, a condition implied by the measurements of growth kinetics.

(d) The Effect on Chromium on the Hardenability

The addition of chromium to steels increases the hardenability. This is directly associated with the ability of chromium to retard the austenite decomposition reactions. The mechanism of retardation of the kinetics of these reactions can in general be divided into two parts: At low supersaturations the kinetics is controlled by the diffusion of chromium and is accompanied by the partitioning of that element. At high supersaturations no partitioning of chromium takes place so that the kinetics is controlled by the diffusion of carbon alone and the retardation effect is through the thermodynamic decrease of the effective undercooling.

In the case of the $\gamma\rightarrow\alpha$ transformation in the Fe-C-Cr system the retardation effect cannot be explained solely on the basis of the above mechanisms so that a boundary 'drag effect'(69,88) and other mechanisms have been suggested.(9) In contrast, for the $\gamma\rightarrow\alpha+cm$ (pearlite) reaction, the above-mentioned mechanisms explain the complete retardation effect reasonably well. At high supersaturations the local equilibrium no-partition mechanism appears to be operative while at low supersaturations the pearlite reaction is controlled by the boundary diffusion of chromium and is explained within local equilibrium considerations. As well, the partition - no-partition transition is properly predicted from local equilibrium no-partition calculations.

(e) The Relative Effects of Cr, Mn and Ni on the Pearlite Reaction

It is informative here to qualitatively consider the relative retardation effects of Cr, Mn and Ni on the pearlite reaction in terms of the mechanisms discussed above for Cr steels. Figure (52) shows the empirical pearlite growth rates and figure (53) the empirical inverse interlamellar spacing vs temperature plots for Fe-C-X (X = Cr, Mn, Ni) steels containing approximately 2% of alloying element taken from different studies. As is seen from figure (52), for the same amount of alloying element addition to steel, Cr has the maximum retardation effect on the pearlite reaction followed closely by Mn, while Ni has the least effect of the three elements under consideration.

At low supersaturations, the partitioning of the alloying element is thermodynamically required in all cases. For chromium the equilibrium eutectoid temperature is increased with the addition of that alloying element while the local equilibrium no-partition eutectoid temperature is decreased. This gives a relatively large temperature range where the partitioning of chromium takes place. For a 2% Cr alloy this range is ~100°C. In this range the pearlite growth must be controlled by chromium boundary diffusion. In the case of Mn, the low supersaturation partitioning range is smaller than for Cr and the equilibrium, as well as the local equilibrium no-partition eutectoid temperature, decrease with the addition of Mn. For the 2% Mn alloy the eutectoid temperature is approximately 690°C and partitioning occurs down to about 650°C, a partitioning range of about 40°C.(17) The maximum in the growth rate in this case is in the no-partition region. In the case of Ni steels, steady state pearlite growth in the partitioning region is never feasible according to the growth model discussed in Chapter IV (see also figure (30)), because Ni segregates into the austenite with respect to both the ferrite and cementite phases.(106) Hence, the steady state pearlite reaction in this case can take place only in the no-partition range. This is substantiated by the fact that in this case the growth rate curve (figure (50)) is not asymptotic to the equilibrium eutectoid temperature but to a temperature about 30°C lower. According to the available information the equilibrium eutectoid temperature for a 2% Ni alloy is about 707°C(106,107) and the pearlite growth rate curve is asymptotic to 678°C. This is also borne out by the 1/S vs T plots. While in the case of 2% Cr and 2% Mn alloys the 1/S vs T straight lines intercept the temperature axis at approximately equilibrium eutectoid temperatures, i.e., 761°C and 690°C, respectively, the corresponding intercept for the 2% Ni alloy is 678°C, approximately 30°C lower than the eutectoid temperature.

At high supersaturations, the pearlite reaction in all cases may be assumed to be controlled by the local equilibrium no-partition mechanism. The local equilibrium no-partition phase boundaries are strongly affected by the activity of carbon in austenite and the distribution coefficient between the austenite and the ferrite and cementite (see figure (23)). The more negative the effect of the alloying element on the carbon activity in austenite, the greater will be the decrease in the driving force for the no-partition reaction. Similarly, the farther away from unity is the distribution coefficient for the alloying element between the austenite and the ferrite and cementite, the greater will be the decrease in the driving force for the no-partition reaction. Of course, the main factor is the direct effect of the alloying elements on the equilibrium boundaries (see figure (23)). At the same time, at high supersaturations and relatively low alloying element additions the effect of the alloying element on the carbon activity will significantly alter the driving force as indicated in figure (54). The quantitative measure of this effect, the Wagner interaction parameter ε_C^X (X is the alloying element), is ∿-12 for Cr, ∿-5 for Mn and ∿+5 for Ni at around 800°C. The relative pearlite growth rates at high supersaturations appear to reflect this influence (figure (52)) for the growth rates are highest for the Ni alloy, lower for the Mn alloy and still lower for the Cr alloy.

A rigorous confirmation of this proposition can only be arrived at through a detailed knowledge of the thermodynamics and phase equilibria for the Fe-C-Ni and Fe-C-Mn systems.

This general understanding of the pearlite reaction in Fe-C-Cr and in the ternary Fe-C-X systems will serve as a starting point for the development of more rigorous theoretical models for the pearlite growth in ternary and higher order systems and ultimately to a more accurate and general treatment for predicting the hardenability of multi-component steels.

CHAPTER VI

CONCLUSIONS

1. The stable and metastable phase equilibria between the α, γ and cm phases in the Fe-C-Cr system have been calculated. The necessary thermodynamic data has been extracted from the limiting binary phase diagrams and other thermodynamic and phase equilibrium information published for the binary Fe-C and Fe-Cr, and the ternary Fe-C-Cr systems.

2. Tie-lines in the $\alpha+\gamma$ region at 770°C and 750°C, in the γ+cm region at 770°C and 750°C, in the α+cm region at 700°C and the three phase equilibrium ($\alpha+\gamma$+cm) at 750°C have been experimentally determined and all are in good agreement with the calculated phase equilibria.

3. The predicted variation of ~~the~~ eutectoid temperature with the chromium content in steel is in good agreement with the experimental values based on the extrapolation of the pearlite interlamellar spacing as a function of temperature to infinite spacing, i.e., the intercept of 1/S vs T plot with the temperature axis.

4. The partition and no-partition regions based on Hillert's para-equilibrium and Kirkaldy's and Hillert's local equilibrium no-partition arguments have been calculated for the $\gamma\rightarrow\alpha$ and $\gamma\rightarrow$cm transformations in Fe-C-Cr. The question of partitioning during the pearlite reaction in Fe-C-Cr has been discussed in terms of these regions.

5

5. The pearlite growth rates and interlamellar spacings have been determined for three Fe-C-Cr alloys containing 0.5, 1 and 2% chromium. These form a consistent set with those reported by Razik et al. for a 1.3% chromium steel.

6. The pearlite growth velocity is satisfactorily explained in terms of chromium boundary diffusion control at low supersaturations and in terms of the local equilibrium no-partition condition at high supersaturations.

7. The straight line relationships between the inverse interlamellar spacing and temperature and their relative slopes for the ternary Fe-C-Cr alloys are qualitatively explained.

8. The agreement between the amount of chromium partitioning during the pearlite reaction of the 1.3% chromium alloy experimentally determined by Razik et al. and our calculations based on local equilibrium flat interface considerations is not good. However, the partition - no-partition transition is properly predicted from the local equilibrium no-partition calculations.

9. The relative retardation effects of chromium, manganese and nickel on the pearlite reaction are qualitatively explained in terms of the mechanisms established for the chromium steels.

REFERENCES

1. E.C. Bain and H.W. Paxton: Alloying Elements in Steels, ASM, Metals Park, Ohio, 1961.
2. M.A. Grossman: Trans. AIME, 1942, vol. 150, p. 227.
3. E. Yost: Härterei-Technische Mitteilung, 1968, vol. 23, p. 85.
4. G.T. Brown and B.A. James: Met. Trans., 1973, vol. 4, p. 2245.
5. R.A. Grange: Met. Trans., 1973, vol. 4, p. 2231.
6. J.S. Kirkaldy: Met. Trans., 1973, vol. 4, p. 2327.
7. K.C. Russel: in Phase Transformations, ASM, Metals Park, Ohio, 1968.
8. M. Hillert: in Decomposition of Austenite by Diffusional Processes, V.F. Zackey and H.I. Aaronson, Eds., Interscience Publishers, New York, 1962.
9. R.C. Sharma and G.R. Purdy: Met. Trans., 1974, vol. 5, p. 939.
10. C. Zener: Trans. AIME, 1946, vol. 167, p. 550.
11. M. Hillert: Jernkont. Ann., 1957, vol. 141, p. 757.
12. D. Turnbull: Acta Met., 1955, vol. 3, p. 55.
13. J.W. Cahn: Acta Met., 1959, vol. 7, p. 18.
14. G. Bolz, M.P. Puls and J.S. Kirkaldy: Acta Met., 1972, vol. 20, p. 73.
15. M.P. Puls and J.S. Kirkaldy: Met. Trans., 1972, vol. 3, p. 2777.
16. M.L. Picklesimer et al.: Trans. AIME, 1960, vol. 218, p. 473.
17. N.A. Razik, G.W. Lorimer and N. Ridley: Acta Met., 1974, vol. 22, p. 1249.
18. F.E. Bowman: Trans. ASM, 1945, vol. 35, p. 112.
19. N.A. Razik, G.W. Lorimer and N. Ridley: Met. Trans. A, 1976, vol. 6A,

p. 209.

20. H. Harvig: Jernkont. Ann., 1971, vol. 155, p. 157.

21. F. Müller and O. Kubaschewski: High Temp.-High Pressure, 1969, vol. 1, p. 543.

22. G. Kirchner, T. Nishizawa and B. Uhrenius: Met. Trans., 1973, vol. 4, p. 167.

23. J. Chipman: Met. Trans., 1974, vol. 5, p. 521.

24. T. Nishizawa: Thermodynamic Study of Fe-C-Mn, Fe-C-Cr and Fe-C-Mo, Report No. 4602, Swedish Council for Applied Research, Stockholm, 1967.

25. K. Bungardt, E. Kunze and E. Horne: Arch. Eisenhüttenw., 1958, vol. 29, p. 196.

26. K. Bungardt, H. Preisendanz and G. Lehnert: Arch. Eisenhüttenw., 1964, vol. 35, p. 999.

27. R.S. Jackson: J. Iron and Steel Inst., 1970, vol. 208, p. 163.

28. R. Benz, J.E. Elliott and J. Chipman: Met. Trans., 1974, vol. 5, p. 2235.

29. W. Jellinghous and H. Keller: Arch. Eisenhüttenw., 1972, vol. 43, p. 319.

30. K. Kuo: J. Iron and Steel Inst., 1953, vol. 173, p. 363.

31. M. Hillert and L.I. Staffansson: Acta Chem. Scand., 1970, Vol. 24, p. 3618.

32. J. Chipman and E.F. Brush: Trans. AIME, 1968, vol. 242, p. 35.

33. B. Uhrenius: Scand. J. Metallurgy, 1973, vol. 2, p. 177.

34. M. Hillert: in Phase Transformations, ASM, Metals Park, Ohio, 1968.

35. R.P. Smith: J. Am. Chem. Soc., 1946, vol. 68, p. 1163.

36. S. Ban-ya, J.F. Elliott and J. Chipman: Trans. TMS-AIME, 1969, vol. 245, p. 1199.

37. S. Ban-ya, J.F. Elliott and J. Chipman: Met. Trans., 1970, vol. 1,

p. 1313.

38. J.B. Gilmour: Ph.D. Thesis, McMaster University, Hamilton, Ontario, September, 1970.

39. Metals Handbook, vol. 8, Eighth ed., ASM, Metals Park, Ohio, 1973.

40. R.L. Orr and J. Chipman: Trans. AIME, 1967, vol. 239, p. 630.

41. L. Kaufman, E.V. Clougherty and R.J. Weiss: Acta Met., 1963, vol. 11, p. 323.

42. C. Zener: Trans. AIME, 1946, vol. 167, p. 513.

43. L.S. Darken and R.P. Smith: Ind. Eng. Chem., 1951, vol. 43, p. 1815.

44. H. Johansson: Arch. Eisenhüttenw., 1937, vol. 11, p. 241.

45. J.C. Fisher: Trans. AIME, 1949, vol. 185, p. 688.

46. R.P. Smith: Trans. AIME, 1959, vol. 215, p. 954.

47. G. Kirchner and B. Uhrenius: Met. Trans. A, 1975, vol. 6A, p. 224.

48. J. Chipman: Met. Trans. A, 1975, vol. 6A, p. 226.

49. L. Kaufman: in Phase Stability in Metals and Alloys, P.S. Rudman, L. Stringer and R. Jaffe, eds., McGraw-Hill, New York, 1967.

50. T. Wada, H. Wada, J.F. Elliott and J. Chipman: Met. Trans., 1972, vol. 3, p. 2865.

51. J.C. Greenbank: J. Iron and Steel Inst., 1971, vol. 209, p. 986.

52. R.J. Brigham and J.S. Kirkaldy: Trans. TMS-AIME, 1963, vol. 227, p. 538.

53. H. Flender and H. Wever: Arch. Eisenhüttenw., 1960, vol. 31, p. 227.

54. R. Woodyatt and G. Krauss: Met. Trans. A, 1976, vol. 7A, p. 983.

55. J.B. Gilmour, G.R. Purdy and J.S. Kirkaldy: Met. Trans., 1972, vol. 3, p. 1455.

56. G.V. Kurdjumov: Proceedings of the International Conference on the Peaceful Uses of Atomic Energy, p. 15, 1955.

57. M.A. Krishtal: Diffusion Processes in Iron Alloys, Metallurgizdat, Moskva, 1963.

58. H.I. Aaronson and H.A. Domian: Trans. AIME, 1966, vol. 236, p. 781.

59. R.E. Reed-Hill: Physical Metallurgy Principles, Van Nostrand, New Jersey, 1964.

60. G.W. Lorimer et al.: Proceedings Fifth International Materials Symposium, G. Thomas, ed., p. 222, California University Press, Berkeley, 1971.

61. G. Cliff and G.W. Lorimer: J. of Microscopy, 1975, vol. 103, p. 203.

62. G.W. Lorimer, N.A. Razik and G. Cliff: J. of Microscopy, 1973, vol. 99, p. 153.

63. T.A. Hall: in Physical Techniques in Biological Research, 2nd ed., vol. 1A, p. 157, G. Oster, ed., Academic Press, New York, 1971.

64. E. Smith and J. Nutting: Brit. J. of Appl. Physics, 1956, vol. 7, p. 214.

65. EDIT/7EM Operating Manual, EDAX Laboratories, North Carolina, 1973.

66. R.W. Gurry, J. Christakos and C.D. Stricker: Trans. ASM, 1958, vol. 50, p. 105.

67. W.H. Brandt: J. Appl. Phys., 1945, vol. 16, p. 139.

68. E. Scheil: Z. Metallk., 1946, vol. 37, p. 123.

69. M. Hillert: in The Mechanism of Phase Transformations in Crystalline Solids, Institute of Metals, London, Monograph No. 33, 1968, pp. 231-247.

70. J.M. Shapiro and J.S. Kirkaldy: Acta Met., 1968, vol. 16, p. 579.

71. K.A. Jackson and B. Chalmers: in Principles of Solidification, by B. Chalmers, p. 201, John Wiley and Sons, New York, 1964.

72. J.S. Kirkaldy: Scripta Met., 1968, vol. 2, p. 565.

73. S. O'Hara and A. Hellawell: Scripta Met., 1968, vol. 2, p. 107.

74. F.C. Frank and K.E. Puttick: Acta Met., 1956, vol. 4, p. 206.

75. B. Sundquist: Acta Met., 1968, vol. 16, p. 1413.

76. J.S. Kirkaldy: Can. J. Phys., 1964, vol. 42, p. 1447.

77. J.S. Kirkaldy: in Energetics in Metallurgical Processes IV, W.M. Mueller, ed., p. 197, Gordon and Breach Science Publishers, 1968.

78. L. Onsager: Phys. Rev., 1931, vol. 37, p. 405.

79. D. Brown and N. Ridley: J. Iron and Steel Inst., 1969, vol. 207, p. 1232.

80. G.F. Bolling and R.H. Richman: Met. Trans., 1970, vol. 1, p. 2095.

81. G. Bolze: Ph.D. Thesis, McMaster University, Hamilton, Ontario, May, 1970.

82. M. Hillert: Acta Met., 1971, vol. 19, p. 769.

83. F.E. Bowman: Trans. ASM, 1946, vol. 36, p. 61.

84. G.R. Purdy, D.H. Weichert and J.S. Kirkaldy: Trans. AIME, 1964, vol. 230, p. 1025.

85. J.B. Gilmour, G.R. Purdy and J.S. Kirkaldy: Met. Trans., 1972, vol. 3, p. 3123.

86. R.C. Sharma and J.S. Kirkaldy: Can. Met. Quart., 1973, vol. 12(4), p. 391.

87. A. Hultgren: Jernkont. Ann., 1951, vol. 135, p. 403.

88. K.R. Kinsman and H.I. Aaronson: in Transformation and Hardenability in Steels, Climax Molybdenum, Ann Arbor, 1967.

89. M. Hillert: Jernkont. Ann., 1952, vol. 136, p. 25.

90. E. Rudberg: Jernkont. Ann., 1952, vol. 136, p. 91.

91. J.S. Kirkaldy: Can. J. Phys., 1958, vol. 36, p. 907.

92. D.E. Coates: Met. Trans., 1972, vol. 3, p. 1203.

93. D.E. Coates: Met. Trans., 1973, vol. 4, p. 2313.

94. J.W. Cahn and W.C. Hagel: in Decomposition of Austenite by Diffusional Processes, W.F. Zackey and H.I. Aaronson, eds., Interscience Publishers, New York, 1962.

95. E. Scheil and A. Lange-Weise: Arch. Eisenhüttenw., 1937, vol. 11, p. 93.

96. B.L. Bramfitt and A.R. Marder: Met. Trans., 1973, vol. 4, p. 2291.

97. D. Brown and N. Ridley: J. Iron and Steel Inst., 1966, vol. 204, p. 811.

98. M.K. Asundi and D.R.F. West: J. Inst. Metals, 1966, vol. 94, p. 19.

99. G.R. Booker and J. Norbury: Brit. J. Appl. Phys., 1959, vol. 10, p. 543.

100. L. Berenbaum and A. Cammarano: in Proceedings Ninth Annual Conference, Microbeam Analysis Society, July 22-26, 1974, Carlton University, Ottawa.

101. G.H. Karchner and E.T. Stephenson: Trans. ASM, 1967, vol. 60, p. 716.

102. F. Habrovec: Practical Metallography, 1968, vol. 5(1), p. 18.

103. C. Wells, W. Batz and R.F. Mehl: Trans. AIME, 1950, vol. 188, p. 553.

104. J. Fridberg, L.E. Törndahl and M. Hillert: Jernkont. Ann., 1969, vol. 153, p. 263.

105. The Electron Probe Microanalyzer, McMaster University, Hamilton, Ontario.

106. Ternära fasdiagram järn-kol-legeringsämne för kisel, mangan, krom, nickel, molybden och volfram, Reg. nr FF1775, SANDVIK Stalforskningen, Sweden, 1973.

107. J.S. Kirkaldy: private communication, McMaster University, Hamilton, Ontario.

TABLE 1

Standard free energy change for the transformation

Fe (fcc) to Fe (bcc)

T °K	$\Delta^0 G_{Fe}^{\gamma\to\alpha}$	T °K	$\Delta^0 G_{Fe}^{\gamma\to\alpha}$	T °K	$\Delta^0 G_{Fe}^{\gamma\to\alpha}$
850	-259.1	980	-99.3	1110	-18.37
860	-244.7	990	-89.8	1120	-14.92
870	-230.8	1000	-80.80	1130	-11.84
880	-217.3	1010	-72.18	1140	- 9.10
890	-204.1	1020	-64.16	1150	- 6.66
900	-191.1	1030	-56.75	1160	- 4.48
910	-178.3	1040	-50.15	1170	- 2.52
920	-166.0	1050	-44.31	1180	- 0.74
930	-154.1	1060	-39.11	1184.5	0
940	-142.4	1070	-34.21	1190	+ 0.89
950	-131.0	1080	-29.92	1200	+ 2.40
960	-119.9	1090	-26.07	1210	+ 3.82
970	-109.3	1100	-22.22	1220	+ 5.15

TABLE 2

Values of the parameter L^{Y}_{CCr} as a function of temperature

T °K	L^{Y}_{CCr} cal/mole	Ref.
1123	-3.303×10^{4}	50
1173	-2.921×10^{4}	51
1273	-2.366×10^{4}	50
1273	-2.574×10^{4}	24
1323	-2.291×10^{4}	51
1393	-2.220×10^{4}	51

TABLE 3

Evaluation of the thermodynamic parameters for ternary cementite from data of Nishizawa(24) at 1000°C

Y_C^γ	Y_{Cr}^γ	Y_{Cr}^{cm}	$(\Delta^oG^\gamma_{CrC_{1/3}}-\Delta^oG^\gamma_{FeC_{1/3}}) + A_{cm}(1-2Y^{cm}_{Cr})$	$1-2Y^{cm}_{Cr}$
.0710	.006	.034	-6,842	.932
.0696	.0087	.048	-6,776	.904
.0652	.0176	.100	-6,840	.800
.0647	.0195	.112	-6,877	.766
.0600	.0312	.176	-6,860	.648
.0589	.0340	.194	-6,903	.612
.0583	.0348	.200	-6,922	.600

TABLE 4

Evaluation of $(\Delta^{o}G^{\gamma}_{CrC_{1/3}}-\Delta^{o}G^{\gamma}_{FeC_{1/3}})$ from the data on γ-cm equilibrium

T °K	Y^{γ}_{Cr}	Y^{γ}_{c}	Y^{cm}_{Cr}	$(\Delta^{o}G^{\gamma}_{CrC_{1/3}}-\Delta^{o}G^{\gamma}_{FeC_{1/3}})$	Ref.
1123	.0179	.0389	.1766	-7,058	39
1423	.0380	.0635	.1766	-7,046	39
1273	.0300	.056	.212	-7,450	26
1273	.0263	.0458	.13	-5,991	28
1373	.0265	.0565	.118	-6,313	28
1143	.0218	.0247	.19	-6,545	54

TABLE 5

Evaluation of $(\Delta^{o}G^{\gamma}_{CrC_{1/3}} - \Delta^{o}G^{\gamma}_{FeC_{1/3}})$ from the data on

α-cm equilibrium

T °K	Y^{α}_{Cr}	Y^{cm}_{Cr}	$(\Delta^{o}G^{\alpha}_{CrC_{1/3}} - \Delta^{o}G^{\alpha}_{FeC_{1/3}})$	$(\Delta^{o}G^{\gamma}_{CrC_{1/3}} - \Delta^{o}G^{\gamma}_{FeC_{1/3}})$	Ref.
973	.0035	.1355	-4,277	-6,816	29
973	.0069	.2415	-4,298	-6,837	29
973	.0063	.2055	-4,092	-6,630	30
973	.0044	.1244	-3,673	-6,211	30
973	.0063	.1842	-3,841	-6,380	30

TABLE 6

Summary of the thermodynamic parameters for the Fe-C-Cr system

Parameter	Value
L^{γ}_{Cv}	-8830 cal/mole
L^{γ}_{FeCr}	-3133-7.606T+0.6568TlnT cal/mole
L^{α}_{Cv}	0
L^{α}_{FeCr}	6000-2.8T cal/mole
$L^{\gamma}_{CrC}=L^{\alpha}_{CrC}=L_{CrC}$	-76,745+40.16T cal/mole
A_{cm}	286 cal/mole (M)
${}^{o}G^{\alpha}_{Fe}-{}^{o}G^{\gamma}_{Fe}$	Table (1)
${}^{o}G^{\alpha}_{Cr}-{}^{o}G^{\gamma}_{Cr}$	-2500-0.15T cal/mole
${}^{o}G^{\alpha}_{C}-{}^{o}G^{\gamma}_{C}$	16,923-6.933T cal/mole
$\Delta^{o}G^{\gamma}_{FeC_{1/3}}$	-521-13.2T+1.69TlnT cal/mole (Fe)
$\Delta^{o}G^{\gamma}_{CrC_{1/3}}$	-7596-13.2T+1.69TlnT cal/mole (Cr)
$\Delta^{o}G^{\alpha}_{FeC_{1/3}}$	$\Delta^{o}G^{\gamma}_{FeC_{1/3}}-({}^{o}G^{\alpha}_{Fe}-{}^{o}G^{\gamma}_{Fe})-\frac{1}{3}({}^{o}G^{\alpha}_{C}-{}^{o}G^{\gamma}_{C})$ cal/mole (Fe)
$\Delta^{o}G^{\alpha}_{CrC_{1/3}}$	$\Delta^{o}G^{\gamma}_{CrC_{1/3}}-({}^{o}G^{\alpha}_{Cr}-{}^{o}G^{\gamma}_{Cr})-\frac{1}{3}({}^{o}G^{\alpha}_{C}-{}^{o}G^{\gamma}_{C})$ cal/mole (Cr)

TABLE 7

Experimental tie-lines for the α-γ equilibrium

T °C	Equilibration time (sec)	Alloy Composition		Ferrite Composition		Austenite Composition		$K_{Cr}^{\alpha/\gamma}$(expl)	$K_{Cr}^{\alpha/\gamma}$(calc)
		X_C	X_{Cr}	X_C	X_{Cr}	X_C	X_{Cr}	$X_{Cr}^{\gamma}/X_{Cr}^{\alpha}$	$X_{Cr}^{\gamma}/X_{Cr}^{\alpha}$
770	5.5×10^6	.01	.0042	.00067	.0033	.022	.0055	1.66	1.75
770	5.5×10^6	.0165	.0093	.00061	.0060	.021	.0104	1.73	1.75
750	1.06×10^7	.0133	.0042	.00077	.0031	.026	.0055	1.78	2.01

TABLE 8

Experimental tie-lines for the γ-cm equilibrium

T °C	Equilibration time (sec)	Alloy Composition		Austenite Composition		Cementite Composition		$\frac{Y^{cm}_{Cr}}{Y^{\gamma}_{Cr}}$	$\frac{Y^{cm}_{Cr}}{Y^{\gamma}_{Cr}}$ (calc)
		X_C	X_{Cr}	X_C	X_{Cr}	X_C	X_{Cr}		
770	2.75×10^6	.0396	.0091	.0332	.0072	.25	.0731	13.1	13.4
770	2.75×10^6	.0431	.0185	.0305	.0116	.25	.1330	14.8	13.6
750	3.2×10^6	.0387	.0092	.0225	.0067	.25	.0912	17.4	15.0

TABLE 9

Experimental tie-lines for the α-cm equilibrium

Alloy Composition		Equilibration time (sec)	Ferrite Composition		Cementite Composition		X^{cm}_{Cr} (calc)	$Y^{cm}_{Cr}/Y^{\alpha}_{Cr}$	$Y^{cm}_{Cr}/Y^{\alpha}_{Cr}$ (cal
X_C	X_{Cr}		X_C	X_{Cr}	X_C	X_{Cr}			
.0201	.0042	1.3×10^6	.0006	.0013	.25	.0382	.0400	38.0	46.5
.0237	.0093	1.3×10^6	.0005	.0015	.25	.0856	.0775	76.1	44.5
.0308	.0187	1.3×10^6	.00047	.0037	.25	.1268	.1260	45.9	42.5

TABLE 10

Results for the alloy treated in the three phase (α-γ-cm) region at 750°C

Alloy Composition		Equilibration time (sec)	X_{Cr}^{cm}		V^{γ}		V^{cm}	
X_C	X_{Cr}		Exp.	Calc	Exp.	Calc	Exp.	Calc
.0273	.0188	3.2×10^6	.143	.150	.275	.25	.069	.065

TABLE 11

Composition of the alloys used for pearlite transformation experiments

Alloy	At % Cr	At % C	Nominal % Cr
A	0.42	3.39	0.4
B	0.91	3.26	0.9
C	1.87	2.73	1.8

TABLE 12

Experimental growth rates and interlamellar spacings for 1.8% chromium alloy

Temperature °C	Growth rate μcm/sec		Interlamellar spacing
	Max. Nodule	Cahn and Hagel	μcm
720	0.38	-	.135
705	0.87	0.50	.092
690	1.82	1.4, 1.14, 1.13	.069
670	2.2	2.4, 1.98, 2.1	.060
650	2.0	2.1, 2.0	.0463
630	1.75	1.65, 1.7	.0407
620	1.7	-	.0370

TABLE 13

Experimental growth rates and interlamellar spacings for 0.9% chromium alloy

Temperature °C	Growth rate μcm/sec	Interlamellar spacing μcm
710	0.38	.178
700	0.9	.128
680	3.4	.088
660	6.2	.072
640	8.3	.057
618	9.5	.046

TABLE 14

Experimental growth rates and interlamellar spacings for 0.4% chromium alloy

Temperature °C	Growth rate µcm/sec	Interlamellar spacing µcm
706	0.33	.240
696	1.31	.174
680	4.2	.109
660	10.3	.079
637	24.0	.065
620	33.0	.055

TABLE 15

Calculation of $(K\delta D^B_{Cr})$ from low supersaturation pearlite growth data

T °C	$\bar{C}_{Cr}$	$v \times 10^4$ cm/sec	$1/S \times 10^3$ cm^{-1}	$C^{\gamma\alpha}_{Cr} - C^{\gamma cm}_{Cr}$	$K\delta D^B_{Cr} = \dfrac{v}{54\left[\dfrac{C^{\gamma\alpha}_{Cr} - C^{\gamma cm}_{Cr}}{\bar{C}_{Cr}}\right]\dfrac{1}{S^2}}$
720	1.8	.35	78	2.16	8.9×10^{-17}
720	1.3	.18	58	1.44	8.94×10^{-17}
710	1.8	.7	97	3.12	7.94×10^{-17}
710	1.3	.4	76	2.38	7.00×10^{-17}
710	0.9	.38	58	2.00	9.41×10^{-17}
700	1.8	1.2	107	4.44	7.87×10^{-17}
700	1.3	.84	94	3.60	6.35×10^{-17}
690	1.8	1.8	136	5.72	5.67×10^{-17}
690	1.3	1.4	112	4.76	5.65×10^{-17}
680	1.8	2.15	155	7.08	4.22×10^{-17}
670	1.8	2.2	175	8.64	2.78×10^{-17}

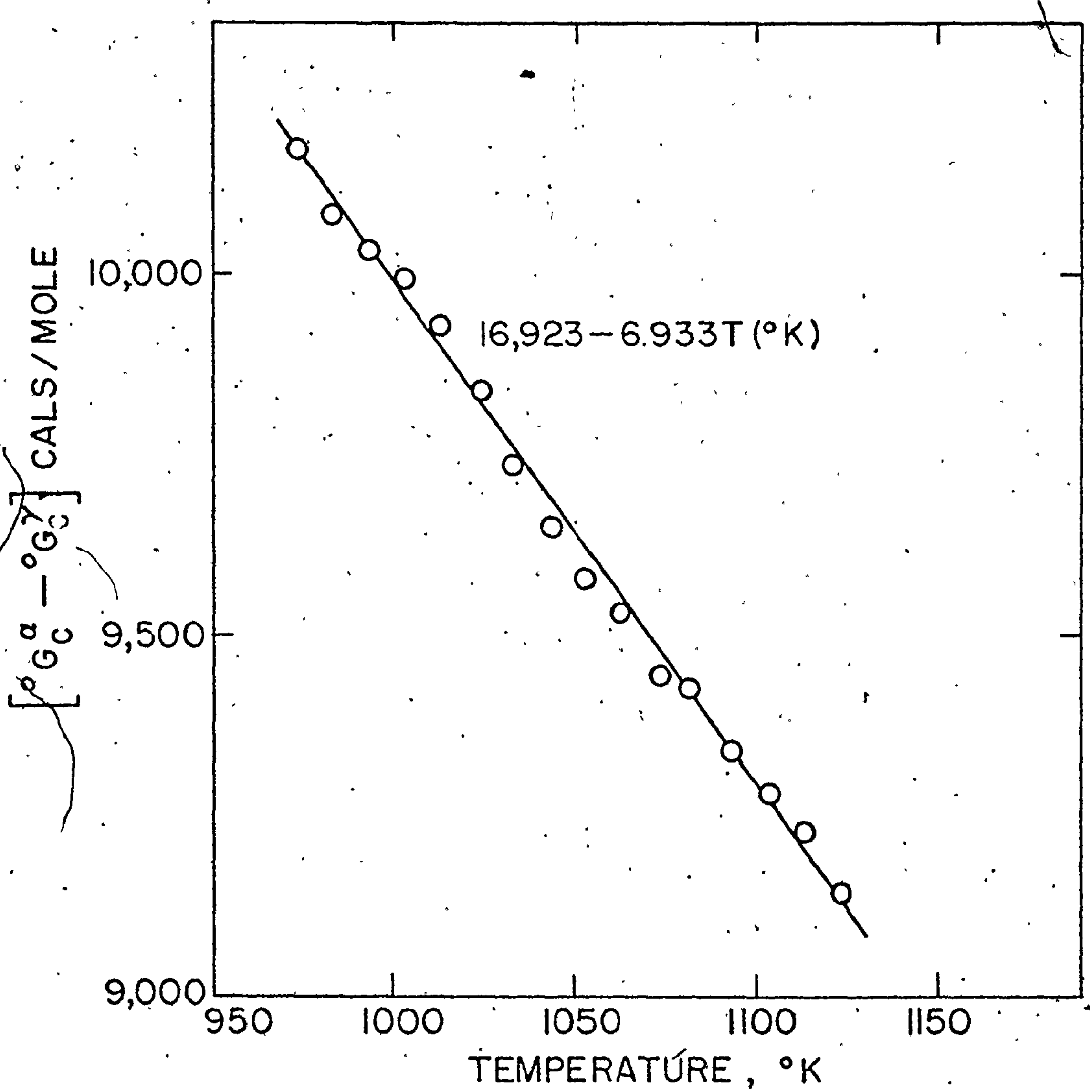

Figure 1. Calculated standard free energy change for the transfer of carbon from γ to α iron.

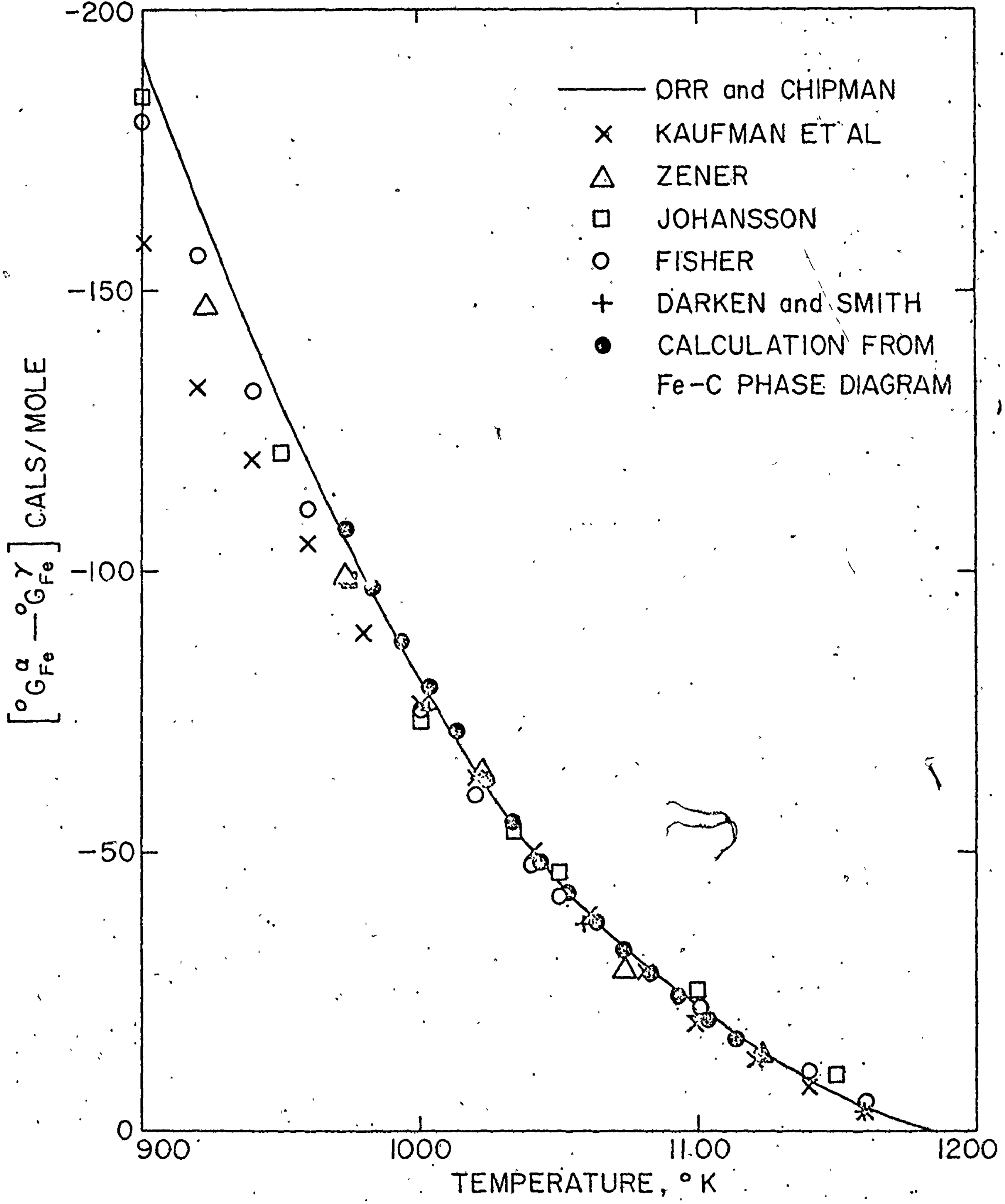

Figure 2. St ndard free energy change for the transformation iron (fcc) to

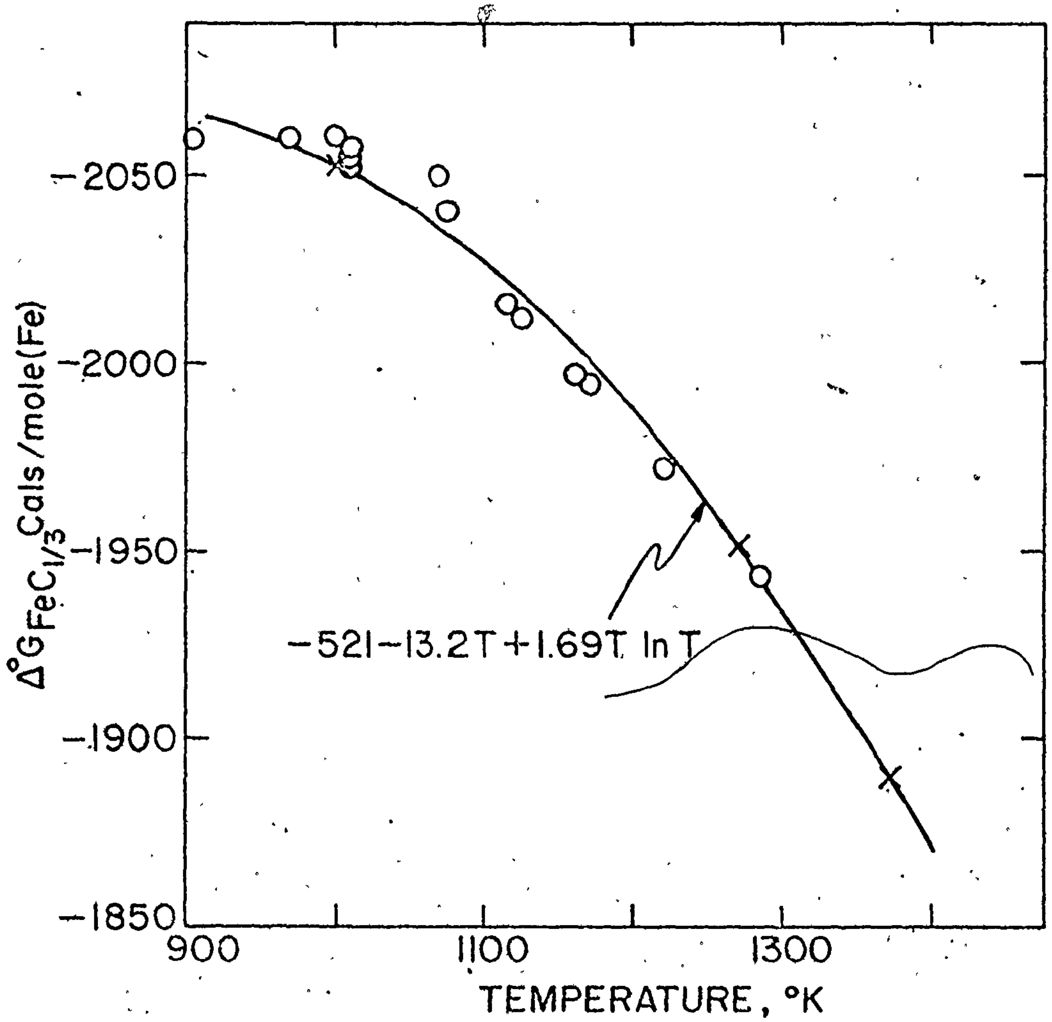

Figure 3. Standard free energy of formation of $FeC_{1/3}$ from γ iron and carbon in γ.

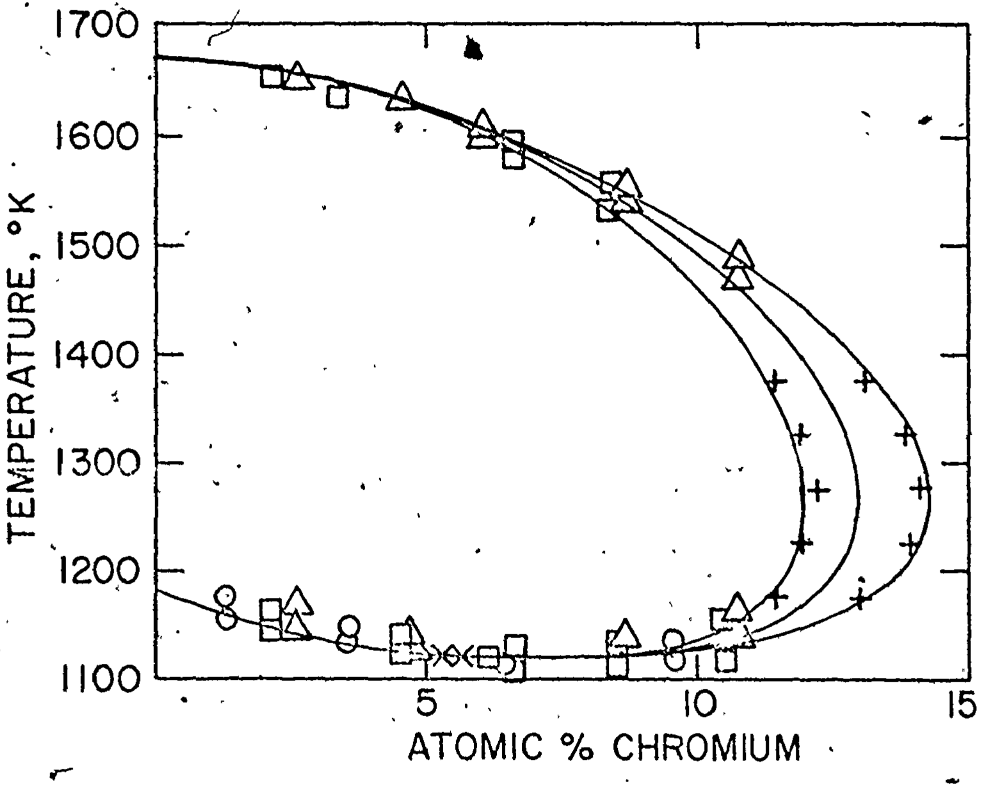

Figure 4. Calculated Fe-Cr phase diagram due to Kirchner et al.

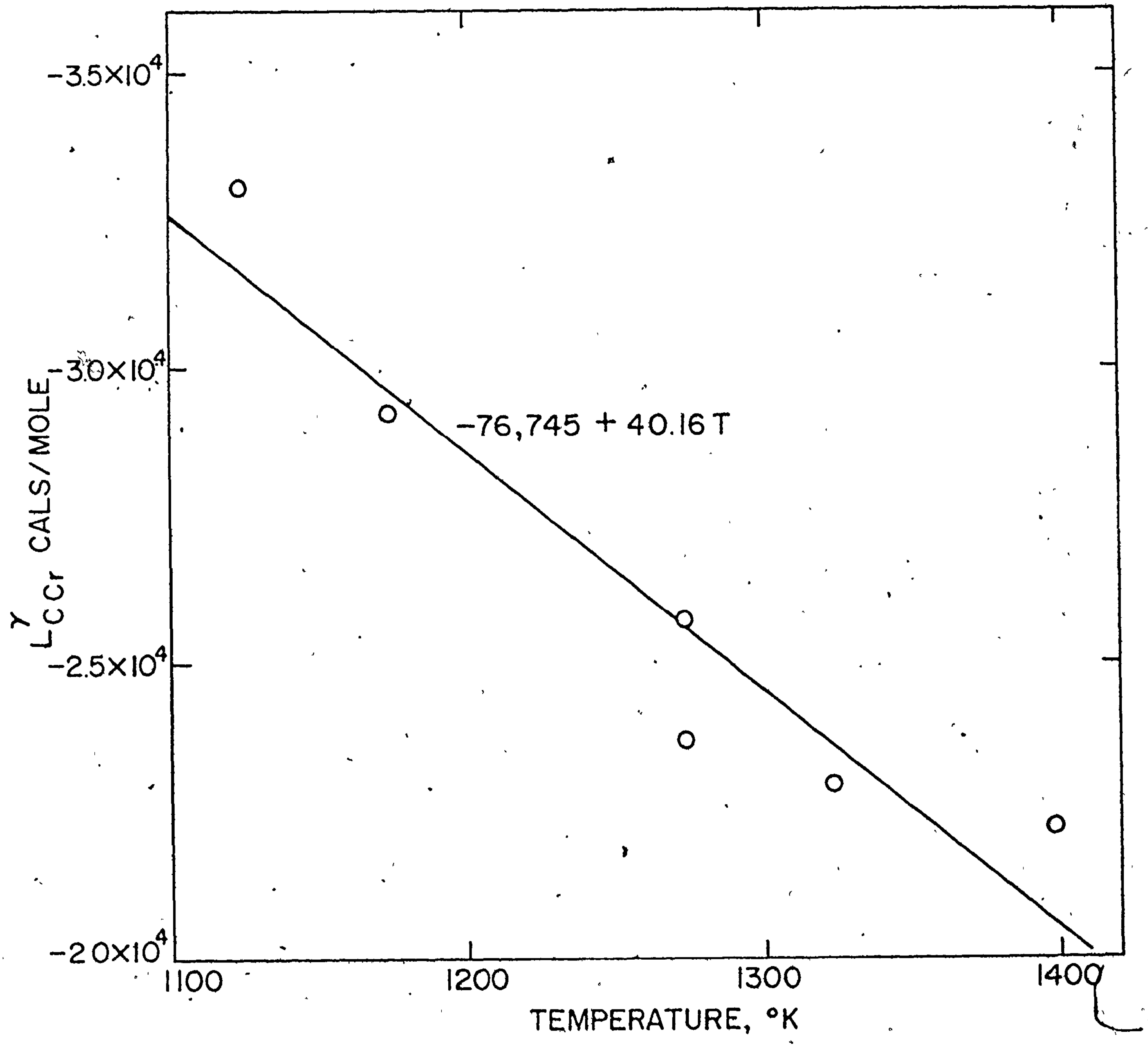

Figure 5. Parameter L^{γ}_{CCr} as a function of temperature.

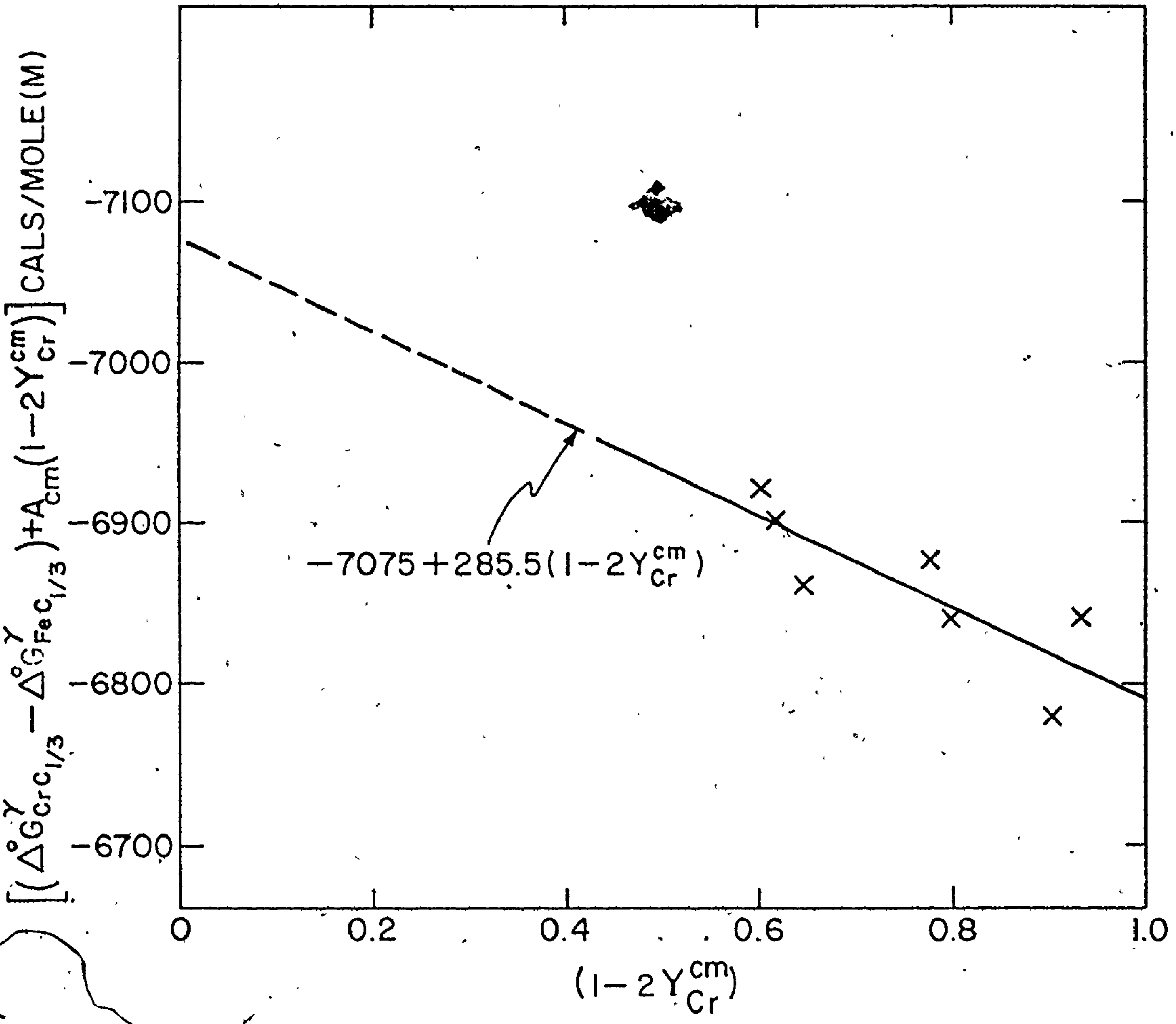

Figure 6. Evaluation of $(\Delta^{o}G^{\gamma}_{CrC_{1/3}}-\Delta^{o}G^{\gamma}_{FeC_{1/3}})$ and A_{cm}.

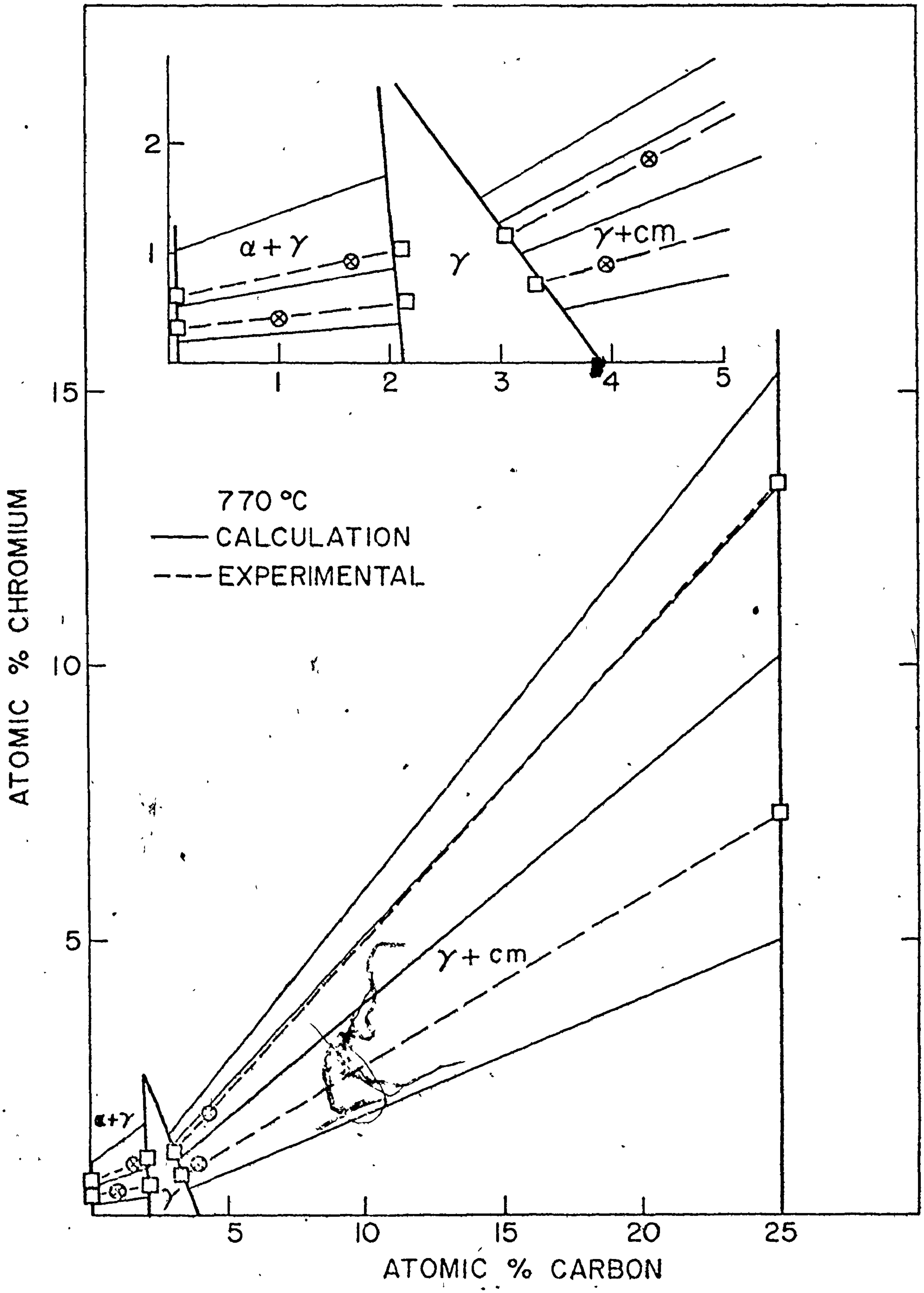

Figure 7. Isotherm for Fe-C-Cr at 770°C.

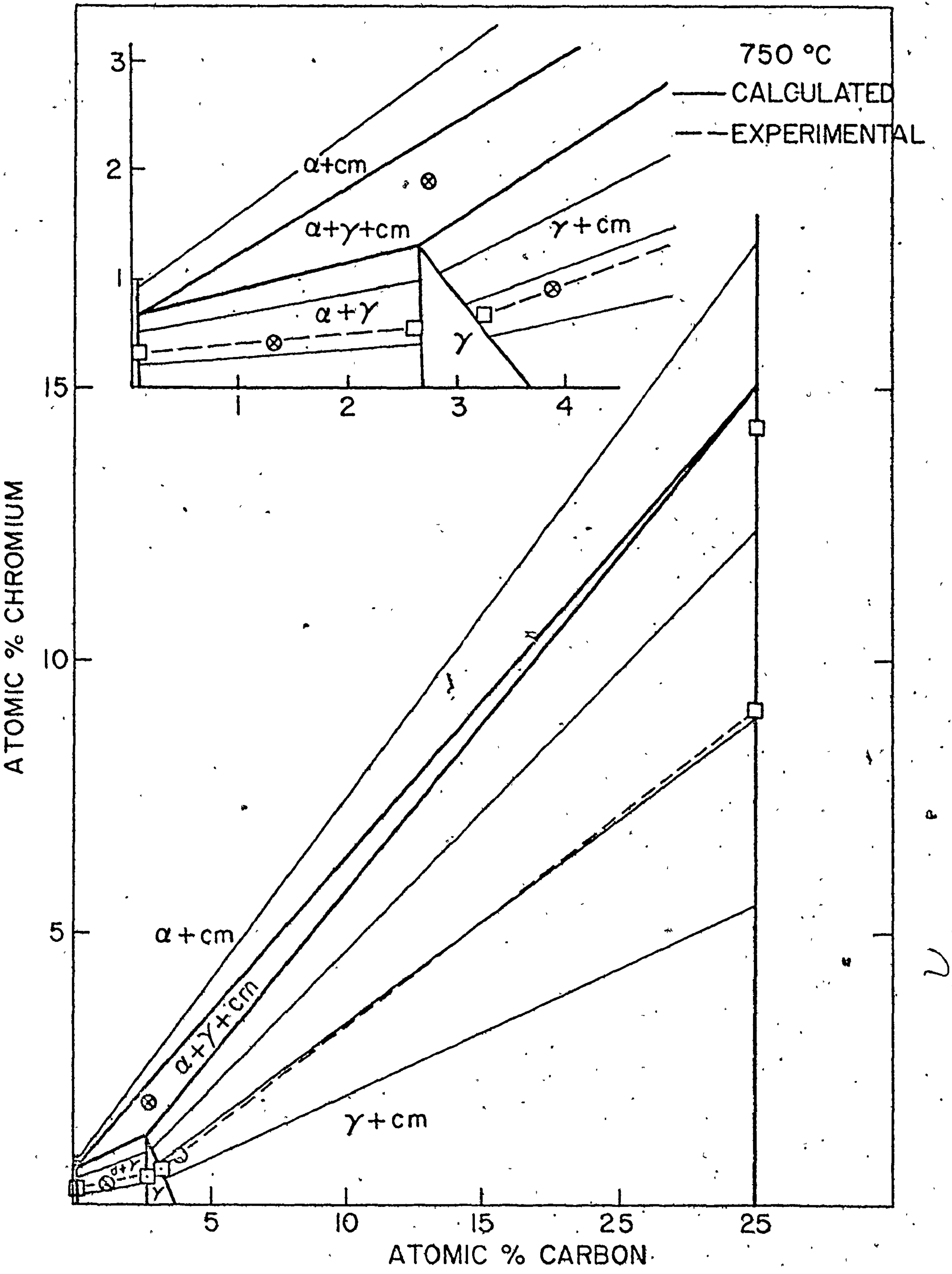

Figure 8. Isotherm for Fe-C-Cr at 750°C.

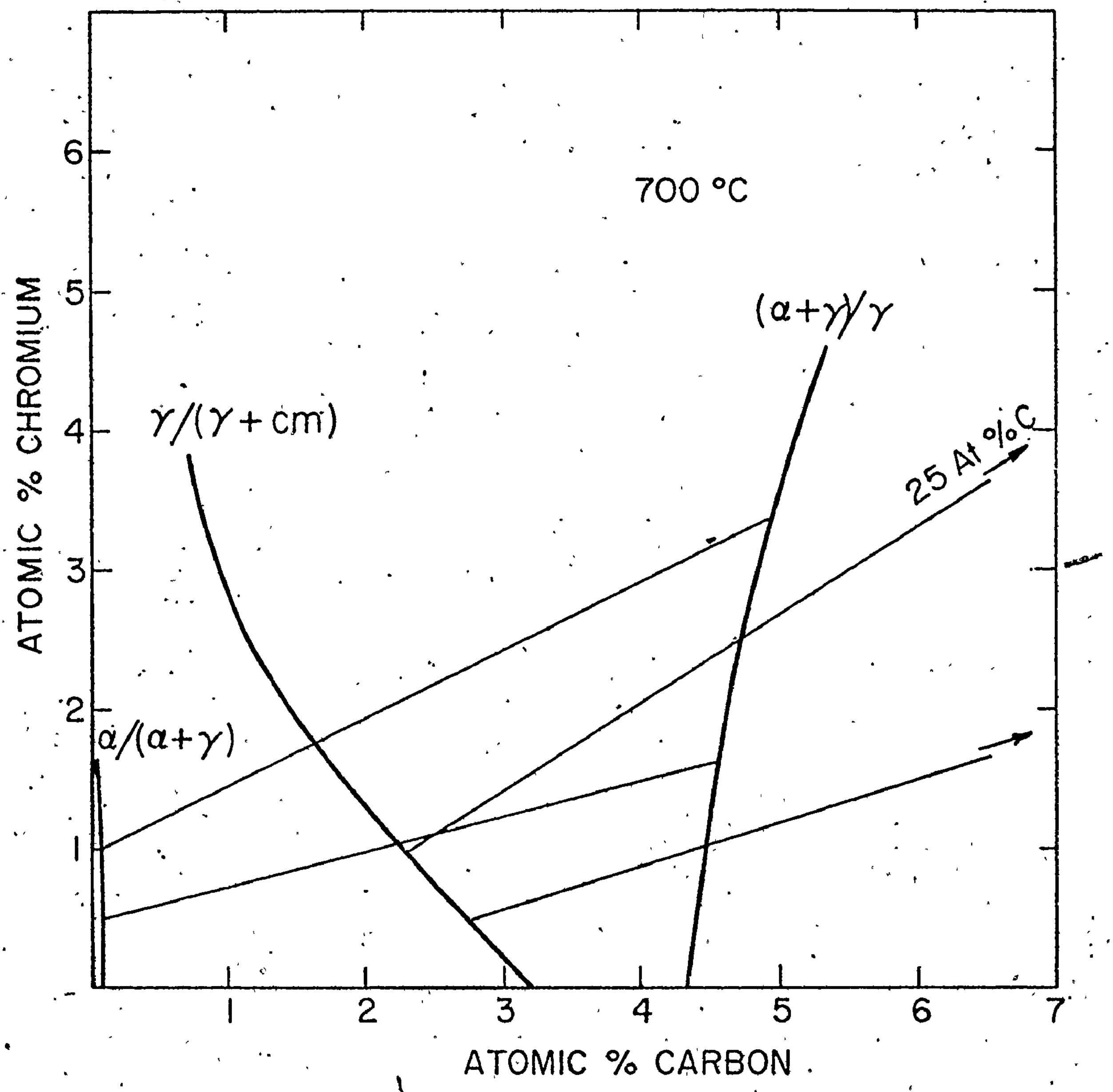

Figure 9. Metastable phase equilibria in Fe-C-Cr at 700°C.

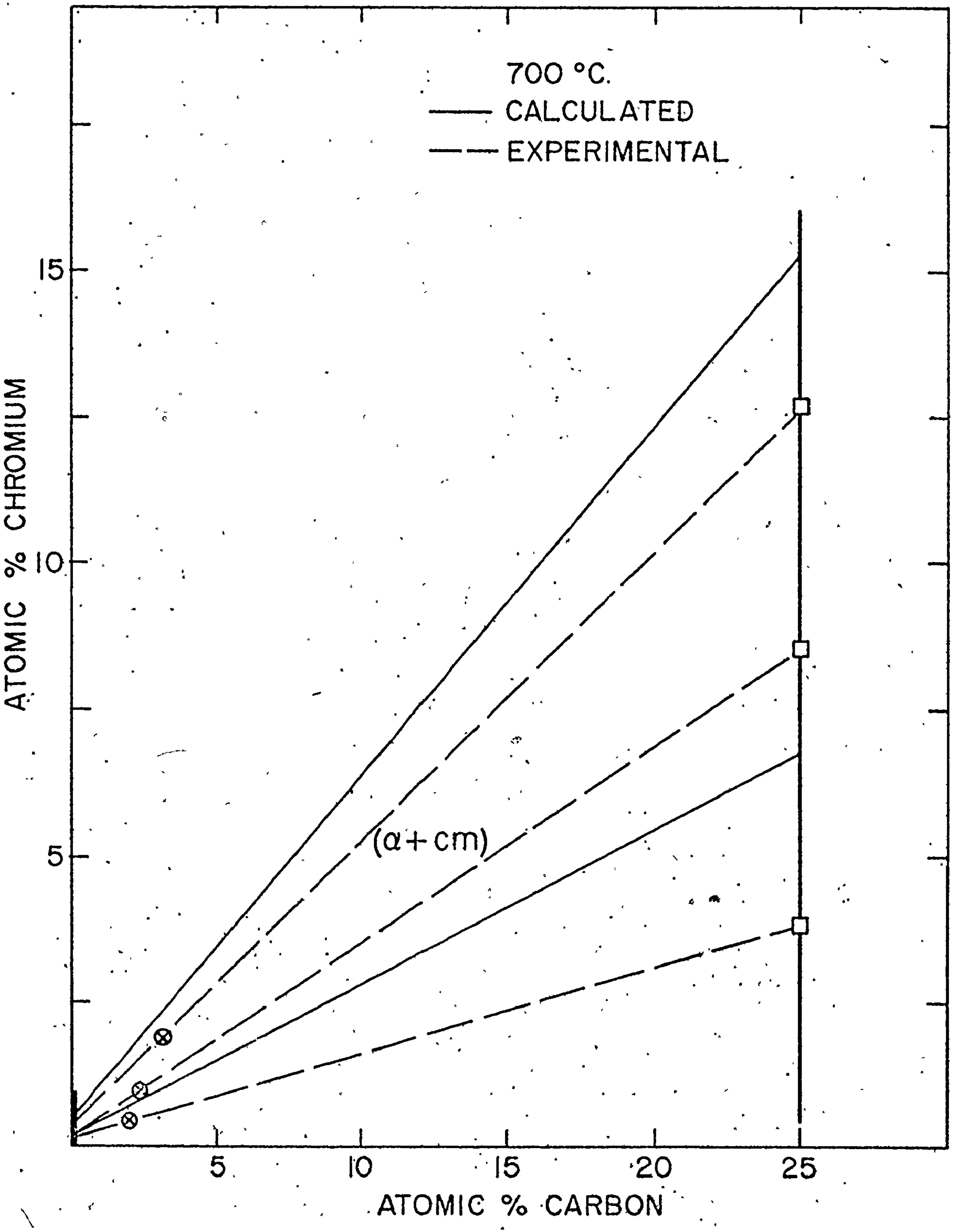

Figure 10. Isotherm for Fe-C-Cr at 700°C.

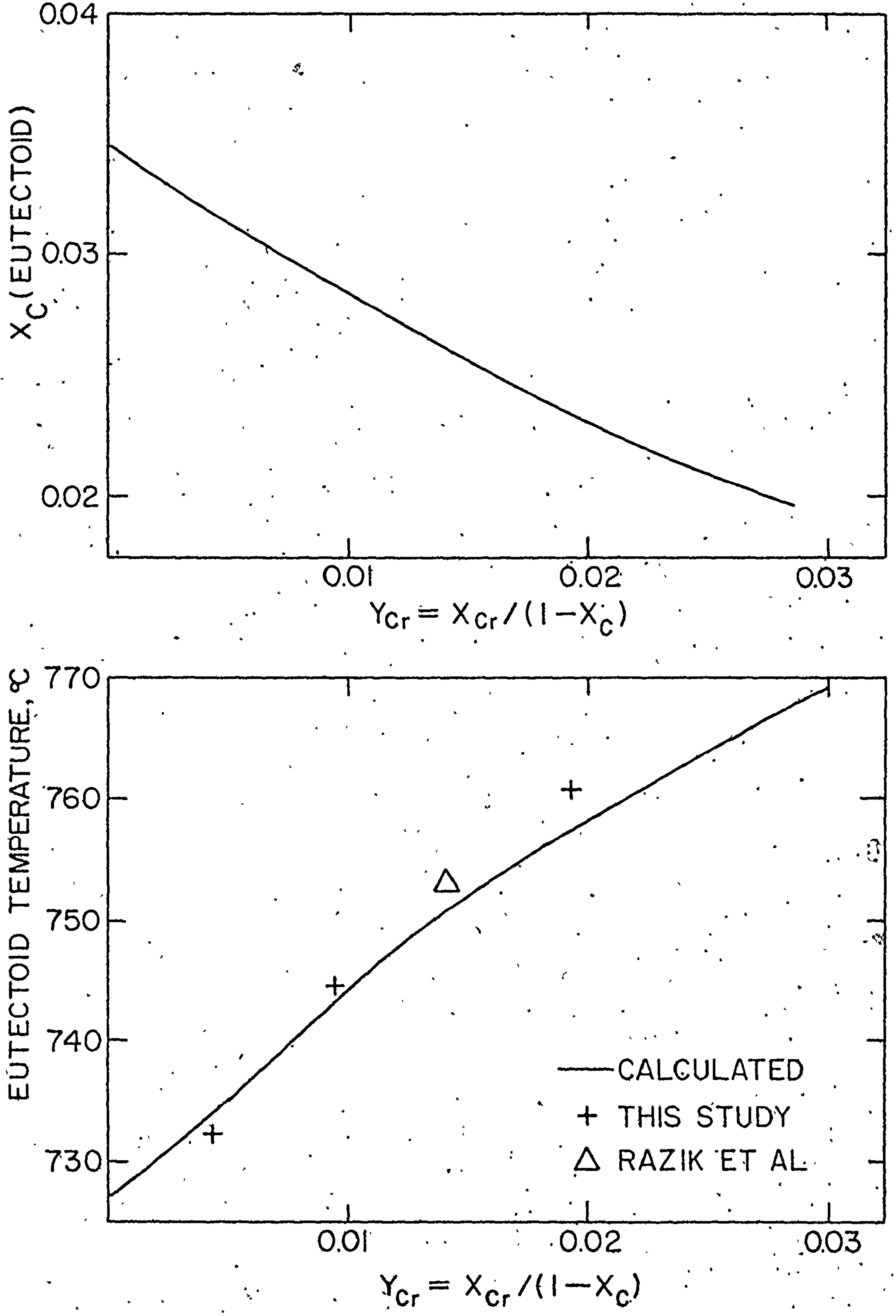

Figure 11. Variation of the eutectoid point as a function of chromium in the Fe-C-Cr system.

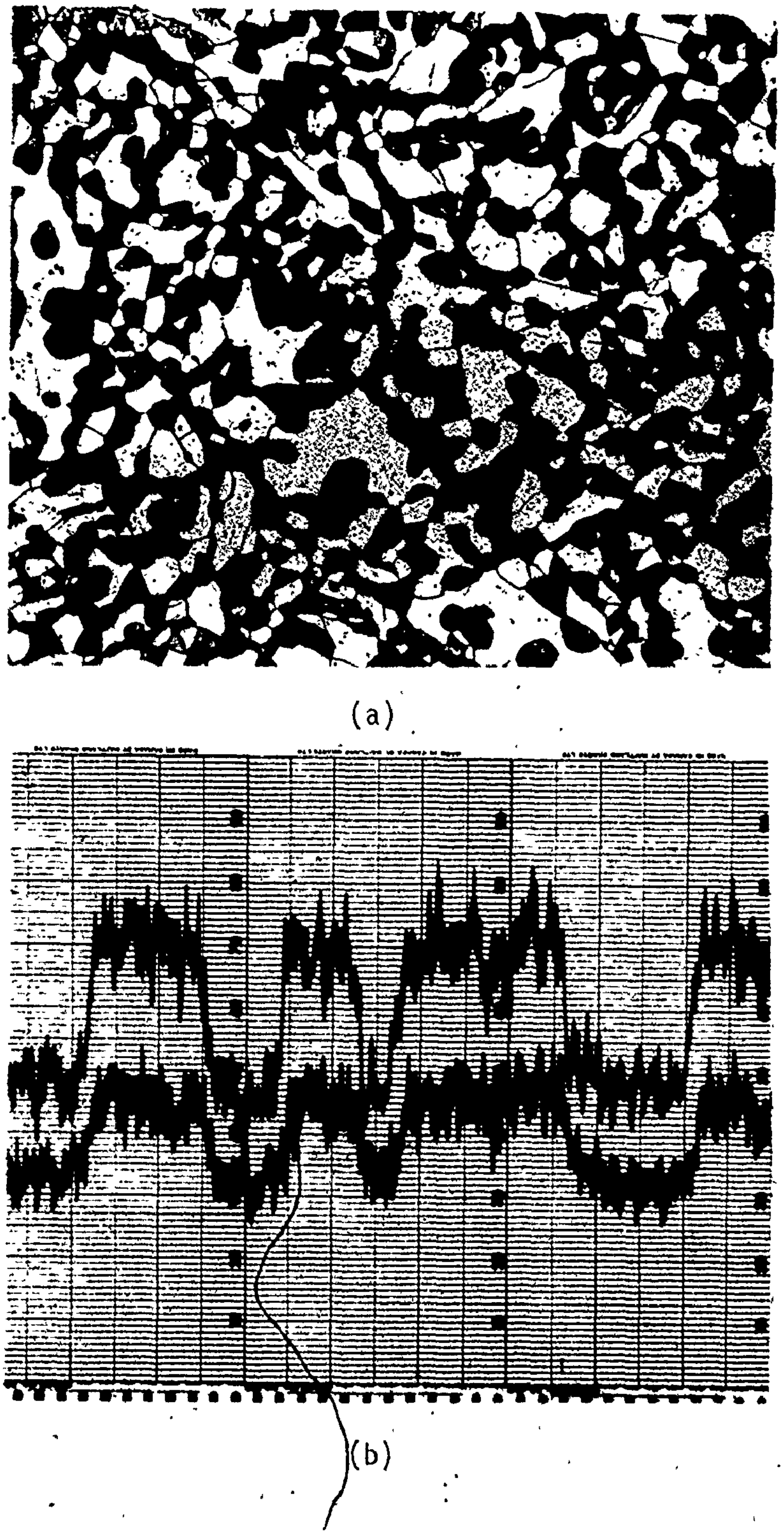

Figure 12. Typical (a) optical photomicrograph (x100) and (b) microprobe scan of the Fe-C-Cr alloy equilibrated in the ($\alpha+\gamma$) region.

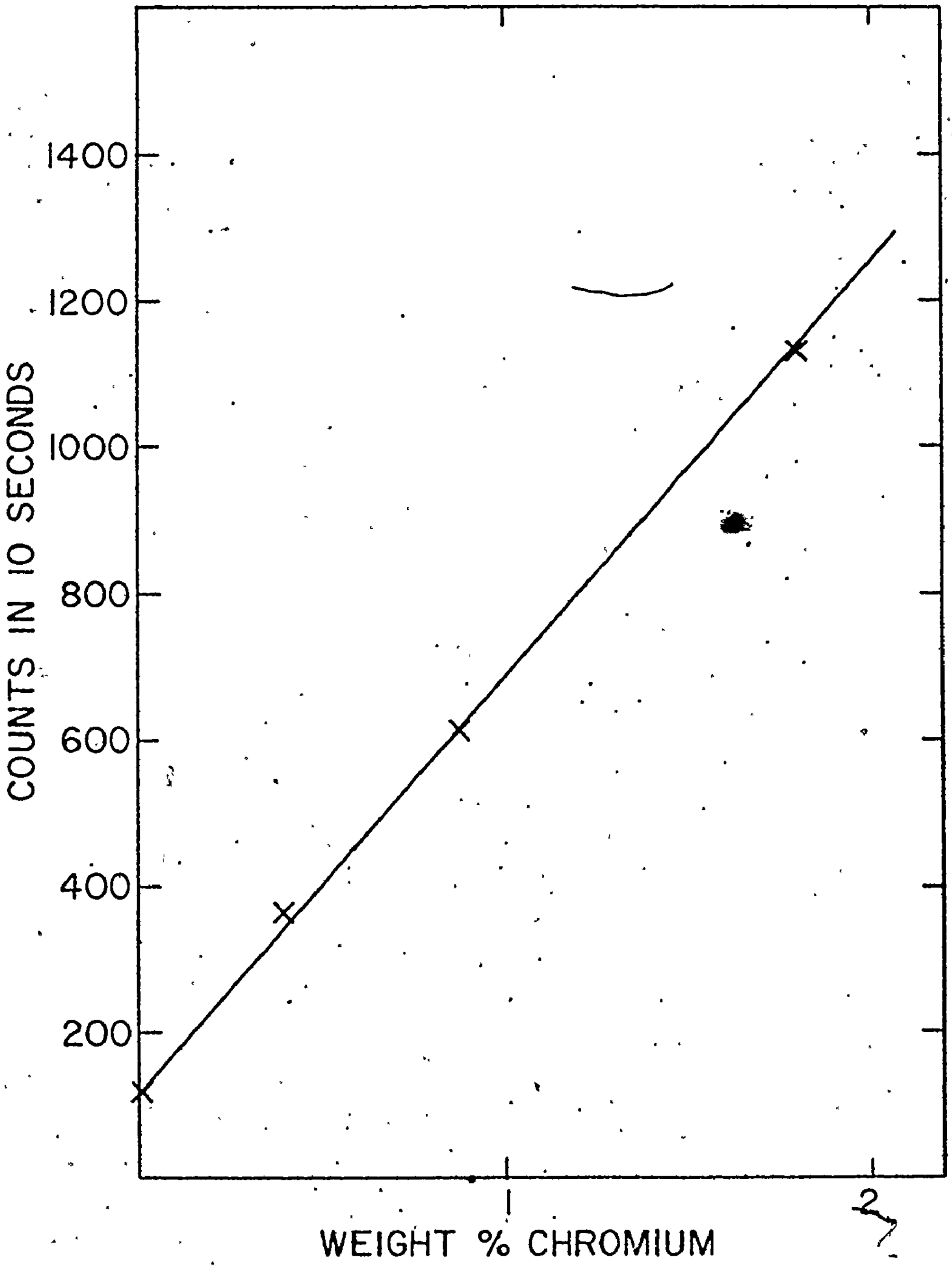

Figure 13. Typical calibration curve for the electron microprobe analyser.

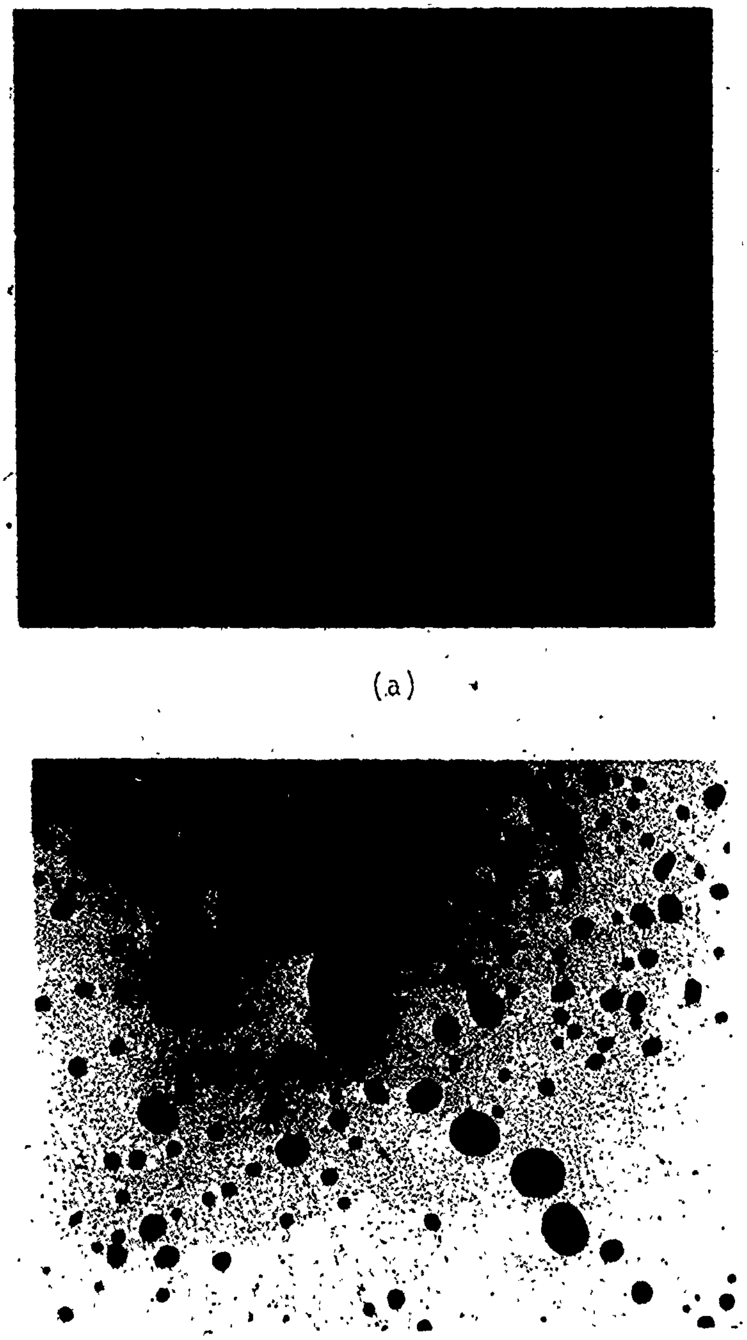
(a)

(b)

Figure 14. Typical (a) optical photomicrograph (x1350) and (b) carbon extraction replica photomicrograph (x7000) of the Fe-C-Cr alloy equilibrated in the (γ+cm) region.

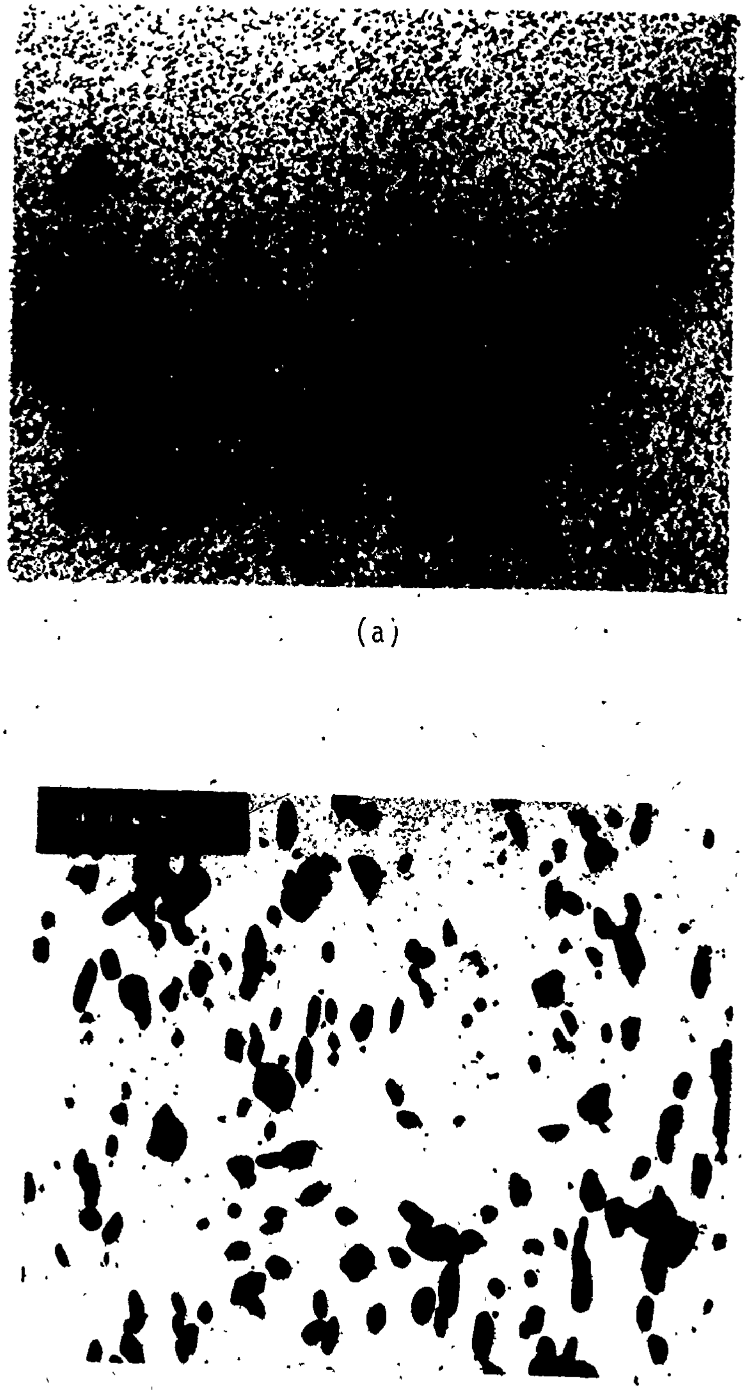

(a)

(b)

Figure 15. Typical (a) optical photomicrograph (x720) and (b) carbon extraction replica photomicrograph (x5500) of the Fe-C-Cr alloy equilibrated in the (α+cm) region.

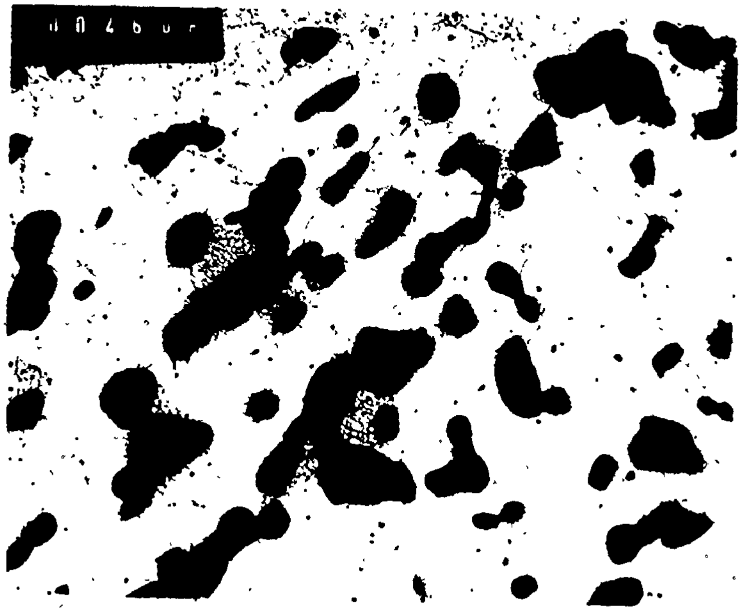

Figure 16. Typical carbon extraction replica photomicrograph of the Fe-C alloy equilibrated in (α+cm) region (x5500).

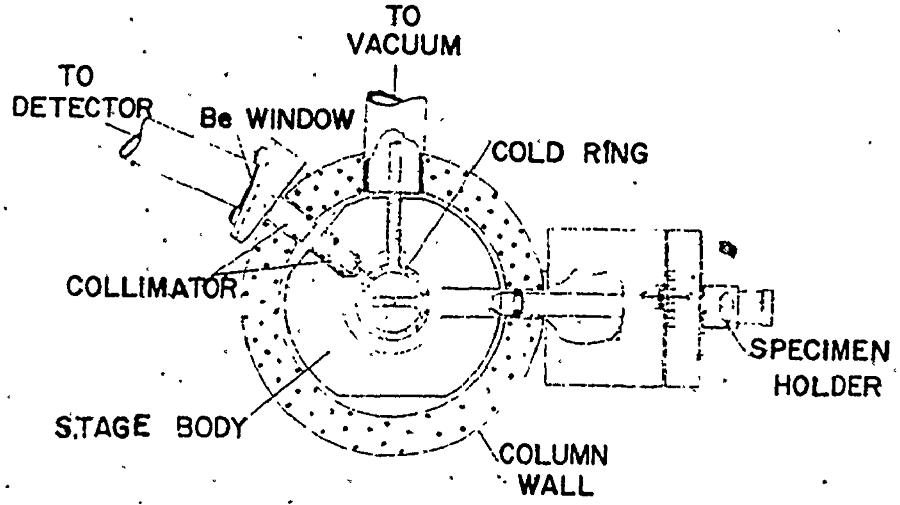

Figure 17(a). Schematic diagram of a cross section through the Philips EM300 electron microscope at the sample holder.

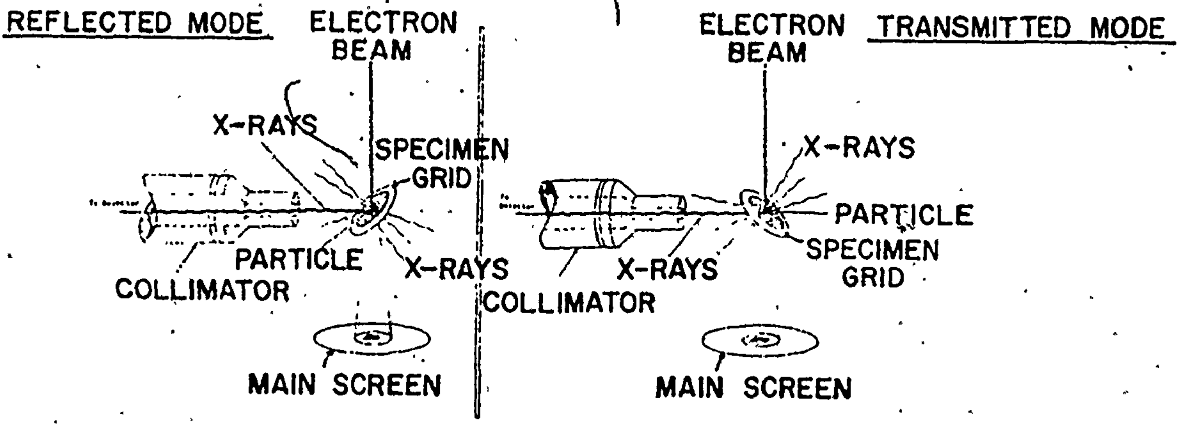

Figure 17(b). Schematic diagram of the sample to collimator position in the "reflection" and "transmission" modes.

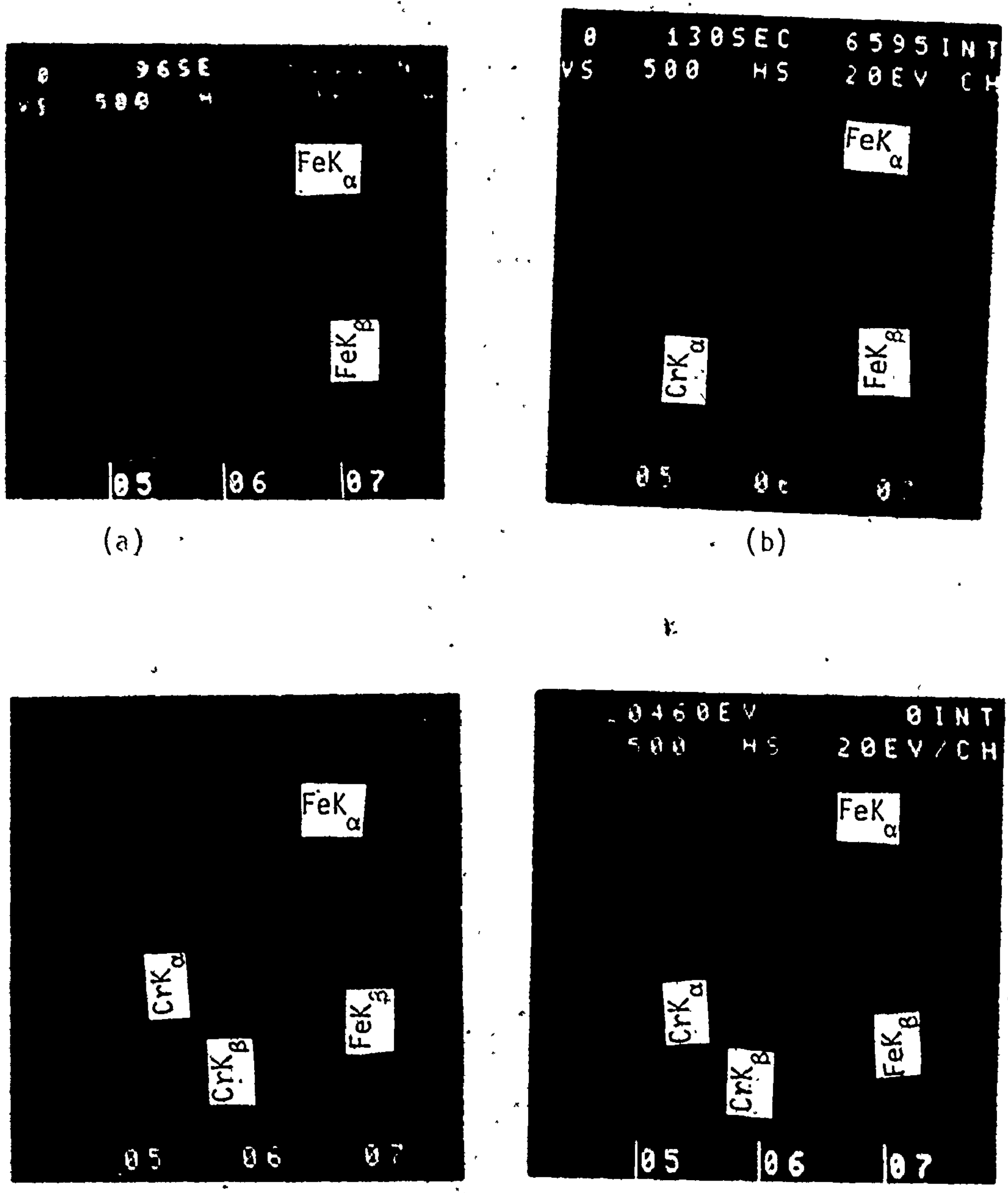

(a) (b)

(c) (d)

Figure 18. Typical X-ray spectra of the carbide particle analysis by EDAX on the Philips EM300 for the Fe-C-Cr alloys equilibrated in the (α+cm) region. (a) 0% Cr, (b) 0.4% Cr, (c) 1.8% Cr and (d) same as (c) with background subtracted.

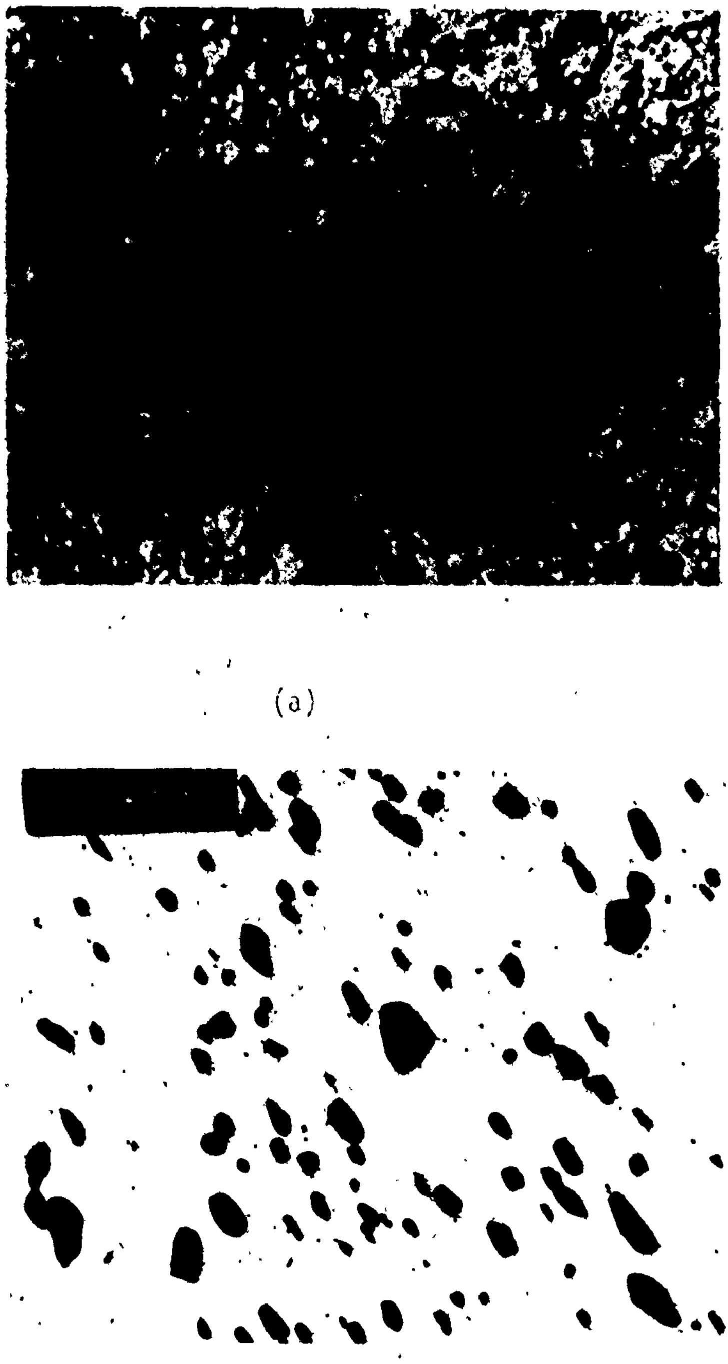

Figure 19. Typical (a) optical photomicrograph (x850) and (b) carbon extraction replica photomicrograph (x5300) of the Fe-C-Cr alloy equilibrated in the three phase, ($\alpha+\gamma+cm$) region.

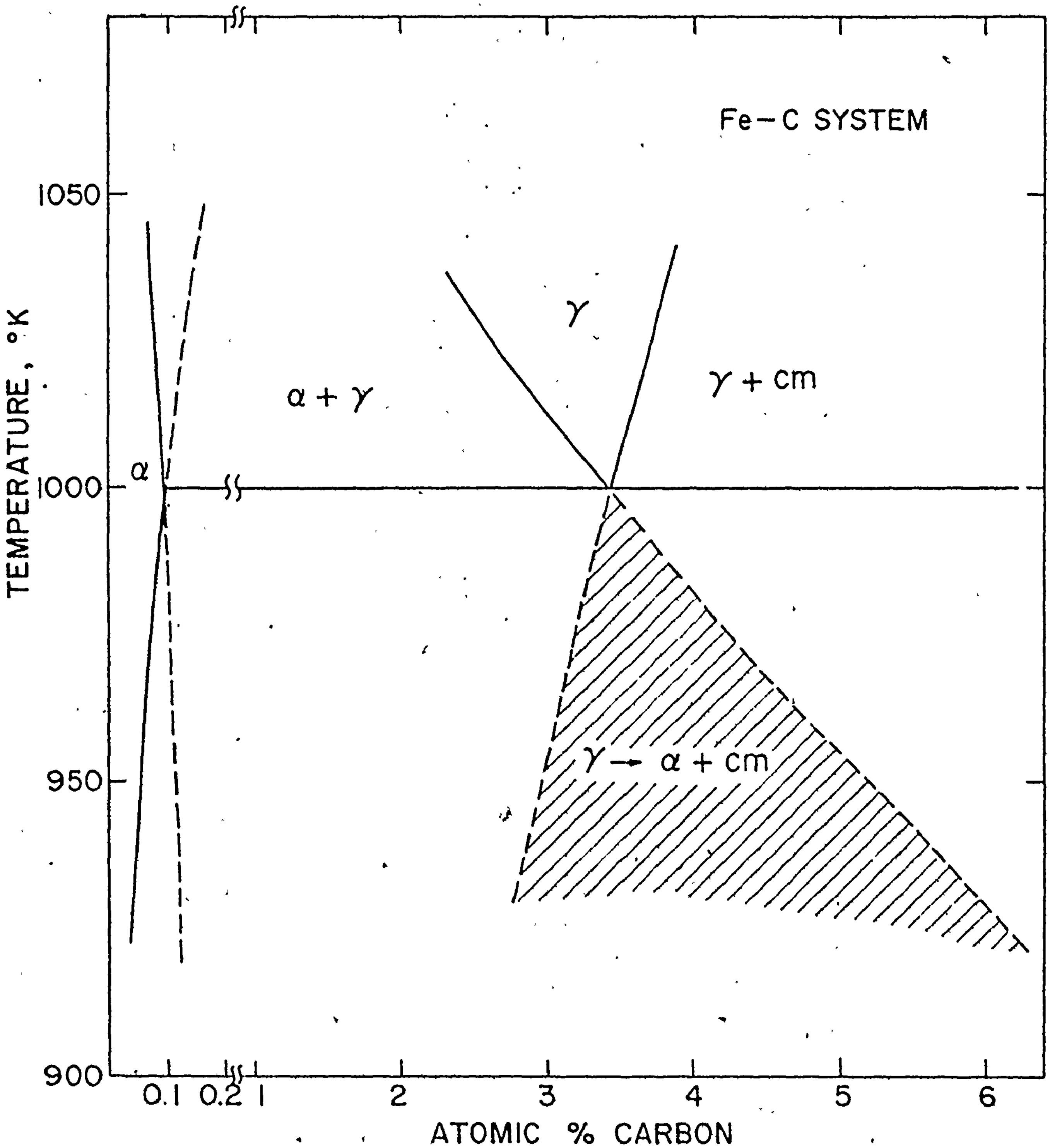

Figure 20. Calculated binary Fe-C phase diagram.

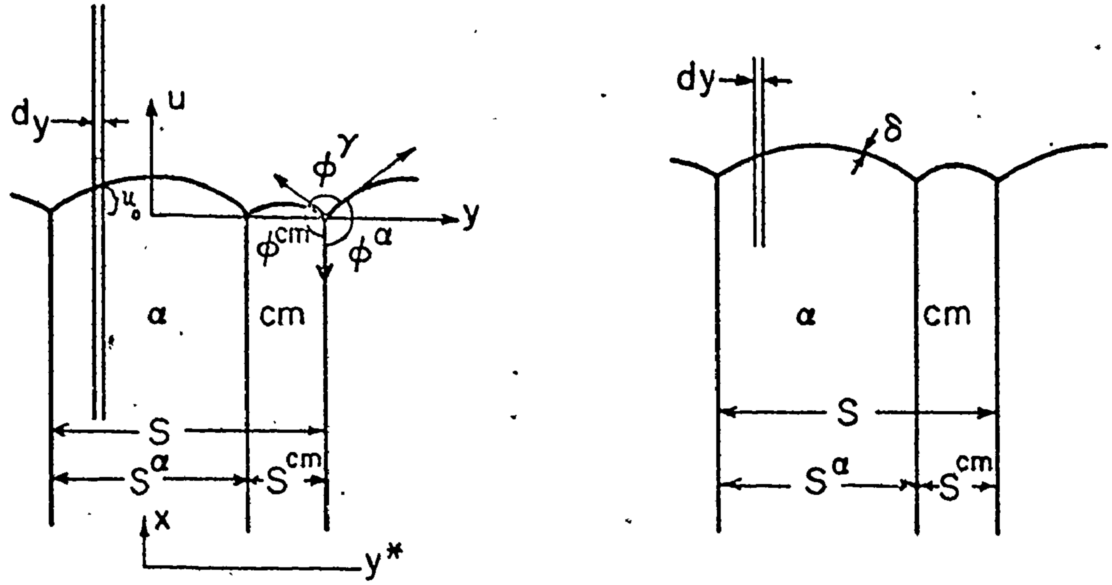

(i) (ii)

Figure 21(a). Representation of the growth of lamellar structure by (i) volume diffusion and (ii) boundary diffusion.

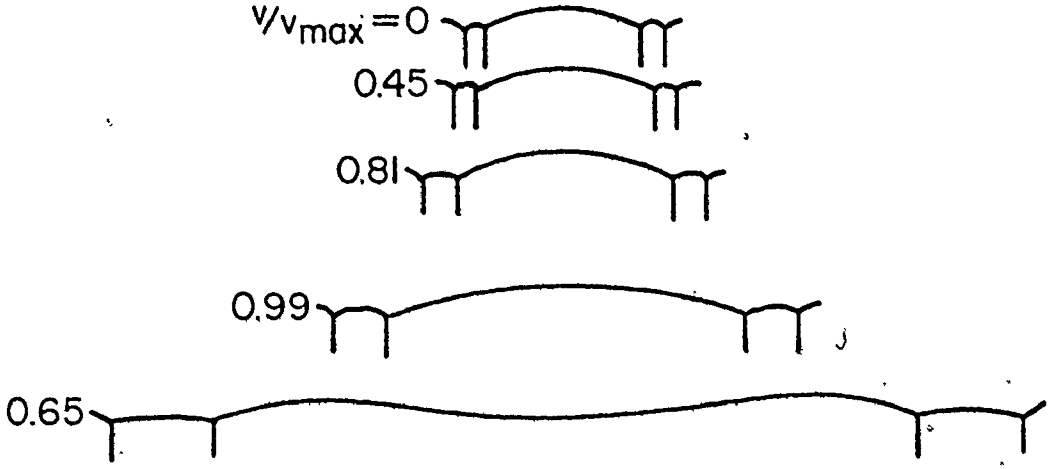

Figure 21(b). Calculated shape and growth rate of pearlite with different interlamellar spacings due to Hillert.$^{(11)}$

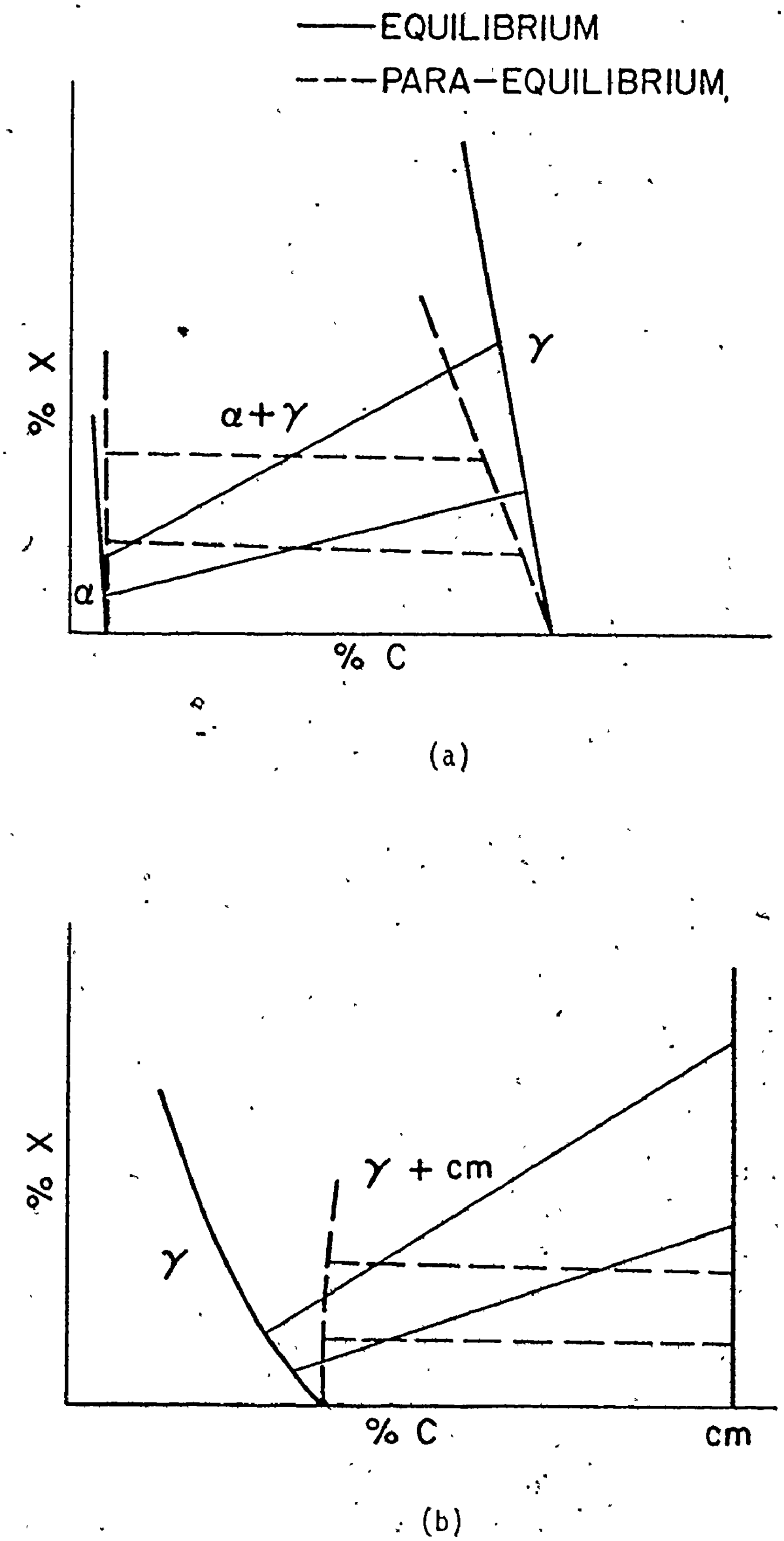

(a)

(b)

Figure 22. Schematic representation of para-equilibrium in Fe-C-X system for (a) the γ→α and (b) the γ→cm transformation.

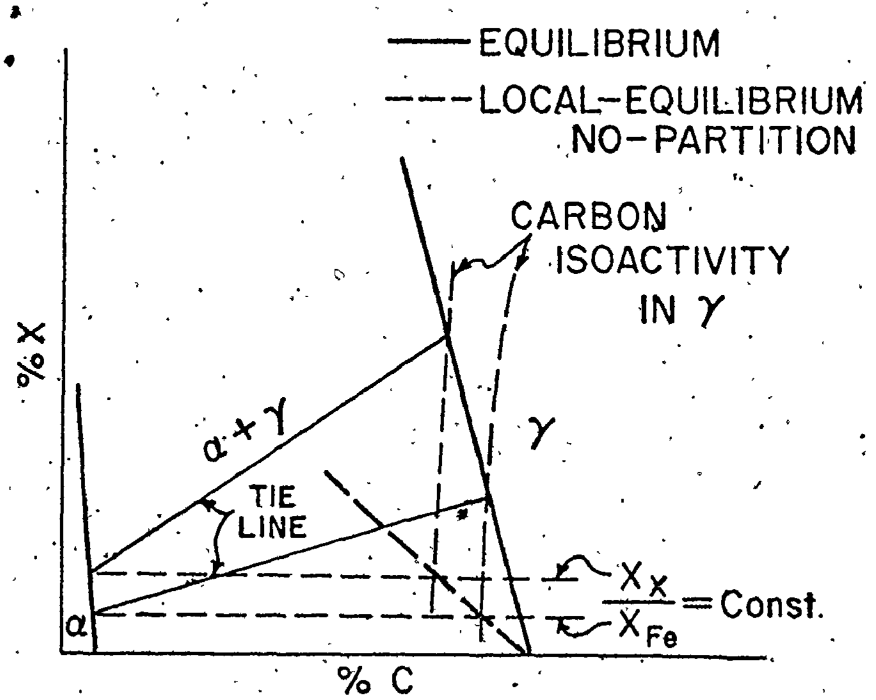

(a)

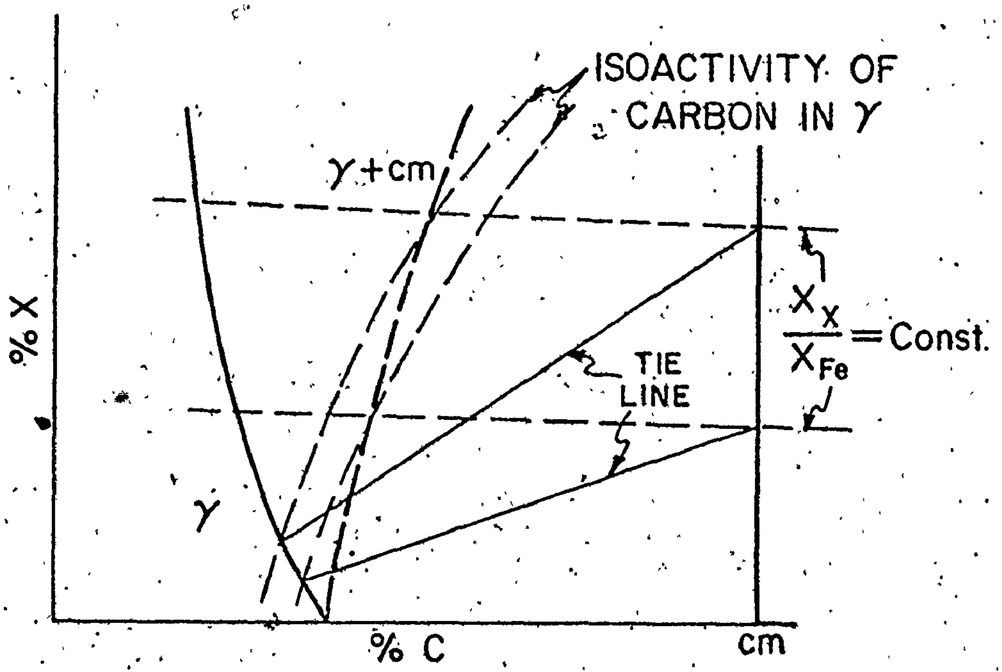

(b)

Figure 23. Schematic representation of the local equilibrium no-partition phase boundary in the Fe-C-X system for (a) the γ→α and (b) the γ→cm transformation.

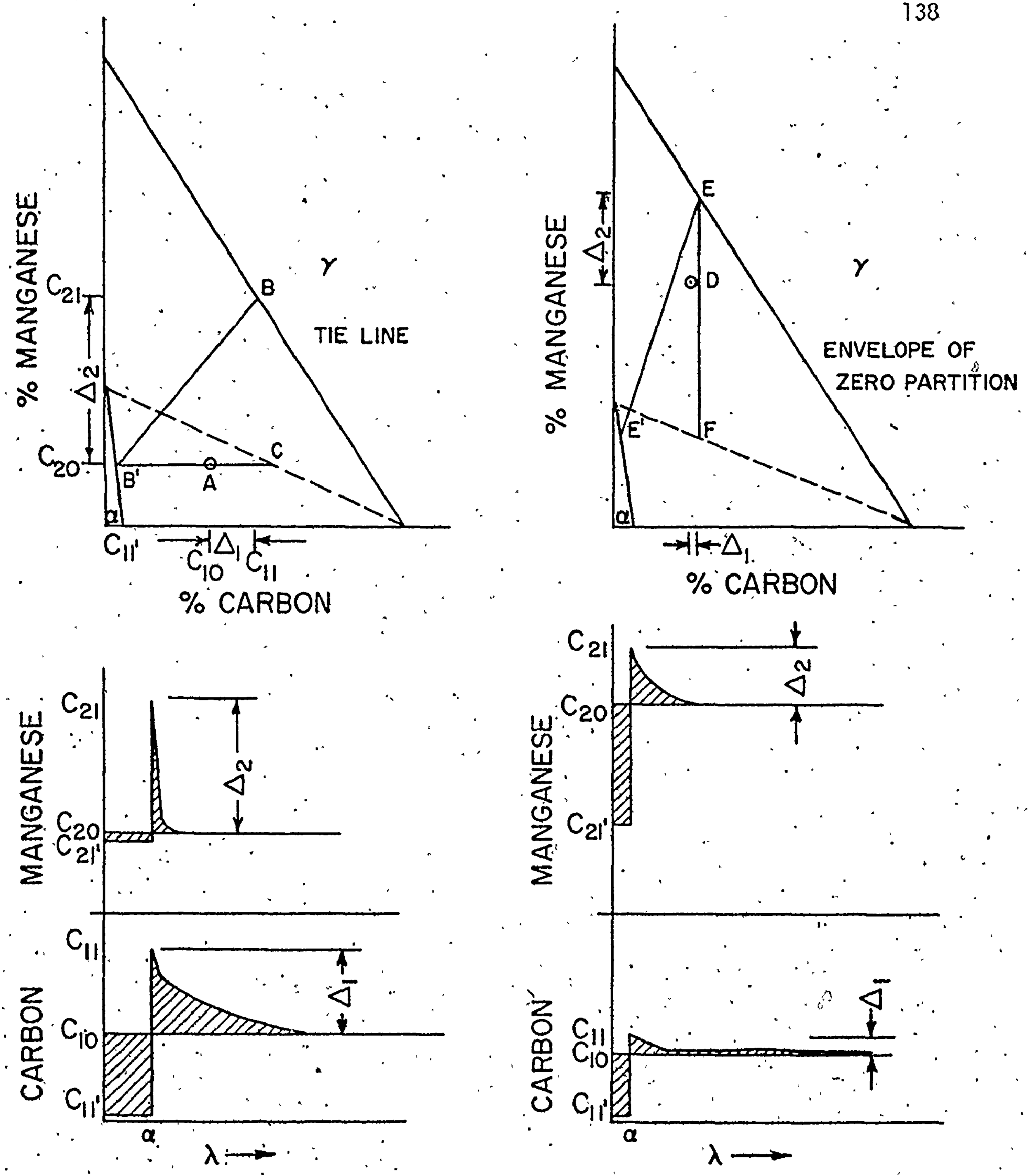

Figure 24. Schematic penetration curves in λ space for ferrite growth in Fe-C-Mn austenites. The mass balances are represented by equal shaded areas on either side of the interface ($\lambda=\alpha$). (after Purdy, Weichert and Kirkaldy)

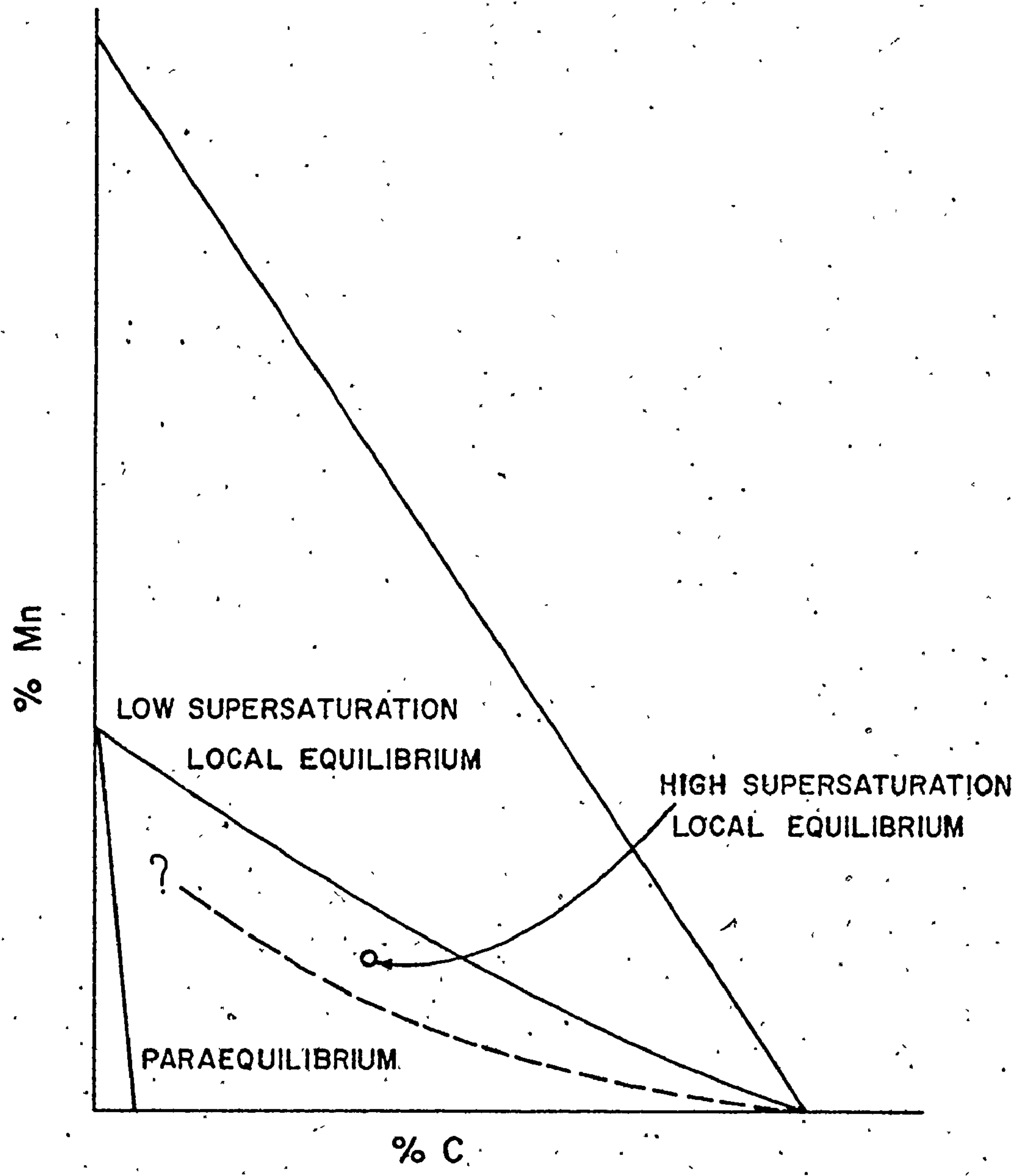

Figure 25. Schematic representation of the local equilibrium - para-equilibrium areas of the proeutectoid transformation in Fe-C-Mn alloys. (after Gilmour)

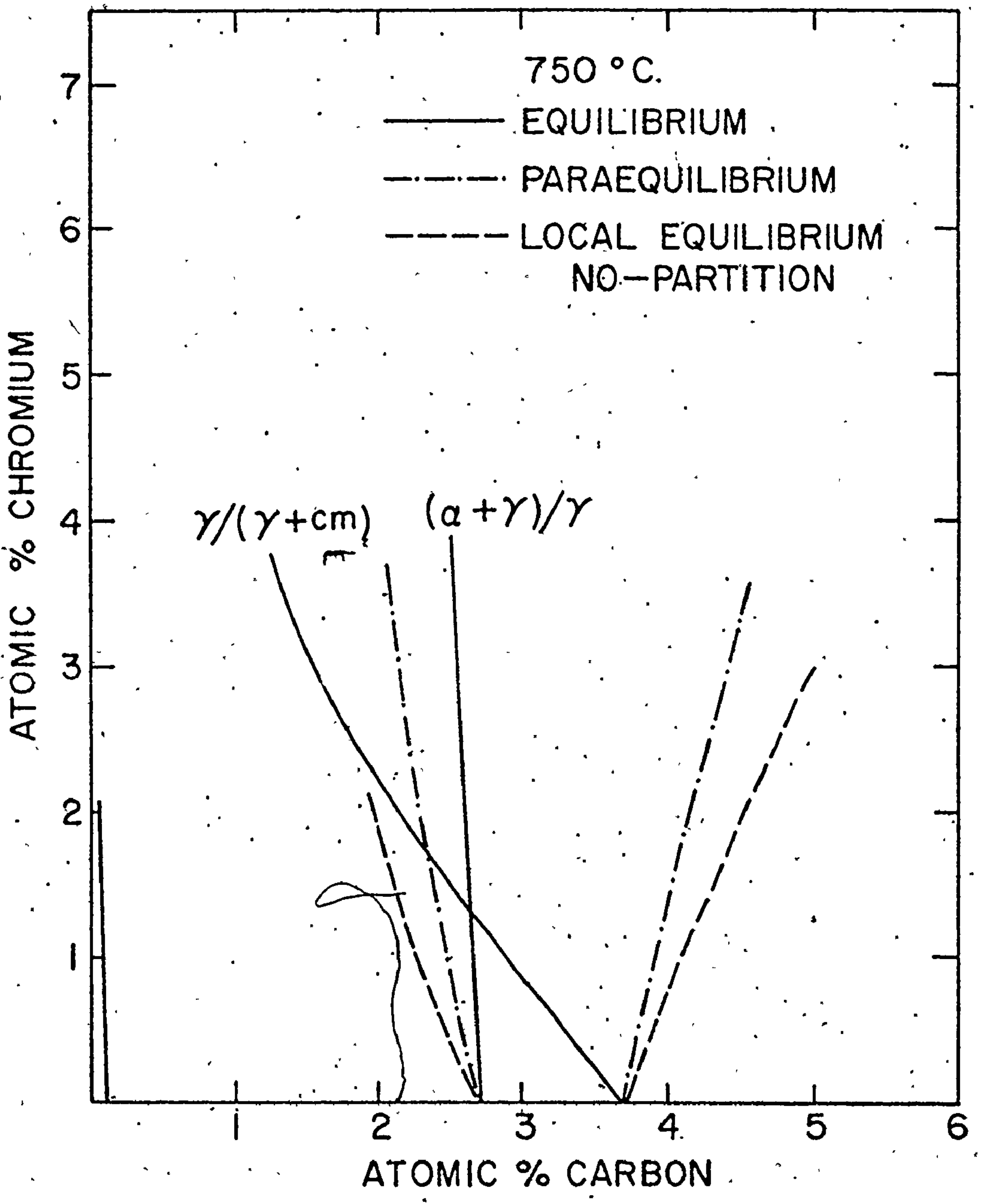

Figure 26. Calculated para-equilibrium and local equilibrium no-partition phase boundaries, in Fe-C-Cr at 750°C.

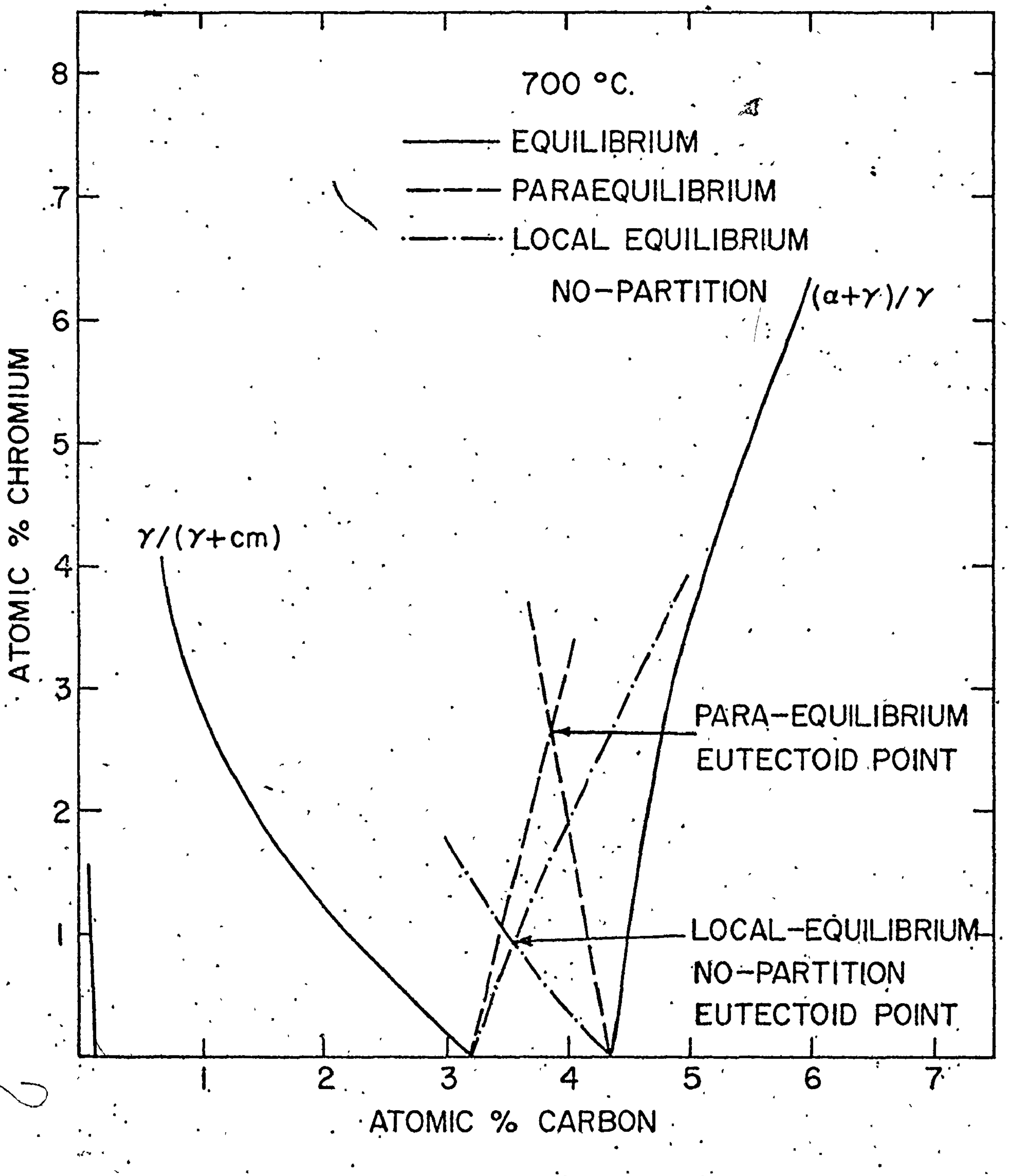

Figure 27. Calculated para-equilibrium and local equilibrium no-partition phase boundaries in Fe-C-Cr at 700°C

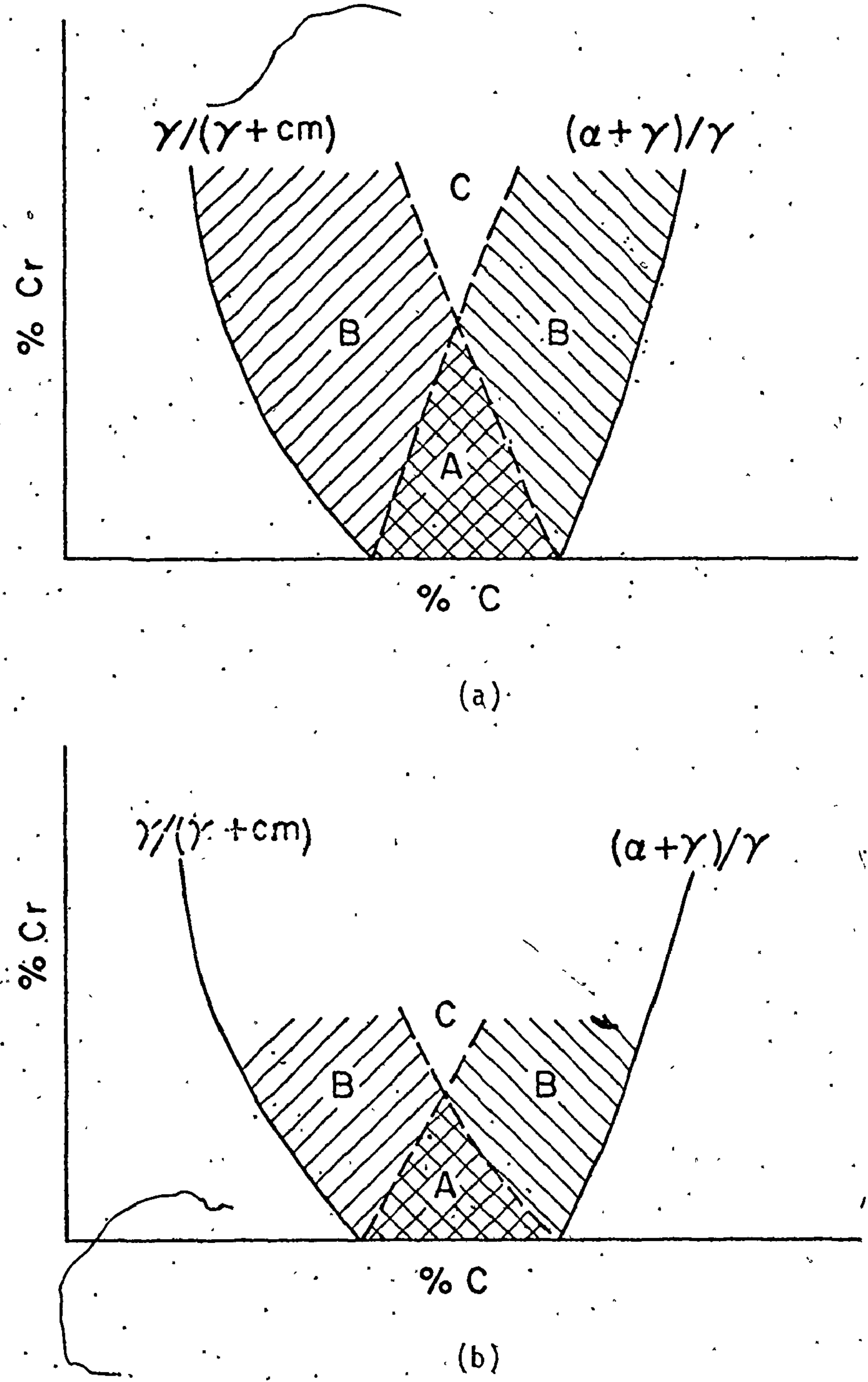

Figure 28. Schematic partition and no-partition zones in the Fe-C-Cr system in the region of interest for the pearlite transformation (a) para-equilibrium (b) local equilibrium no-partition.

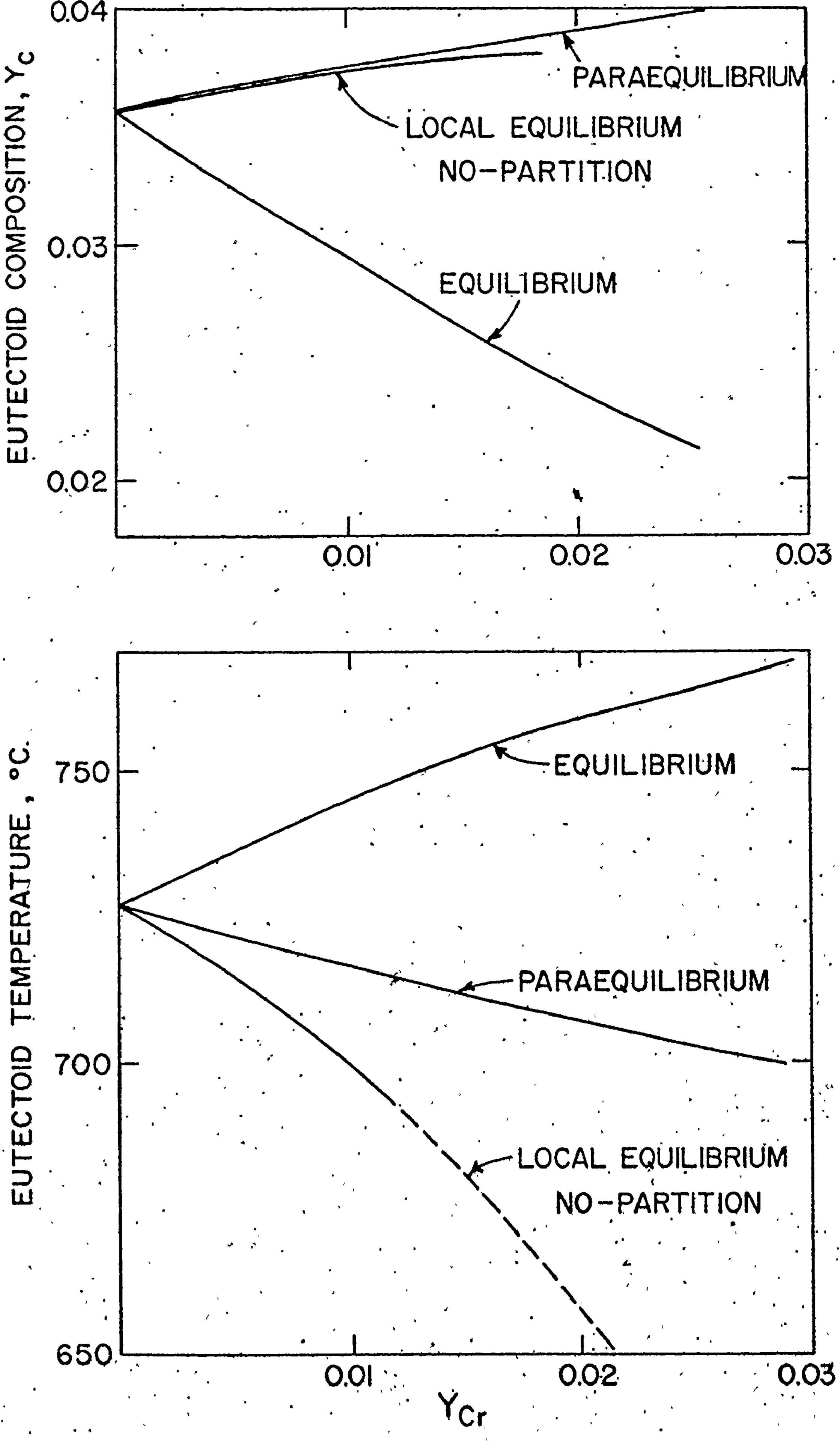
0.04
0.03
0.02
EUTECTOID COMPOSITION, Y_C
PARAEQUILIBRIUM
LOCAL EQUILIBRIUM
NO-PARTITION
EQUILIBRIUM
0.01
0.02
0.03
750
700
650
EUTECTOID TEMPERATURE, °C
EQUILIBRIUM
PARAEQUILIBRIUM
LOCAL EQUILIBRIUM
NO-PARTITION
0.01
0.02
0.03
Y_{Cr}

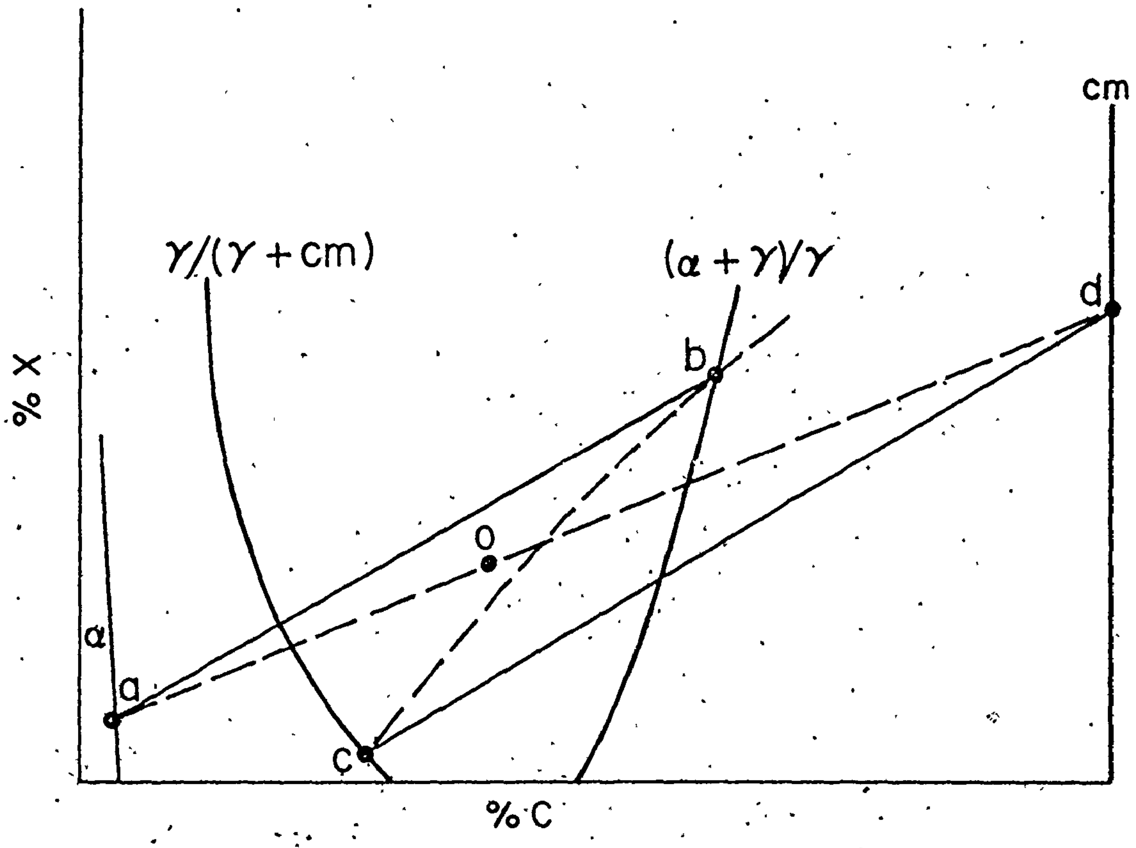

Figure 30. Schematic representation of chromium partitioning in the low supersaturation range.

(a) 20 sec (b) 40 sec

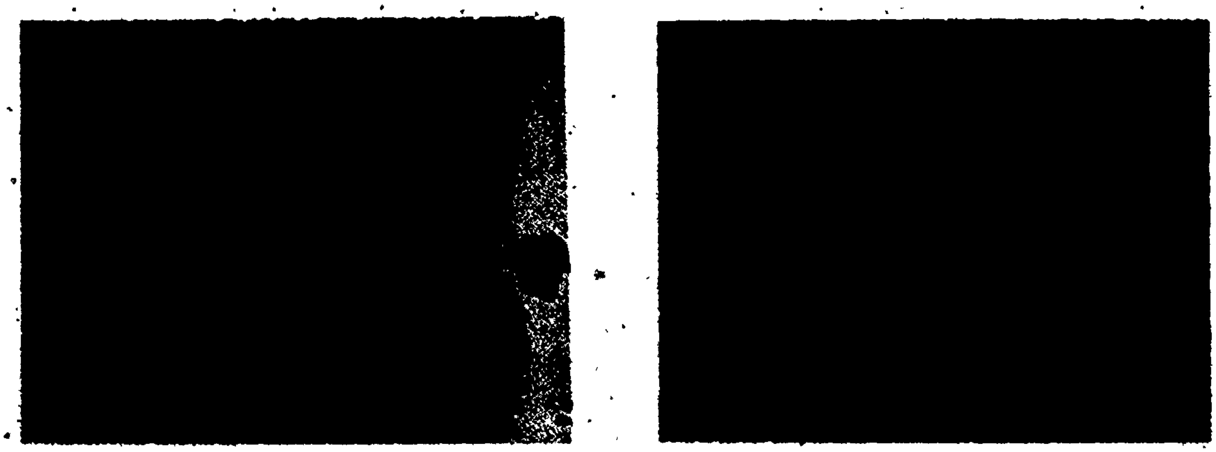

(c) 60 sec (d) 80 sec

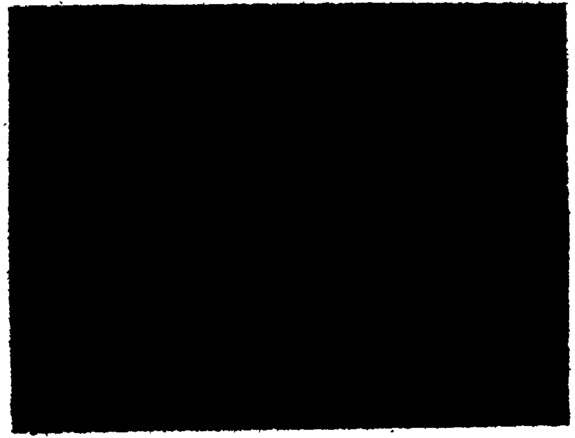

(e) 100 sec

Figure 31. Photomicrographs of pearlite growth during an isothermal experiment for the 1.8% Cr alloy at 690°C. (x70)

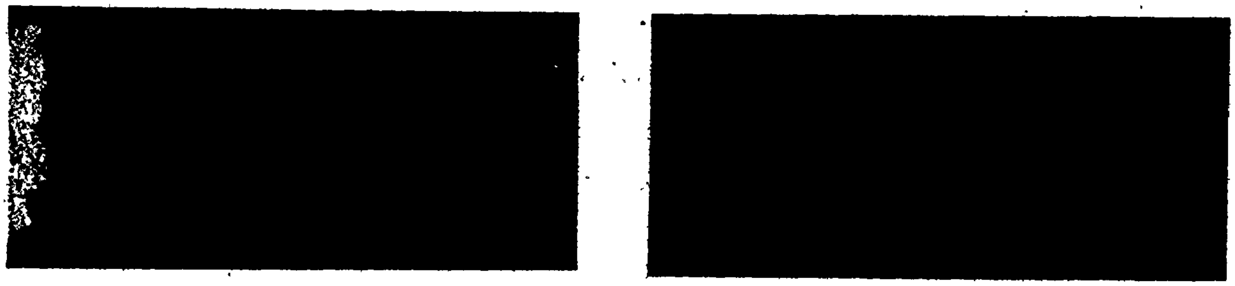

(a) 10 sec (b) 14 sec

(c) 18 sec (d) 22 sec

(e) 26 sec

Figure 32. Photomicrographs of surface pearlite growth during an isothermal experiment for 0.9% Cr alloy at 660°C. (x70)

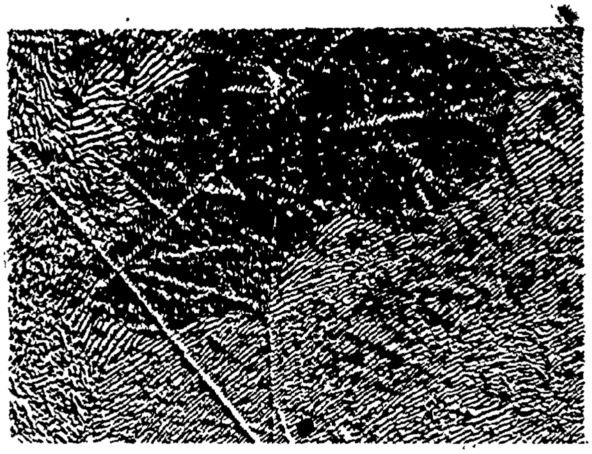

(a) 1.8% Cr alloy, 705°C

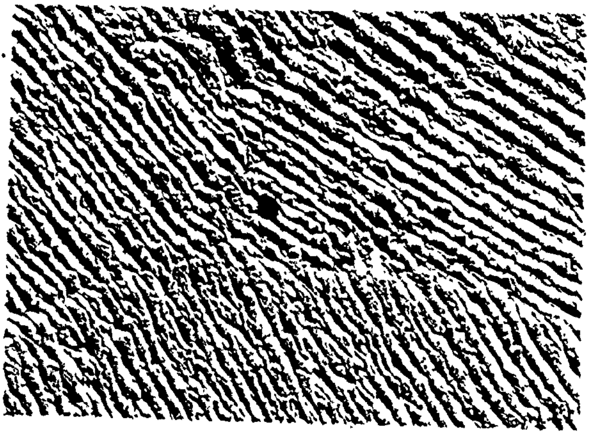

(b) 0.9% Cr alloy, 710°C

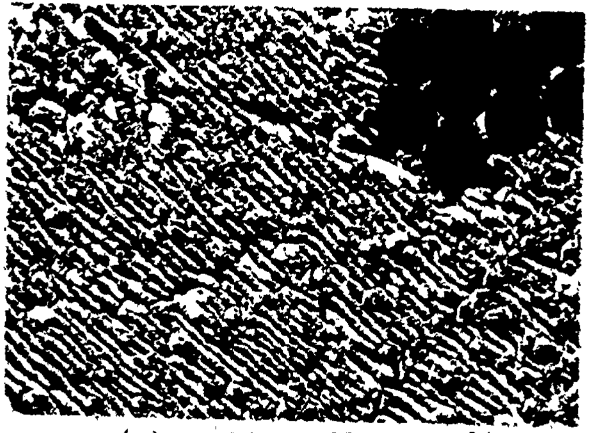

(c) 0.4% Cr alloy, 620°C

Figure 33. Typical pearlite surface replica photomicrographs for measuring the interlamellar spacing.

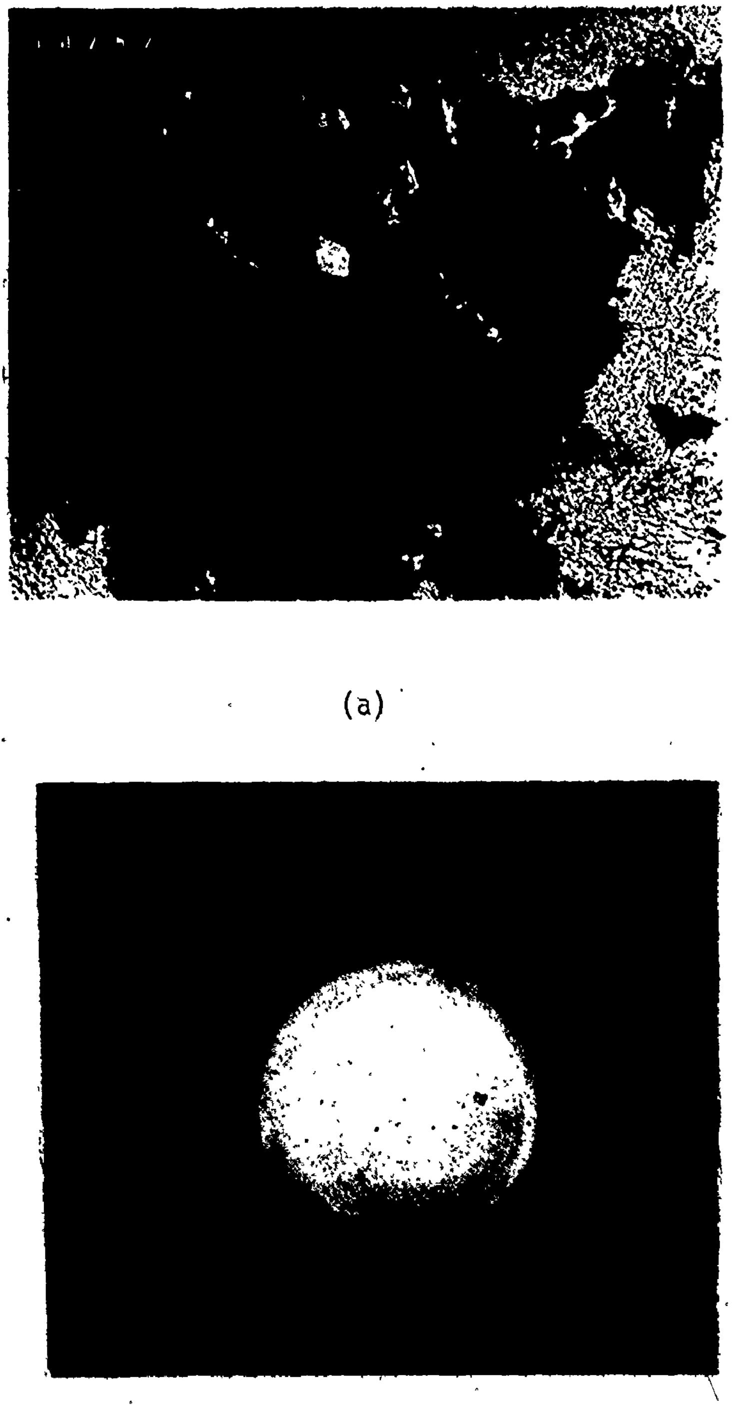

(a)

(b)

Figure 34. Typical (a) pearlite carbon extraction replica of the partially transformed Fe-C-Cr alloy (x2500) and (b) selected area electron diffraction pattern.

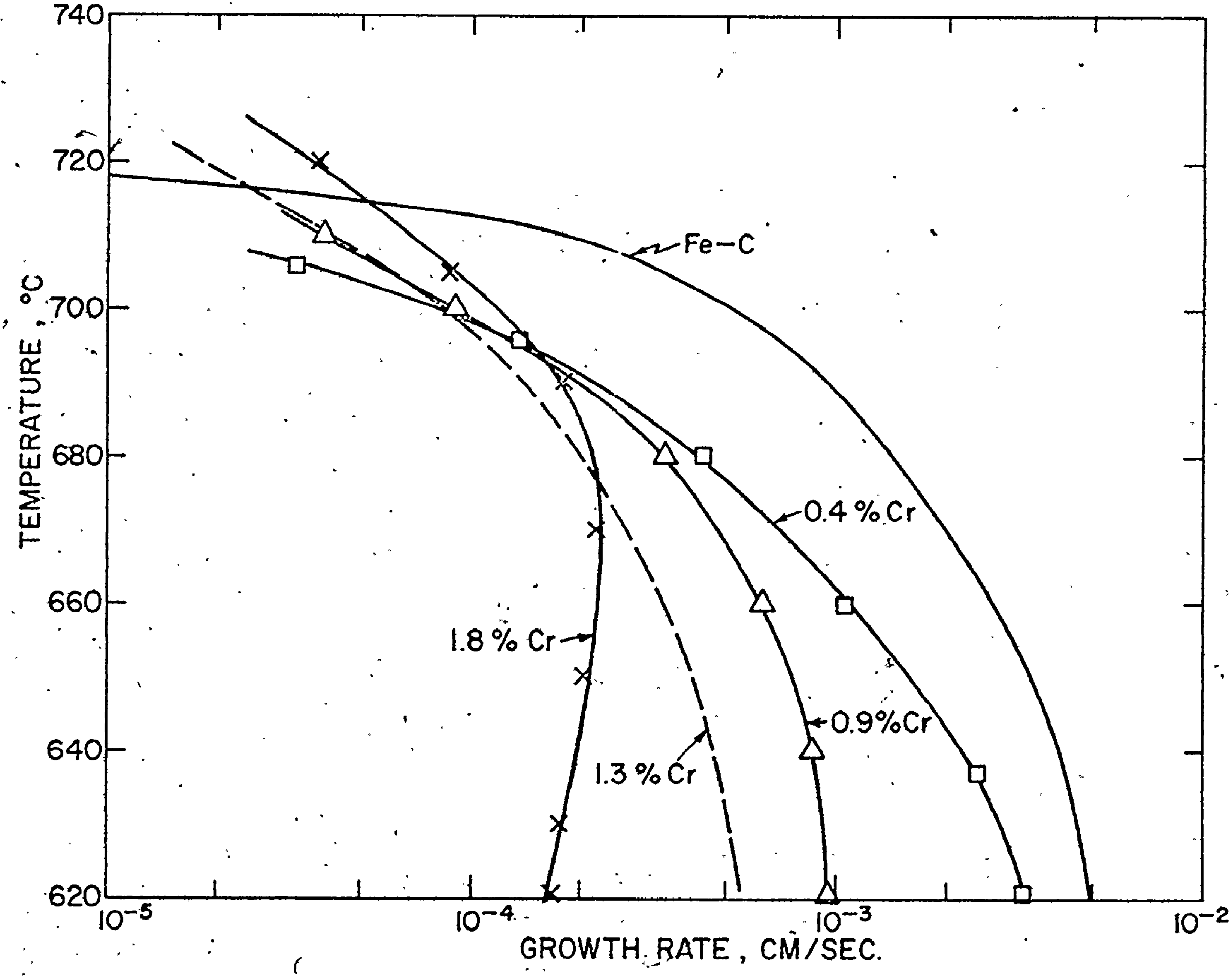

Figure 35. Pearlite growth rates as a function of transformation temperature.

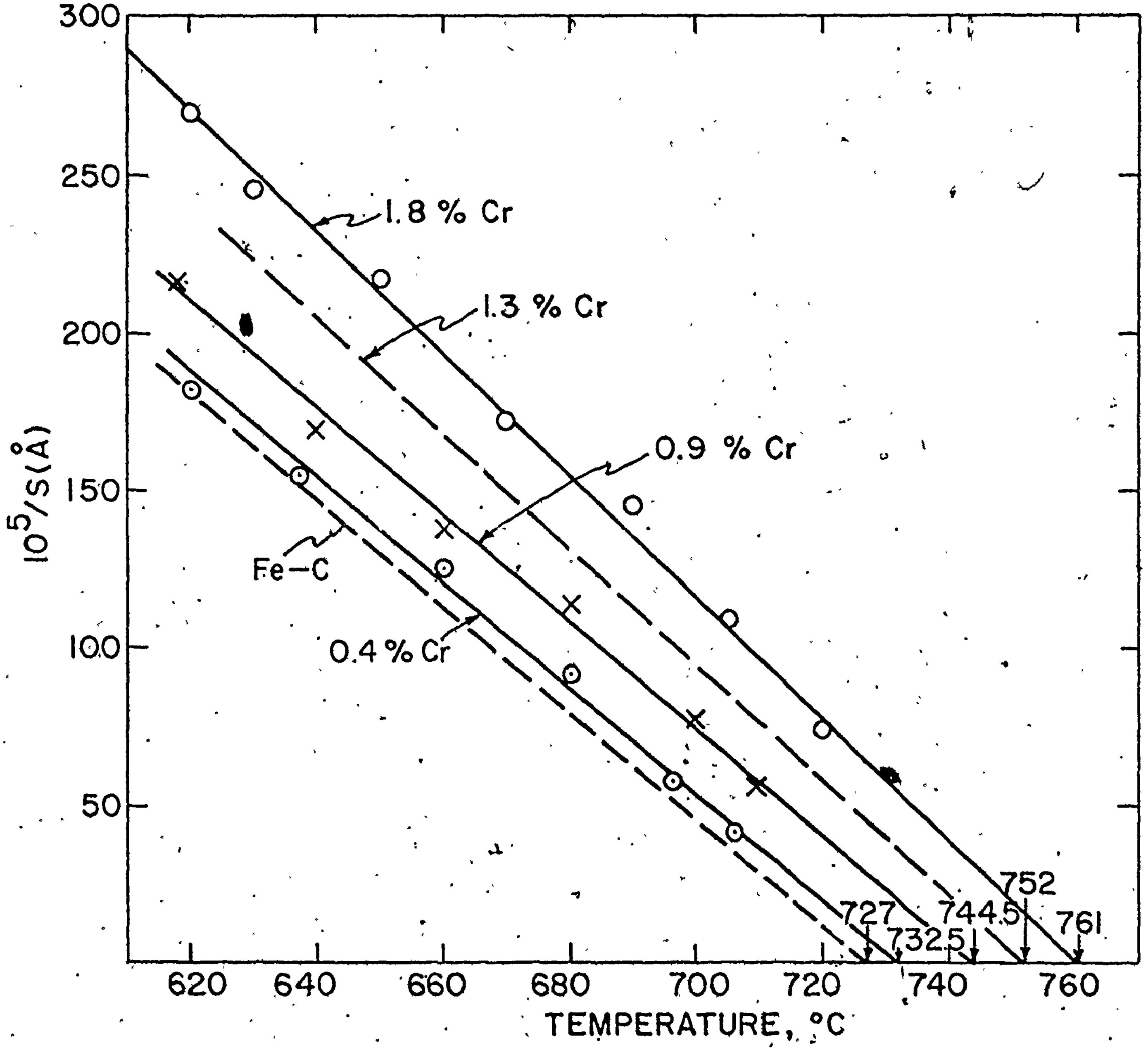

Figure 36. Reciprocal interlamellar spacing as a function of transformation temperature.

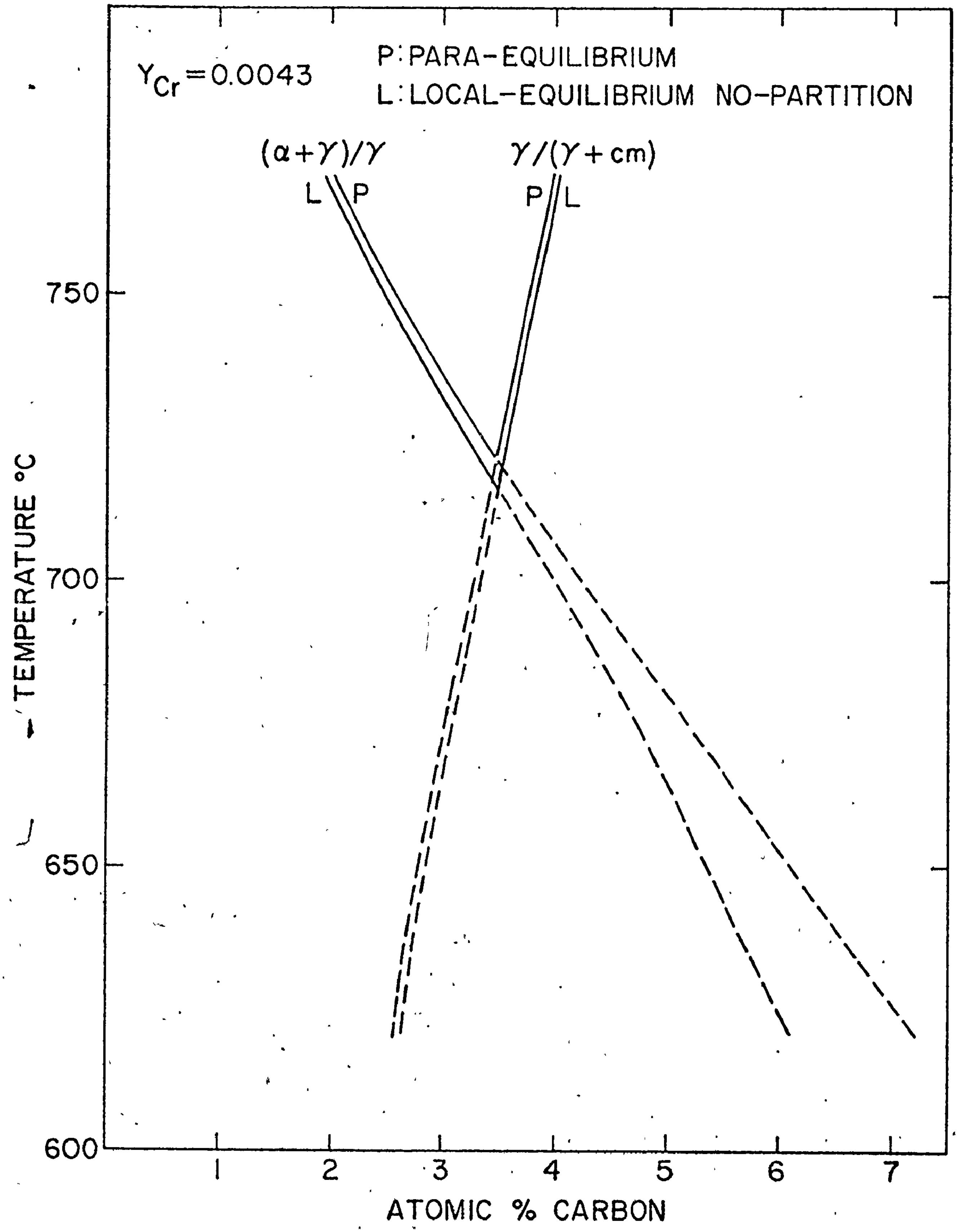

Figure 37. Calculated para-equilibrium and local equilibrium no-partition

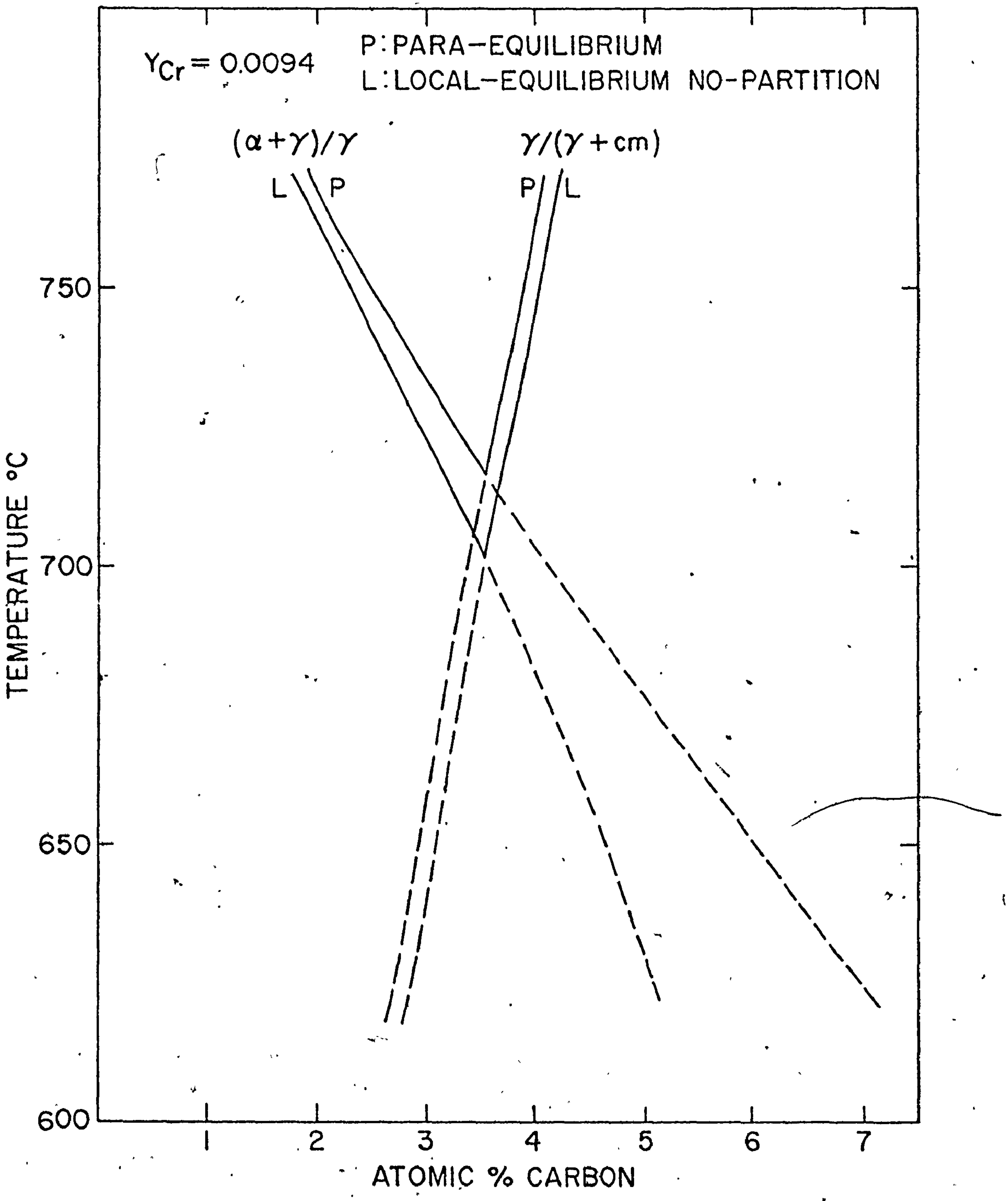

Figure 38. Calculated para-equilibrium and local equilibrium no-partition phase boundaries for 0.9% Cr alloy.

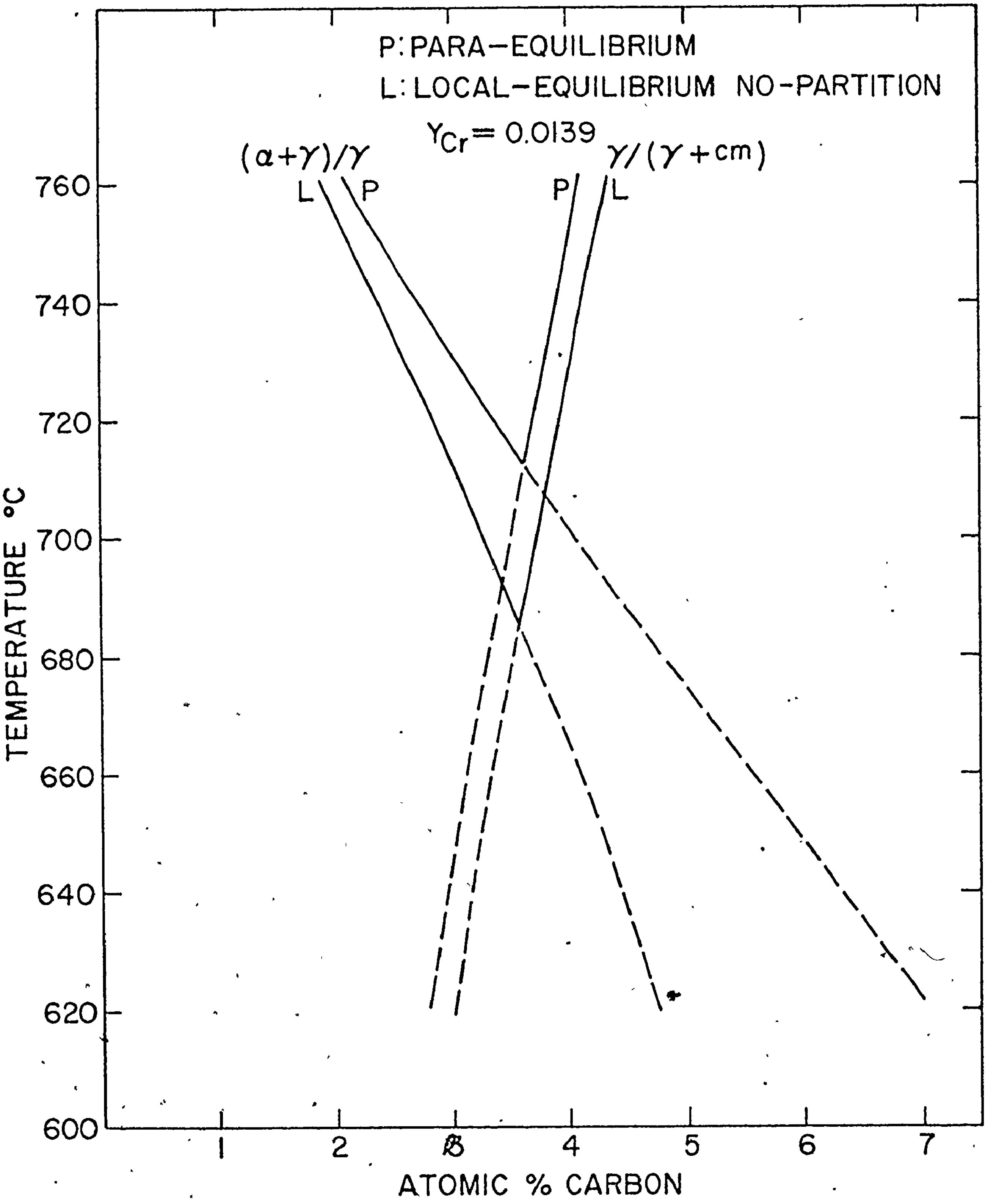

Figure 39. Calculated para-equilibrium and local equilibrium no-partition phase boundaries for 1.3% Cr alloy.

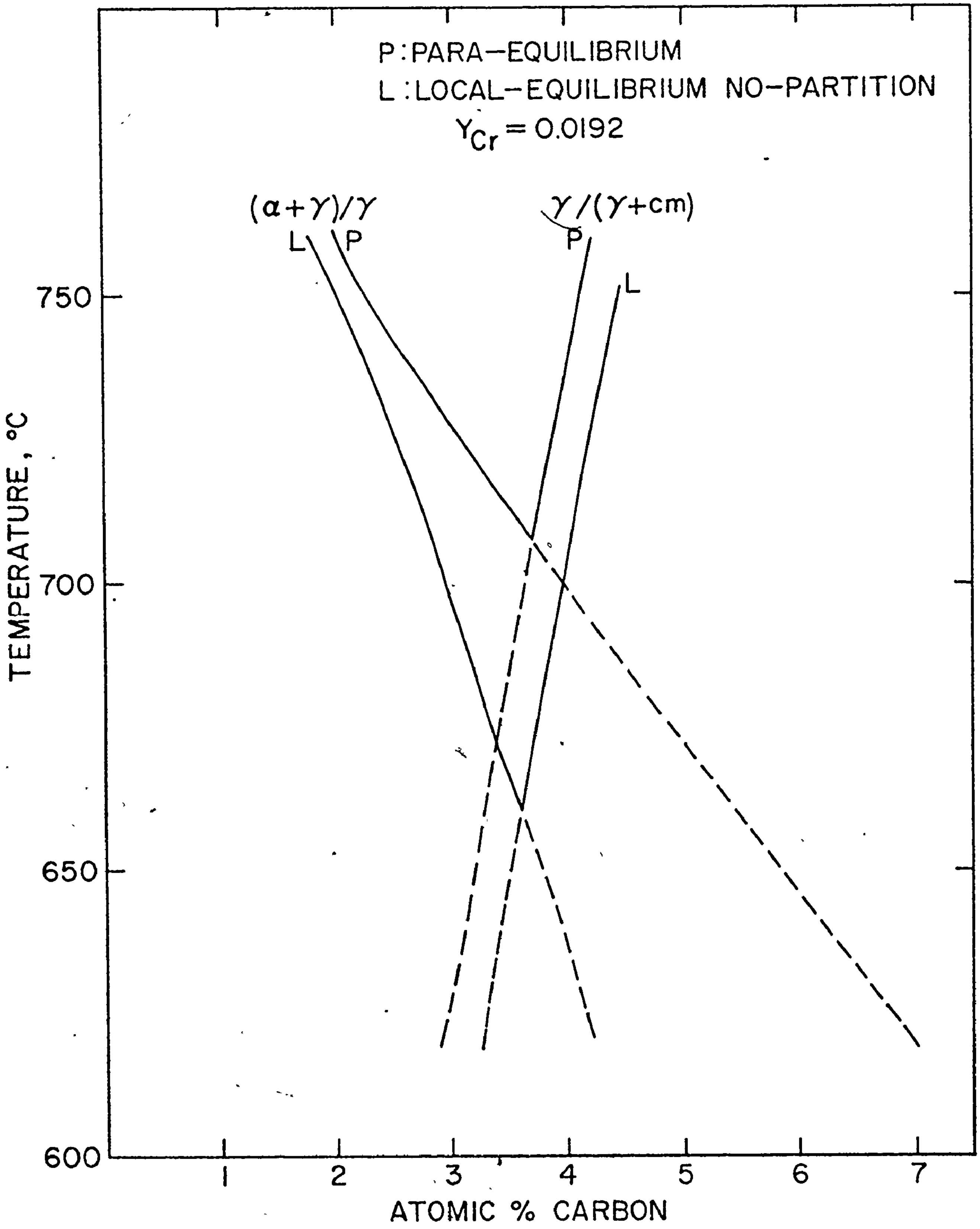

Figure 40. Calculated para-equilibrium and local equilibrium no-partition phase boundaries for 1.8% Cr alloy.

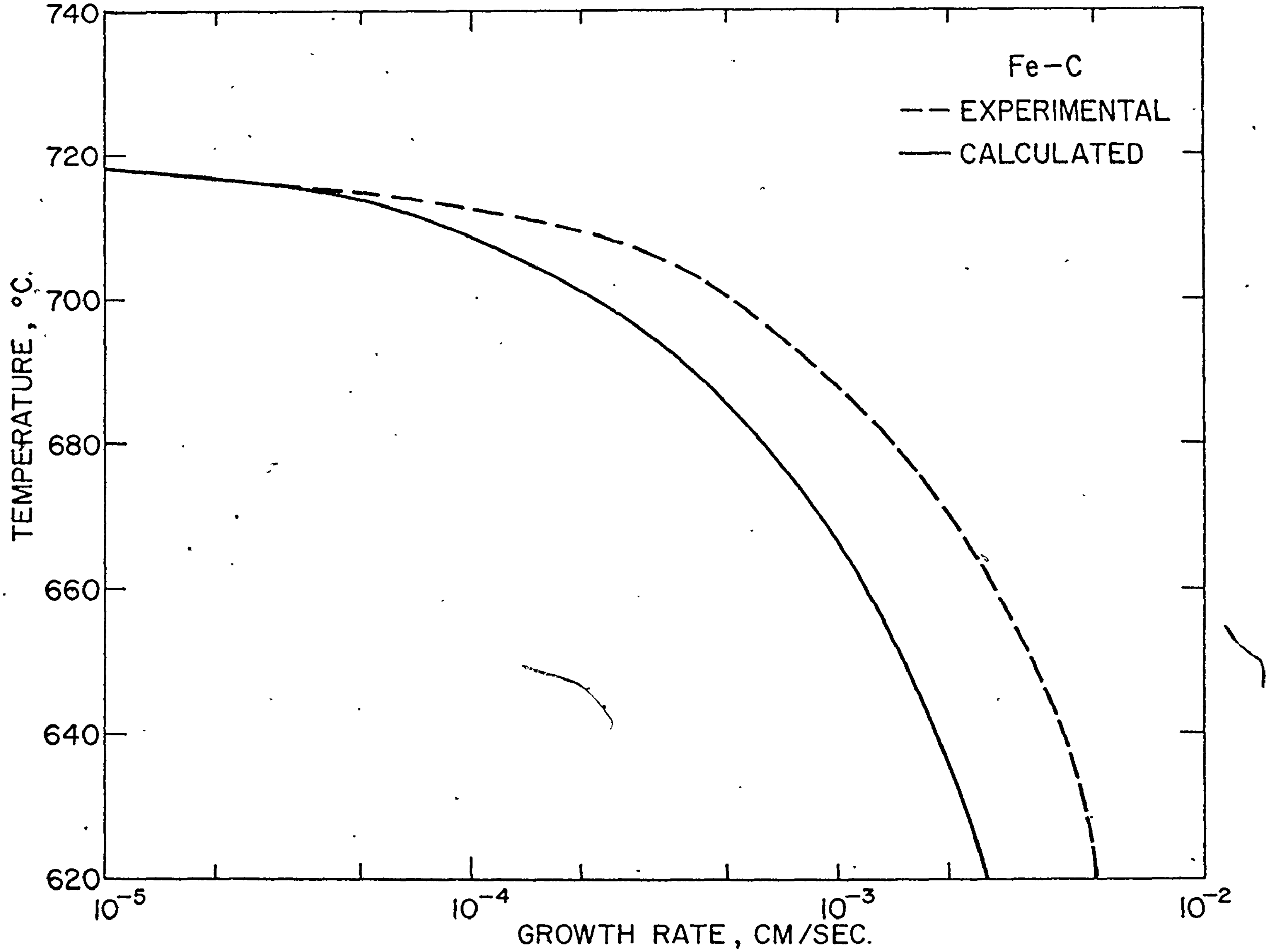

Figure 41. Calculated and experimental pearlite growth rates for Fe-C.

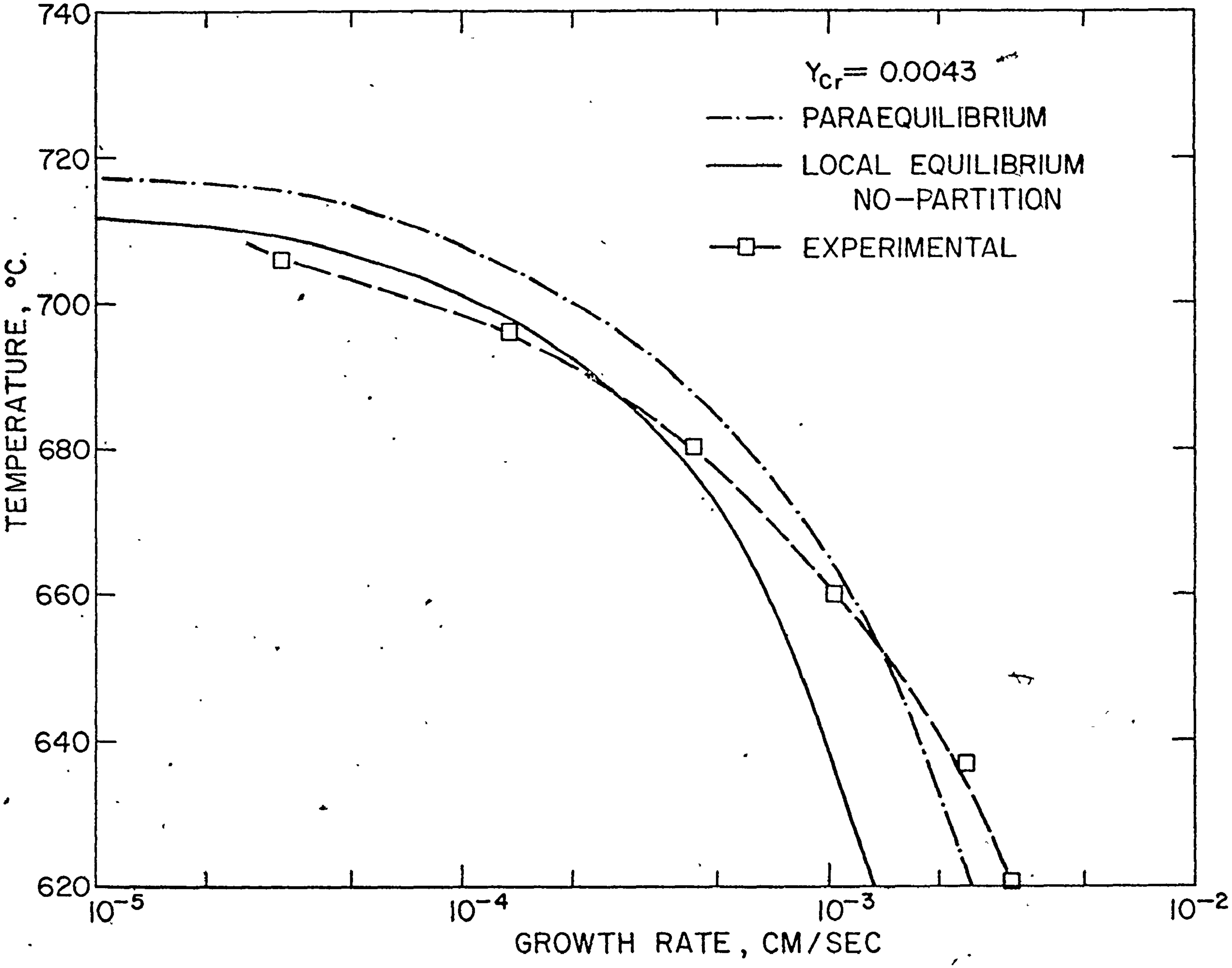

Figure 42. Calculated and experimental pearlite growth rates for 0.43 Cr Alloy.

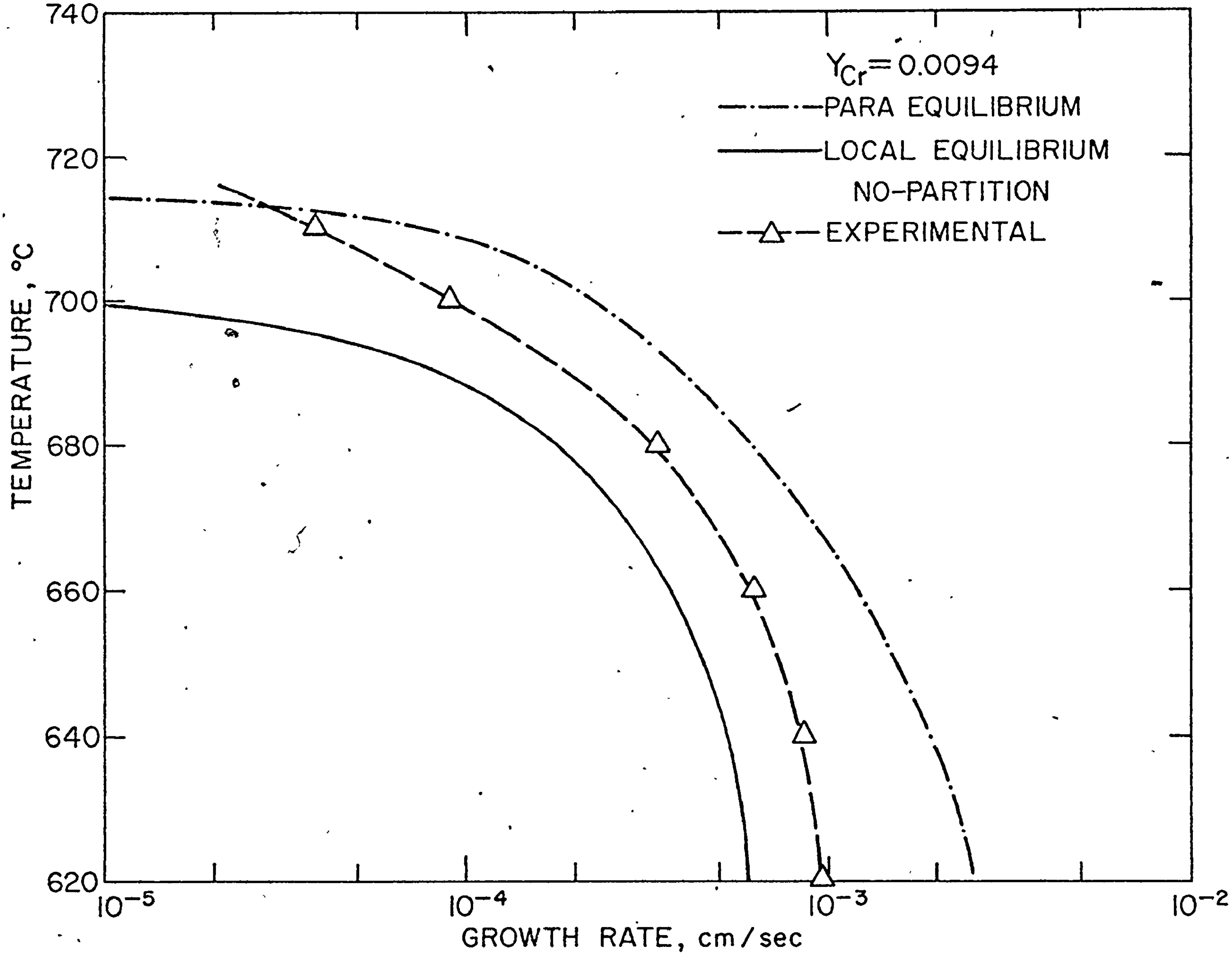

Figure 43. Calculated and experimental pearlite growth rates for 0.9% Cr alloy.

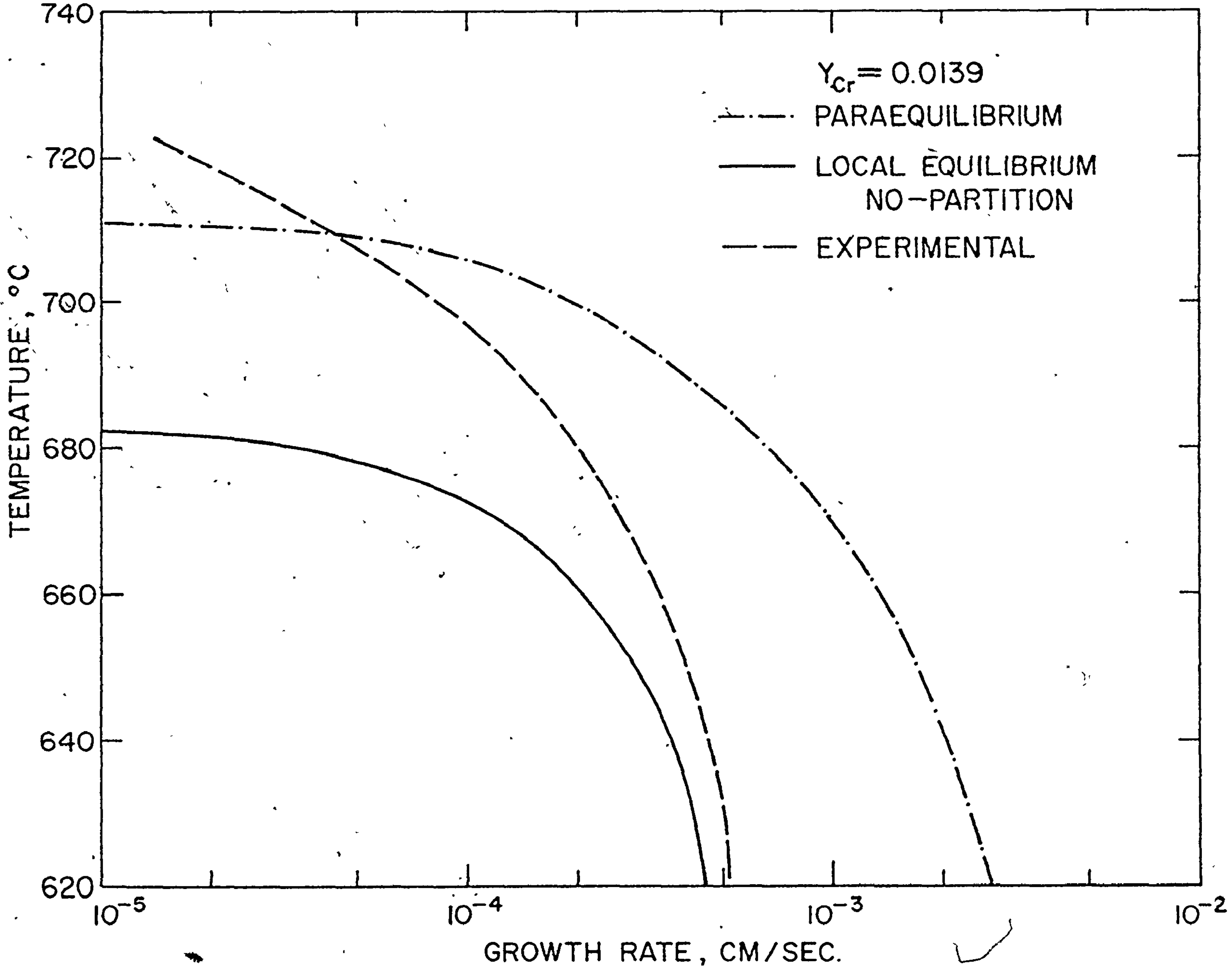

Figure 44. Calculated and experimental pearlite growth rates for 1.3% Cr alloy.

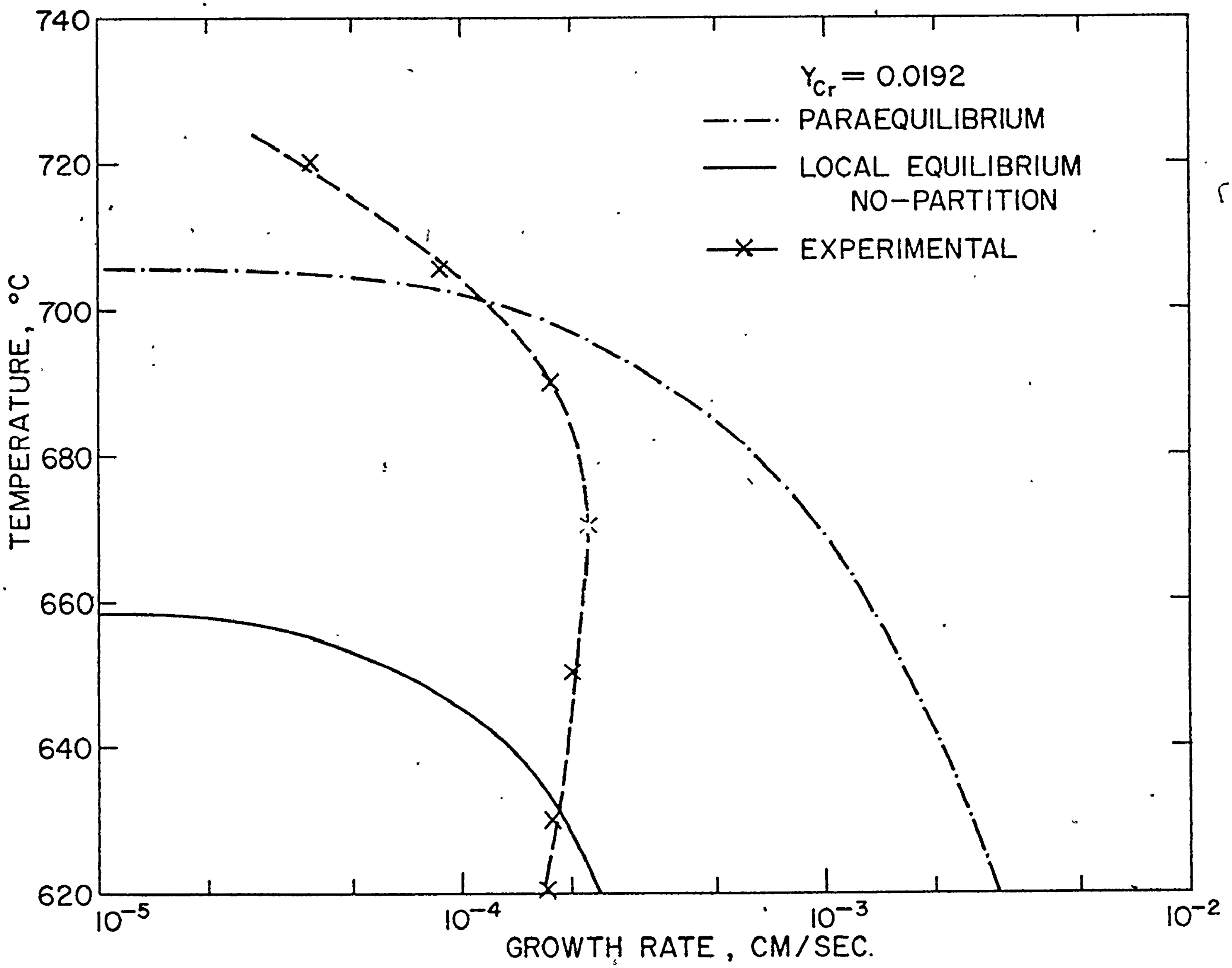

Figure 45. Calculated and experimental pearlite growth rates for 1.8% Cr alloy.

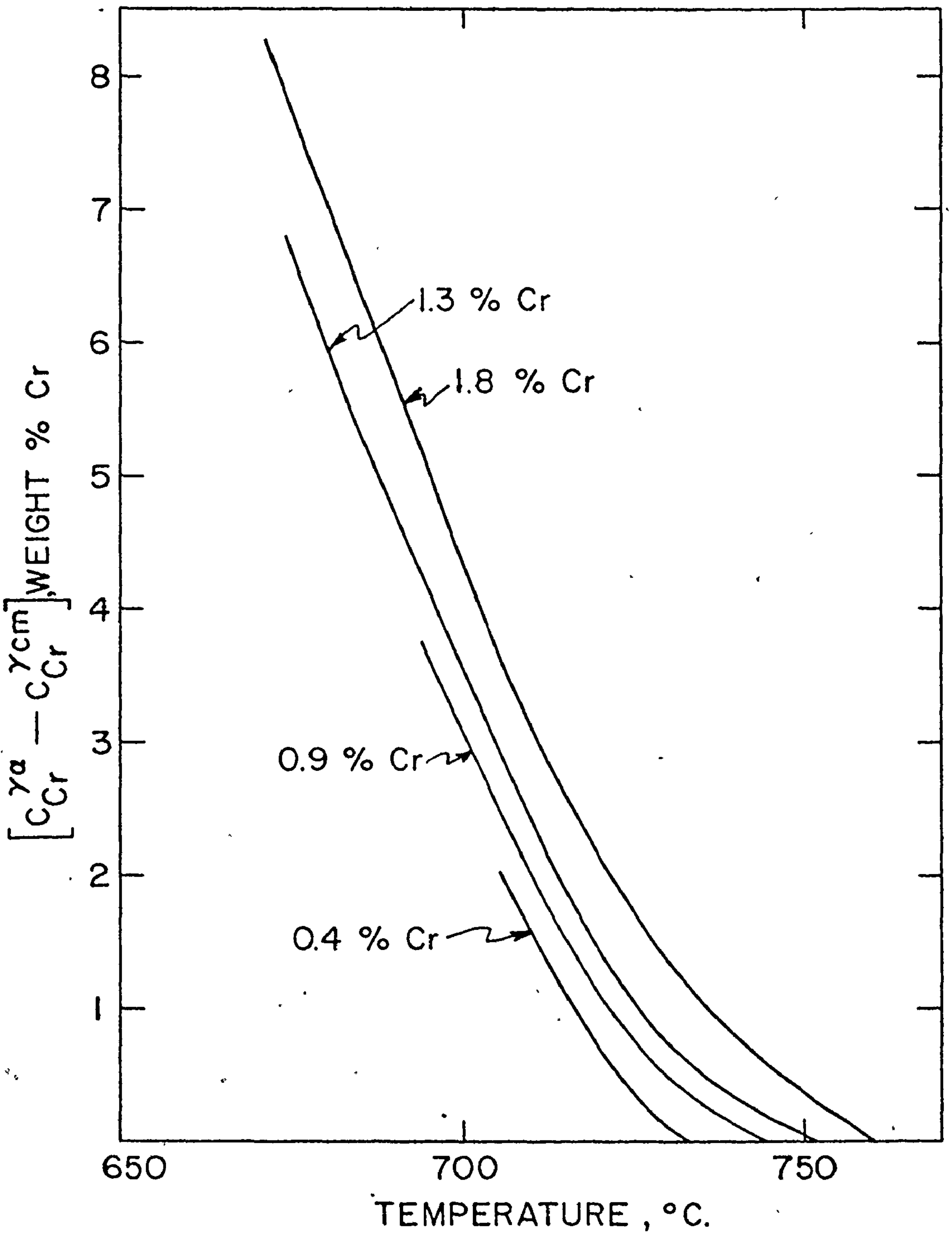

Figure 46. Driving force for chromium phase boundary diffusion at low supersaturations.

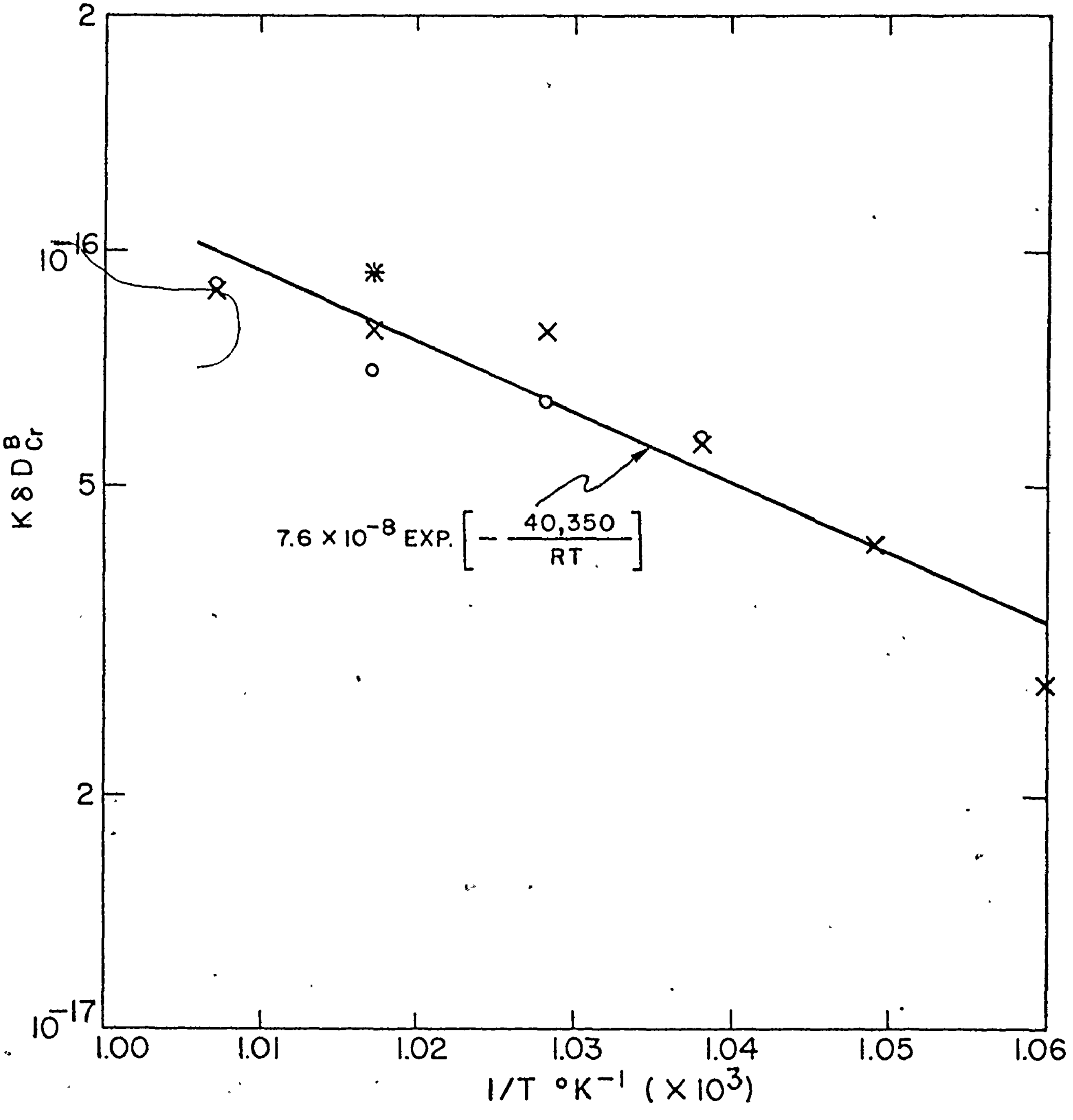

Figure 47. Effective chromium phase boundary diffusivity at low supersaturations as a function of temperature.

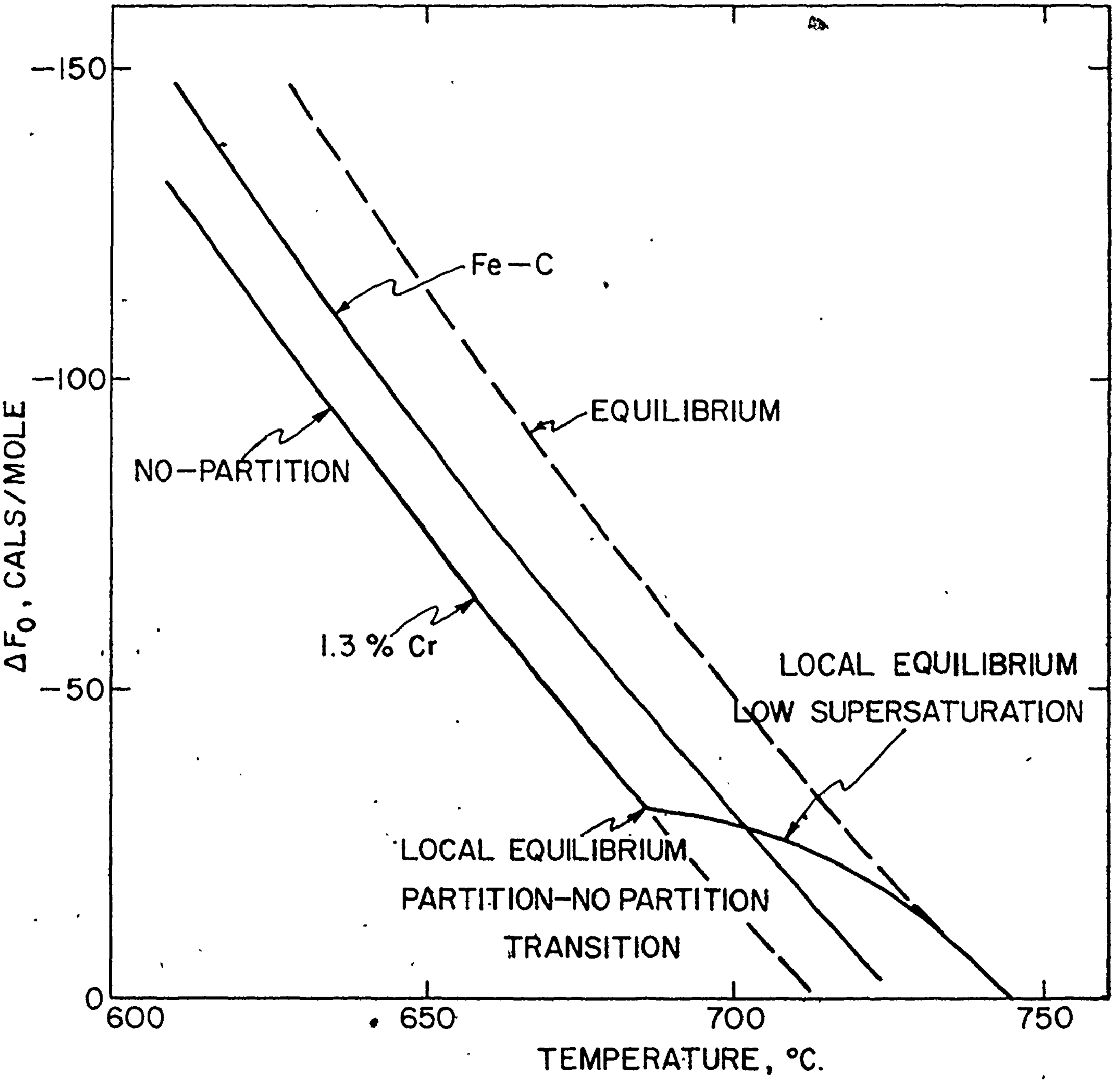

Figure 48. Free energy of transformation, ΔF_0, for the pearlite reaction as a function of temperature.

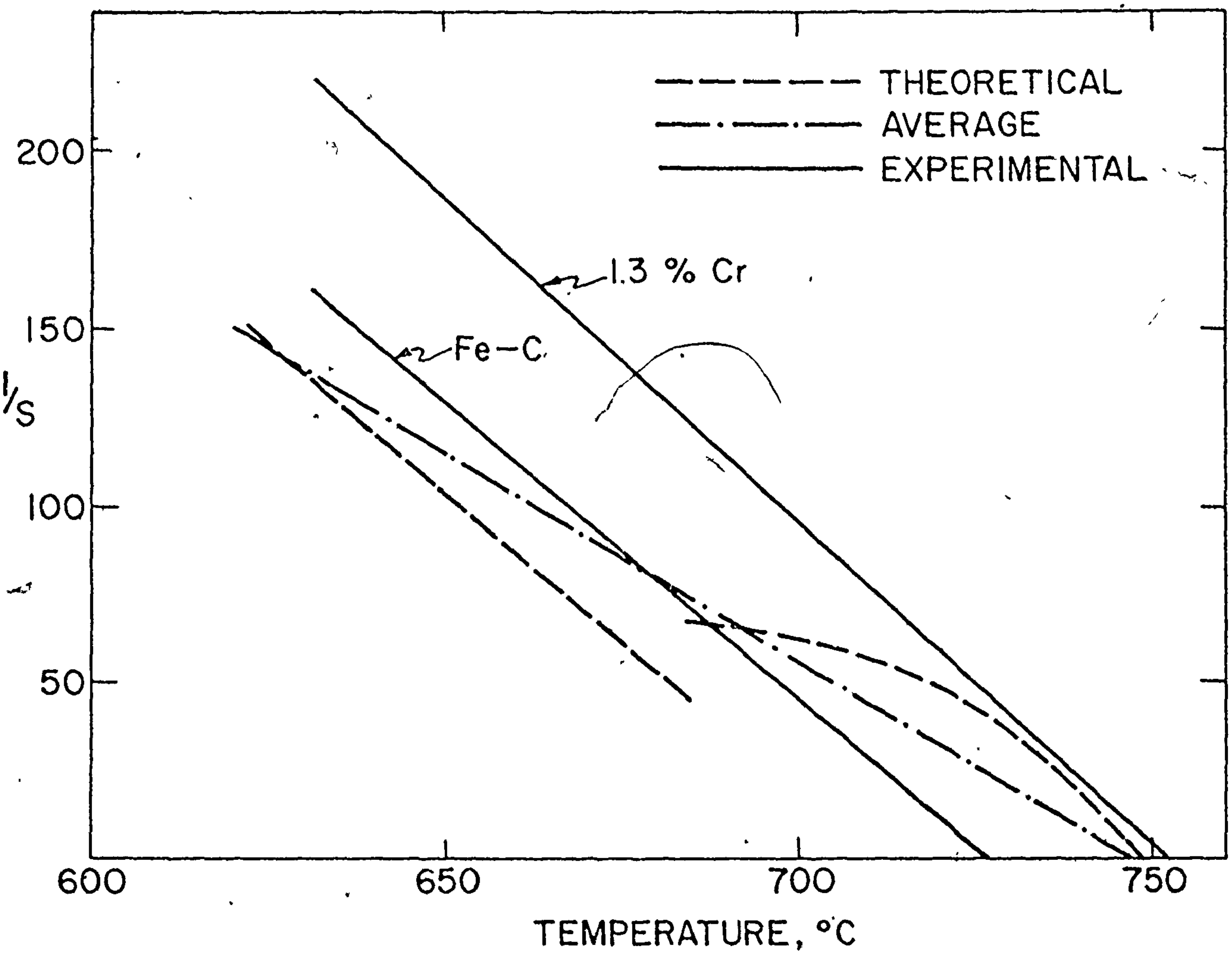

Figure 49. Expected 1/S vs T relationship for 1.3% chromium steel on the basis of ΔF_0.

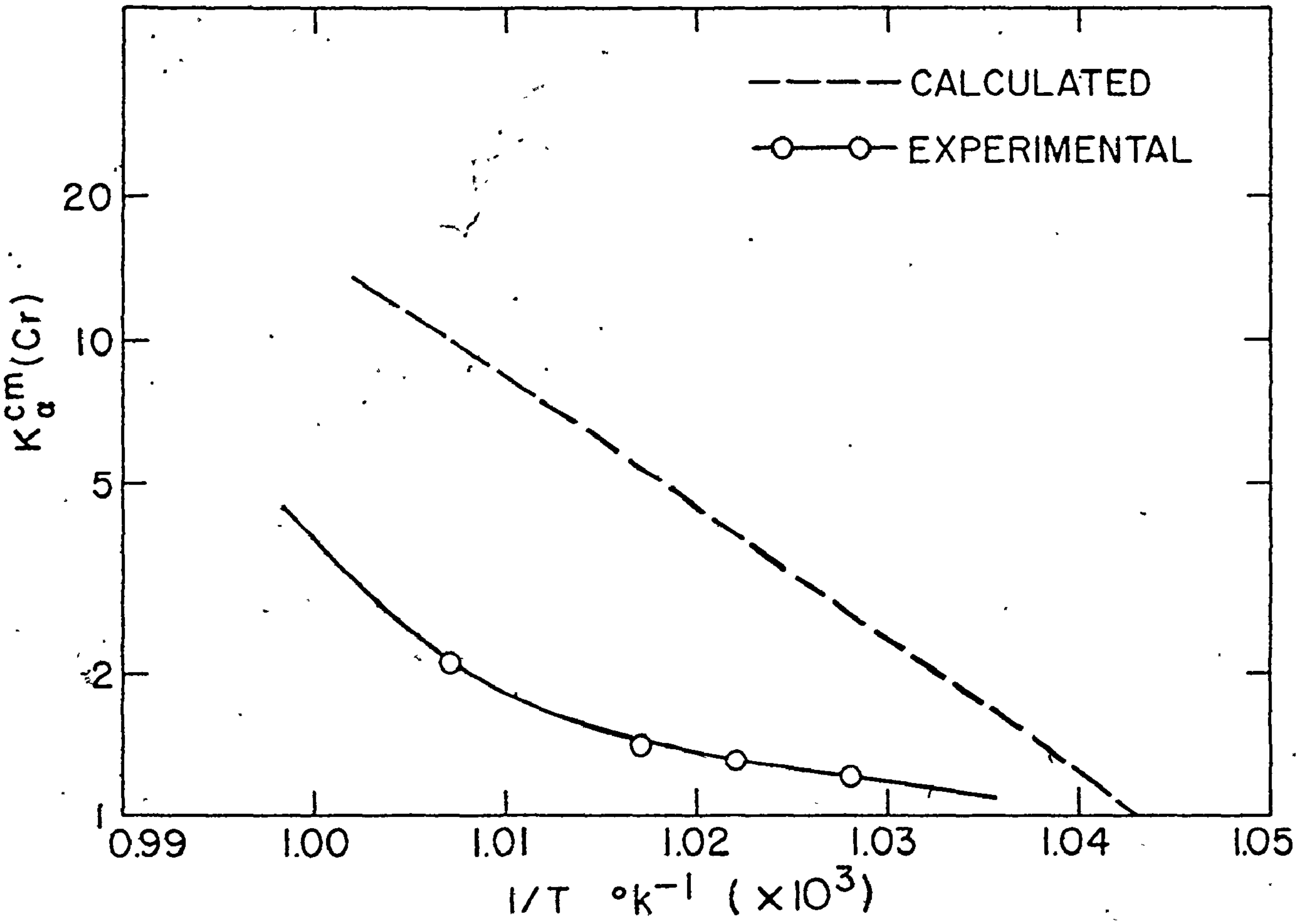

Figure 50. Calculated and experimental (after Razik et al.) chromium partition data for 1.3% chromium steel at low supersaturations.

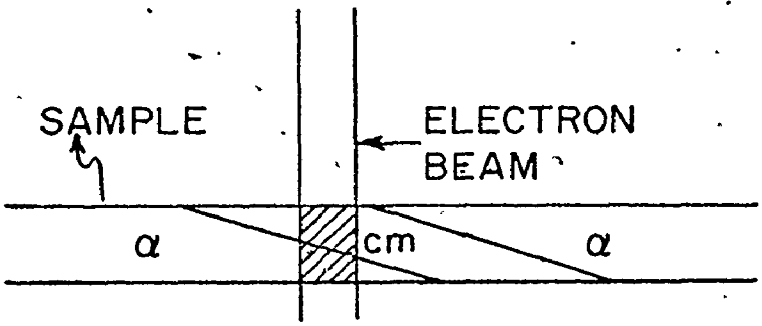

Figure 51. Schematic representation of a possible source of error in the chromium partitioning experiments of Razik et al.

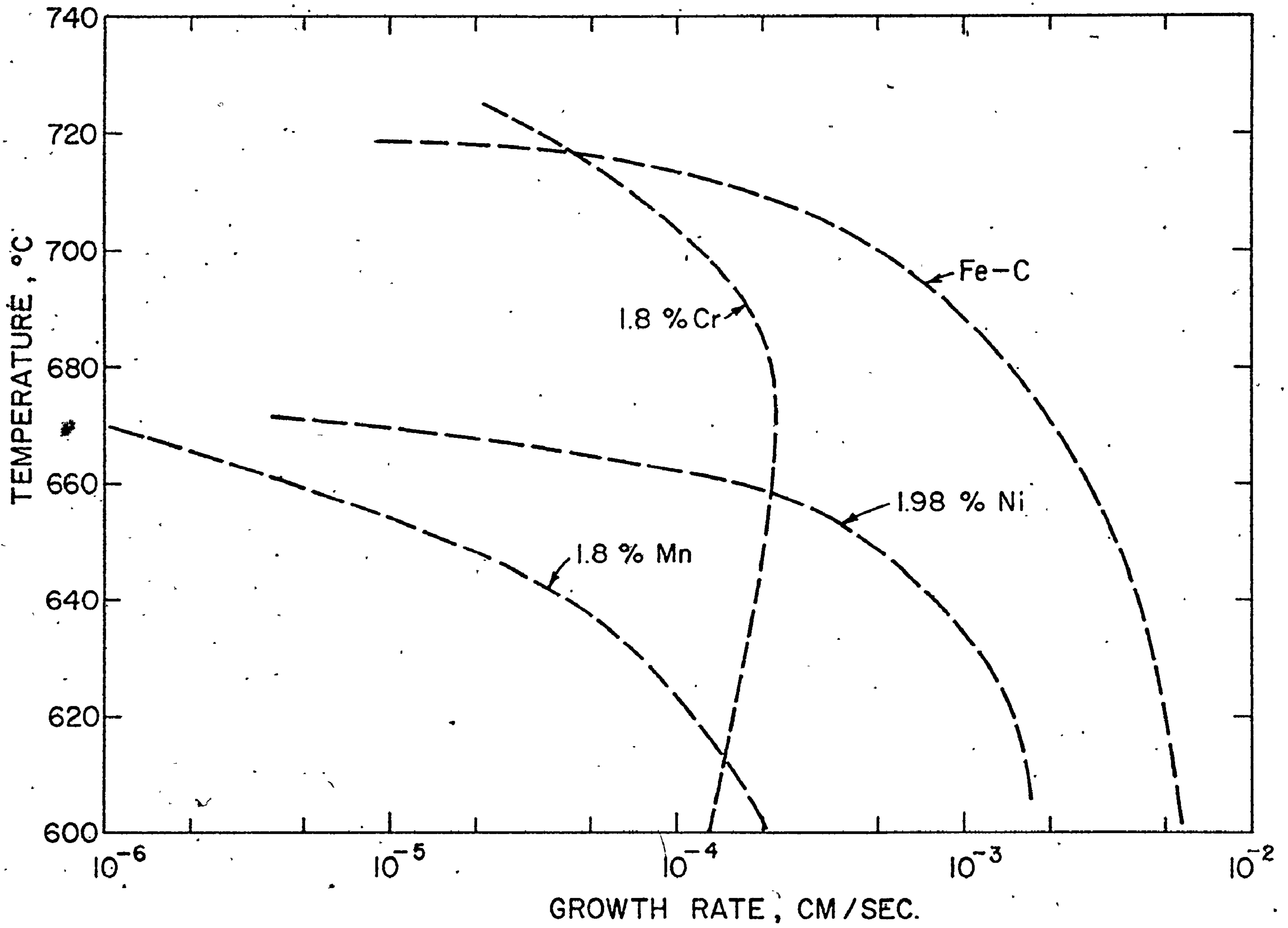

Figure 52. Experimental pearlite growth rates as a function of temperature for approximately 2% Cr, Mn and Ni steels.

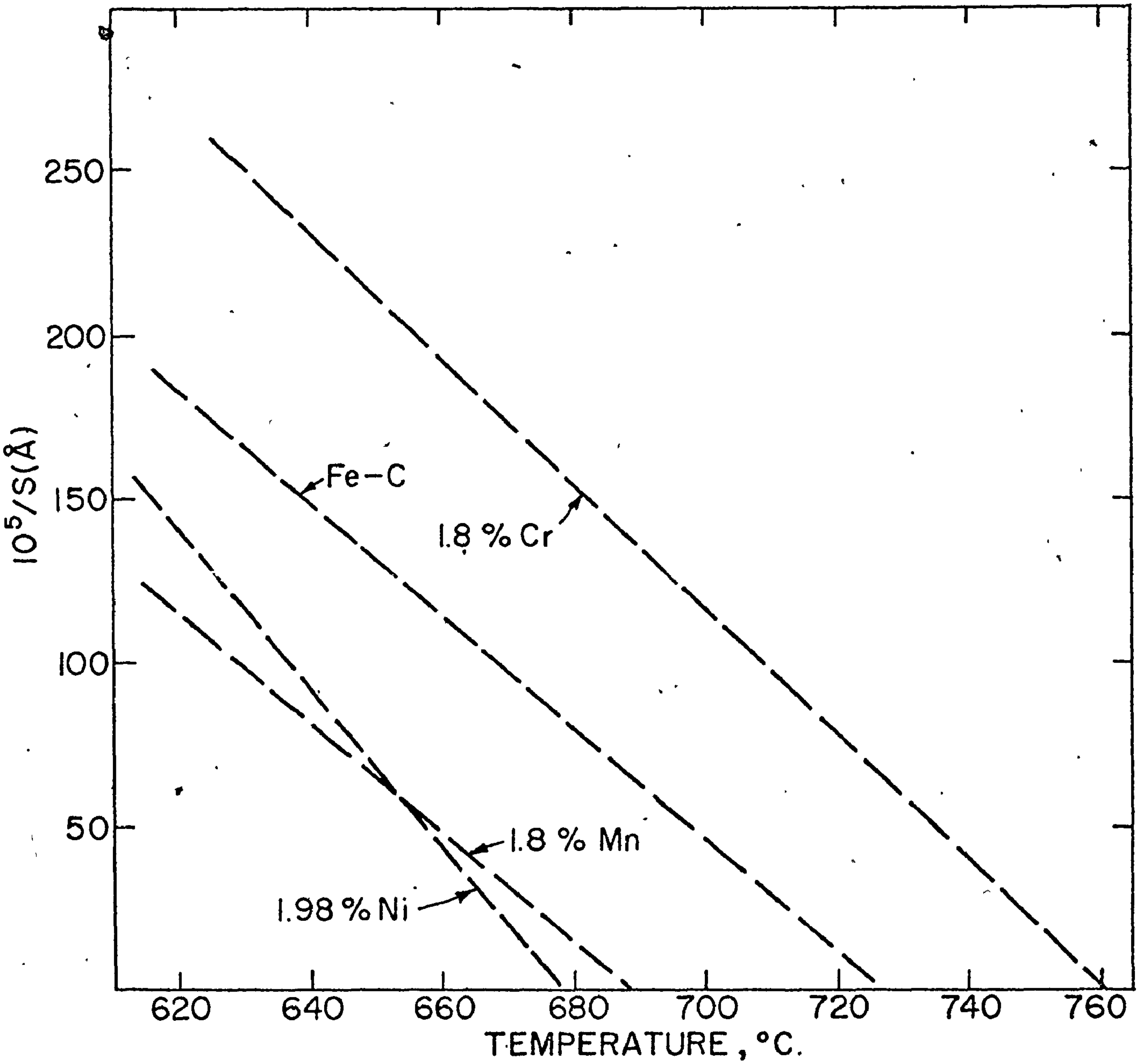

Figure 53. Reciprocal interlamellar spacing as a function of temperature for approximately 2% Cr, Mn and Ni steels.

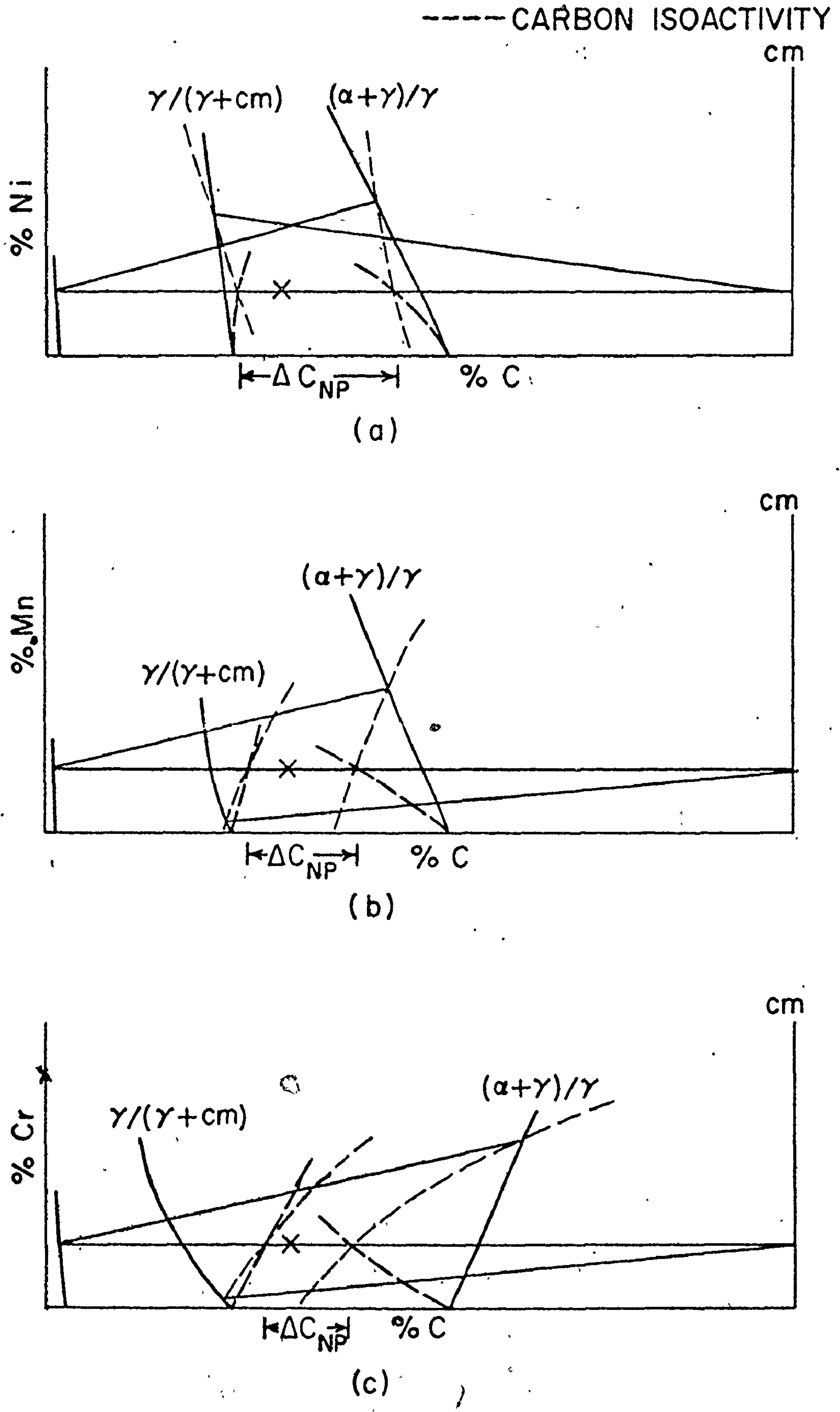

Figure 54. Schematic representation of the relative effect of ε_C^X on the driving force, ΔC_{NP}, for the pearlite reaction by the local